Artifact-suppressing reconstruction for X-ray near-field holography

Vom Promotionsausschuss der
Technischen Universität Hamburg

zur Erlangung des akademischen Grades

Doktor-Ingenieur (Dr.-Ing.)

genehmigte Dissertation (Monografie)

von
Johannes Dora

aus
Hamburg

2026

Vorsitzende des Prüfungsausschusses: Prof. Dr. Sabine Le Borne
(Technische Universität Hamburg)

Gutachter: Prof. Dr.-Ing. Tobias Knopp
(Technische Universität Hamburg)
Prof. Dr. Christian Schroer
(Universität Hamburg)

Tag der mündlichen Prüfung: 03.06.2025

ORCID: 0009-0001-4283-8499

Acknowledgments

The decision to leave my job in industry and start a doctoral thesis is something I definitively do not regret. The infamous episodes of stress and self-doubts, which accompany the writing of a doctoral thesis, were always compensated by having a lot of fun at work. The fun was the result of having a good time with colleagues, conducting incredibly interesting experiments and appreciating the knowledge gain to satisfy my curiosity. Interdisciplinary research like this is only possible with contributions and commitment from many people. Throughout my academic journey, colleagues, friends, and family strongly supported me in reaching this milestone of finishing my thesis. I would like to acknowledge and thank the people who took part in this work.

First, I would like to express my gratitude to my principal investigators Tobias Knopp and Christian Schroer,as well as my supervisor Johannes Hagemann. Their openness and positive attitude where a source of motivation to delve deeper into physics and to pursue various ideas. Johannes happily discussed a wide variety of ideas and approaches on an eye-to-eye level, which I very much appreciated. He was always available to provide quick feedback and to proofread any written work.

I would also like to thank the amazing beamline staff, Silja Flenner and Imke Greving, for their support during the experiments and the development of my online reconstruction framework. I am also grateful that they allowed me to work within their beamline software. Silja tried out all of my ideas, no matter how crazy, on diverse experimental data. Their feedback on how different versions of the reconstruction algorithm performed on problematic datasets was invaluable.

Martin Möddel provided valuable advise for writing the two publications resulting from this thesis. I was especially glad about how the structure of the articles evolved over time, which would not have been possible without his input.

The software in this work was implemented on the high-performance computing cluster, Maxwell. I would especially like to thank Frank Schluenzen and his team for their quick and competent IT support.

Several colleagues helped proofread my thesis, which were Sina Röper, Thea Engler and Tang Li.

The doctoral thesis was funded by the Data Science in Hamburg Helmholtz Graduate School for Structure of Matter (DASHH). Here, I would like to thank Christiane Ehrt and Heike Hufnagel Martinez for the organization and Sabine Le Borne for taking on the panel chair of the project.

I would also like to thank Berit Zeller-Plumhoff for spontaneously offering me a job to help me bridge the financial gap between contracts.

Finally, I would like to thank my family. My parents, Anastasia Kilogou-Dora and Helmut Dora, made it possible for me to study at a university. I would also like to thank my wife, Sunniva Lange, who encouraged me to switch from industry to science and pursue a doctoral degree. This meant moving to a different city. She always lifted me up when self-doubt and looming deadlines hit.

Abstract

X-ray near-field holography is an excellent tool for imaging objects with a resolution in the nanometer range. Full-field measurements with a lens-free microscopic measurement setup allow holograms of objects to be recorded at multiple magnifications. Unfortunately, these holograms can only be measured as an integral over a certain period of time. The phase information of the hologram is lost and only the intensities are recorded, commonly known as the phase problem. To recover the phase information, a spatial support and/or the recording of several holograms at different detector distances are usually used as additional information in reconstruction approaches. However, both constraints are only feasible for a very closed set of experiments, require time consuming optimization of hyper-parameters and a lot of computation time. Avoiding both techniques is a necessity to enable *in-situ*/*operando* measurements but, in doing so, reconstruction artifacts appear. Another challenge is the Autofocus problem. For the reconstruction of holographic data, the numerical focus of the measurement setup is part of the forward model and must be known very precisely. If the numerical focus is inaccurately embedded in the forward model of the reconstruction algorithm, it will generate artifacts or result in blurred reconstructed images. In practice, it is often difficult to accurately determine the Fresnel number for a good reconstruction. In the following work, the origin of possible artifacts as described above is investigated in detail and countermeasures are developed by adjusting the raw data preprocessing, by adjusting the reconstruction and by an automatic optimization of the forward model.

The first part of this thesis addresses reconstruction artifacts with respect to a reference method, a projected gradient decent approach, using a Nesterov accelerated gradient. The reconstruction artifacts have the following identified causes: Truncation artifacts are caused by the limited field of view of the detector. The real hologram is cut off and as a result, the acquired image contains inconsistent areas at the borders. Mirroring the hologram in all directions in combination with a modified window function is derived as a countermeasure to reduce the impact of truncation edges. Low frequency artifacts are identified to be mainly caused by a global normalization error in the empty beam normalization or flat-field-correction. The normalization is corrected by introducing a constant offset parameter into the reconstruction. Other artifacts are overestimation artifacts, mainly caused by the Nesterov acceleration. The forward model amplifies this effect, which is sensitive to high spatial frequencies. To reduce the overestimation of the phase and absorption values, a regularization of the absorption values is applied, which is sufficient for both parameters simultaneously. The insensitivity of the forward model to low spatial frequencies leads to weak reconstruction artifacts. These are therefore reconstructed slowly since they have a small impact on the reconstruction loss. A newly introduced frequency-dependent Nesterov momentum and iterations on multiple grids explicitly accelerate the reconstruction of low frequencies. Both techniques also reduce an overestimation of high spatial frequencies. The combination of all described methods is summarized in a new artifact-suppressing reconstruction method (ASRM). Compared to the reference algorithm, it suppresses all artifacts mentioned above and reduces the reconstruction time significantly.

The second part of the thesis proposes a solution to the autofocus problem with an approach to automatically optimize the Fresnel number. The approach consists of three problems to be solved. An error metric is required that quantifies the distance between the estimated forward model and the correct one. A global optimization has to be defined, which has to be solved by an appropriate solver. As an error metric, a model fit error (MFE) metric is derived from data inconsistencies that are introduced when a non-negative electron density constraint is applied to a defocused wave-field. The novel error metric is evaluated by simulation and experimental results and finally compared with other error metrics from the literature. On simulated data, the MFE metric performs similarly to comparative error metrics and significantly better on experimental data. For an automated solution of the autofocus problem, a global optimization problem with respect to the numerical focus is formulated. The expected uncertainty of the setup geometry is added as a constraint to the target function. Since the gradients of the target function are not trivially accessible, a gradient-less downhill simplex method is chosen as a solver. As fine tuning, the parameters for the ASRM algorithm are adjusted so that the MFE behaves optimally.

Contents

Acronyms

AF autofocus 91, 92, 94, 99, 100, 106, 111, 113, 114

ASRM artifact suppressing reconstruction method 3, 70, 72, 80, 88, 89, 113, 114, 116–118

FFC flat-field correction 26, 27, 49, 51–54, 88

FOV field of view 35, 38–41, 46, 89, 114

FZP fresnel zone plate 15–19, 32, 34, 77

GI Gini index 102

GoG Gini index of the gradient 102, 106, 109, 113

GRA gradient 101, 106, 108, 113

HF high frequency 39, 69–71, 76, 88, 99, 102

LAP laplacian 101, 106, 108

LF low frequency 52–54, 56, 67, 72, 76, 77, 79, 81–83, 88

MFE model fit error 4, 97, 99, 103, 104, 106, 107, 111, 113, 114, 116, 117

MSE mean squared error 80, 88, 89, 95

NAG Nesterov accelerated gradient 31, 56, 57, 69, 70, 73, 74, 76, 88, 89

NFH near-field holography 2–4, 15, 17, 25, 27, 30, 32, 37, 56, 73, 77, 91, 92, 100, 113, 114

NM Nelder-Mead 99, 103, 105, 113

OE overestimation 57–59, 72, 73, 76, 77, 79–81, 84, 85, 88

OSA order sorting aperture 15–17

PGD projected gradient descent 25, 30, 31, 38, 39, 42, 56, 57, 63, 68, 73, 76, 88

ROI region of interest 3, 37, 38, 40–42, 46, 47, 51, 80, 86, 87, 113, 114

SNR signal-to-noise ratio 57, 66, 107

SPEC spectrum 102, 106, 110

TC Tamura coefficient 102

TF transmission function 60, 64, 72

ToG Tamura coefficient of the gradient 102, 106, 109, 113

TR truncation 41–47, 49, 50, 72, 76, 77, 79, 88

VAR variance 102, 103, 106, 110

WR weak reconstruction 67, 72, 76, 77, 79, 88

Introduction

1

Imaging techniques are one of the most important tools for investigating condensed matter. Microscopic measurement setups make it possible to decipher the properties of matter down to the smallest details. In contrast to a classical light microscope, we can significantly improve the properties of a microscopy experiment by using a coherent light sources and thus enabling imaging with the holographic principle [1]. In recent decades, light sources have been continuously improved up to the availability of synchrotron radiation sources with high brilliance, that enable holographic measurements with hard X-rays [2–8]. Such experiments allow a spatial resolution in the range of nanometers.

In holography, the image contrast is the result of two types of interaction between light and matter: The illumination attenuation and the shift of the phases, caused by a measured specimen. The phase shift of the illumination produces the strongest image contrast and encodes information that is otherwise unavailable when using an incoherent illumination. Unfortunately, even modern detectors are not capable of completely capturing a complex wave-field. The recordings are always integrated over a certain period of time, whereby the phase information is lost and only the intensities remain as a measured hologram. The resulting problem that the phases have to be recovered is widely known as the phase problem [9–13]. To date, a variety of approaches have been developed to determine the complex refractive index of a measured sample with spatial resolution. The possible approaches range from one-step methods that directly invert the contrast transfer function [14] to iterative algorithms such as the famous Gerchberg-Saxton algorithm [15] and its successors [16–19]. Those algorithms are well established and commonly used in the community of synchrotron radiation sources to reconstruct weakly interacting samples from one or more intensity images. Strongly interacting objects with high phase shifting values and non-negligible absorption are much harder to reconstruct. For such objects, retrieving the complex refractive index from mixed contrast holograms requires the incorporation of advanced prior knowledge and prohibits typical simplifications like the linearization of the forward operator or constraints on the measured material. Here, the appearance of reconstruction artifacts, phase wrapping, algorithm stagnation, long computation times and quantitatively wrong results are omnipresent problems that need to be solved [20, 21].

With further advances the field of X-ray microscopy, the complexity of the measured objects is continuously increasing, requiring the refinement of available algorithms and the development of novel approaches. Furthermore, due to the increasing amount of image data produced at synchrotron facilities, the demand for robust and fast reconstruction algorithms increases, and the automatic optimization of reconstruction parameters becomes an obligation if *in situ*/*operando* studies are to be performed [22–25]. In such scenarios, the reconstruction must be performed under very difficult conditions. The algorithm must then reconstruct the refraction index of a large variation of different objects as robustly as possible, generate a result as quickly as possible and have the smallest possible number of parameters that need to be adjusted manually, while the reconstruction parameters should be reduced to a minimum. This means that restrictive or time-consuming measurement setups or algorithmic regularization techniques must be avoided. The consequence is that we have to abandon commonly used techniques like multi-distance measurements or regularization with a spatial support constraint and total variation. Furthermore, all setup parameters must be known exactly during the experiment, which requires automatic optimization of the model parameters.

1.1 Contributions

This thesis deals with the development of a reconstruction algorithm for X-ray near-field holography (NFH). The aim is to reconstruct the projected complex refractive index of an object from single holograms, without a spatial support constraint. As a reference, Alg. 0, which is derived in Ch. 3 was used, which is based on the refAP algorithm of Wittwer et al. [20] with an omitted spatial support constraint. The main contributions are separated into two chapters. One chapter deals with the analysis of reconstruction artifacts and the development of an artifact suppressing algorithm. The second chapter extends this algorithm with the automatic optimization of the forward model. The contribution in those chapters are as follows.

1.1.1 Development of an artifact suppressing reconstruction algorithm

In Ch. 4, a novel algorithm for NFH is developed that suppresses reconstruction artifacts. Most parts of this chapter were already published in a peer-reviewed journal [21]. The data and code underlying the results of the publication were published in a software framework in [26]. The publication and the content of this chapter contributes to current research by the following:

- Removing the spatial support constraint of [20] yields multiple types of reconstruction artifacts. The cause of reconstruction artifacts were identified and the artifacts were divided into appropriate meaningful categories. The categories could be decoupled from the reference algorithm and thus be generalized which makes them relevant for other reconstruction methods.

- For each artifact type, up to two techniques were developed for preprocessing and the iterative reference algorithm in order to suppress them. The techniques are generalized and independent from each other, making them relevant for other reconstruction methods.

- Subsequently, all techniques were combined into a new artifact suppressing reconstruction method (ASRM). The computational time was reduced by a factor of three with respect to the reference algorithm. In preparation for future in-situ experiments at experimental stations of synchrotron radiation sources, this algorithm is the first for NFH that fulfills all conditions in the following list:
    - For time reasons, the reconstructions are carried out with only a single hologram as input data. The recording of several holograms per reconstruction, e.g. by ptychographic methods [27–29] or the recording of holograms at several distances [30, 31], is dispensed with.
    - A spatial support constraint [32, 33] is also omitted for reasons of time and to enable the reconstruction of objects that are larger than the region of interest (ROI). This applies to both a static constraint and automatic adaptation, e.g. via shrinkwrap [34].
    - To ensure the variability of the objects to be reconstructed, a material constraint [35, 36] is not used.
    - The constraints used for the final reconstruction result are exclusively data-driven or physical in nature to avoid quantitatively incorrect results. Specifically, these are a data driven least-squares approach, the non-negative electron density and energy conservation constraints [37, 38]. All other developed techniques that alter the reconstruction result with respect to quantitative results, are only used in a warm-up phase.
- The new algorithm was tested on experimental data with successively increasing interaction strength. A reconstruction was carried out with a biodegradable magnesium-based wire, which was also the first complete reconstruction. Previous publications on this dataset were only partly reconstructed [20, 23] although additional constraints were used.

1.1.2 Development of an autofocus algorithm

In Ch. 5, an autofocus algorithm is developed that includes the proposition of a novel error metric. Part of the forward model of the reconstruction algorithm is the so-called Fresnel number. The Fresnel number summarizes the geometry of the measurement setup into one scalar value and is often not known with sufficient precision. The beamline P05 at the PETRA III storage ring (DESY, Hamburg) uses a cone beam setup for nano-tomography. The distance between the focus of the used optic and the sample z_{01} can only be determined up to a precision of ±5 mm, during the experiment. Performing a reconstruction with the algorithm developed in Ch. 4 and an imprecise value for z_{01} results in images that are blurred due to a defocus effect. Most parts of this chapter were already published in a peer-reviewed journal [39]. The data and code underlying the results of the publication were published in a software framework in [40]. The content of this chapter contributes to current research by the following:

- This chapter investigated the requirements for an automatic optimization of this value in an *in situ*/*operando* setting. The importance that a focus metric also considers the used algorithm behind reconstructed images was outlined. This issue is typically disregarded in current literature.
- A new focus metric called model fit error (MFE) was developed that quantifies the reconstruction defocus by fitting the forward model to the measured hologram.
- Optimal reconstruction parameters for the MFE criterion in combination with the algorithm of Ch. 4 were determined.
- The robustness was demonstrated on strongly interacting objects. The quality of the generated metric curve yields comparable results with respect to a simulation and outperforms previous focus metrics with respect to experimental data.
- The feasibility of an automatic optimization of z_{01} was demonstrated for experimental data by applying a downhill simplex method.

1.2 Outline

The thesis is divided into the following chapters. Chapter 2 introduces the physical fundamentals of lensless imaging with a NFH setup and the assumptions made for the forward model. This is followed by Ch. 3, which derives the reference algorithm for the reconstruction of complex refractive indices. Furthermore, the data used for the evaluations in this work are described and the experiments from which the data originate are presented.

Chapter 4 analyzes the reconstruction artifacts that occur when using the reference algorithm without additional constraints. The artifacts are categorized and their causes are examined. For each category, up to two countermeasures are developed to suppress the artifacts in the reconstruction. The countermeasures are each applied on the reference algorithm presented in Ch. 3 as part of the data preprocessing, the optimization problem and the solver. The developed measures are then combined into a common algorithm, resulting in the artefact suppressing reconstruction method. In the last part, the new method is applied to several experimental data sets with increasing interaction strength. A comparison is also made between the combined method and the individual techniques with regard to remaining artifacts and the computing time required.

In Ch. 5, the method from Ch. 4 is extended by the automatic optimization of the forward model. First, the influence of imprecisely known distances on the reconstruction result is shown. The conditions are listed that a combination of reconstruction algorithm and error metric must fulfill so that the focus-to-sample distance can be optimized automatically. In the second half, a new model-based error metric is developed and embedded in an optimization problem, which is solved with a downhill simplex method. In the last part, a comparison is made between the new metric and the existing metrics in current literature. The comparison is carried out with simulated and experimental data. The feasibility of the developed automatic optimization algorithm of the forward model is demonstrated for experimental data.

Physical Fundamentals 2

2.1 Complex Index of Refraction

In comparison to optical microscopy, the wavelength and the coherence of the illumination in full-field microscopy at a synchrotron radiation light source are significantly different. The combination of a very short wavelength in the order of 1 Å and high coherence exposes a large amount of information about the measured object. The signal at the detector is dominated by two physical effects that occur during the interaction of the illumination with a specimen in the beam. The first is the absorption, resulting in the attenuation of the illumination. The second effect is the scattering of photons at atoms. Here, we consider only the low-energy limit of the Compton effect, the Thomson scattering.

Both effects alter the illumination during the wave propagation through the object and leave a pattern in the wave-field that arrives at the detector. The effects can be encoded as one common complex number, the complex index of refraction n. This is often expressed in the form

$$n(x, y, z) = 1 - \delta(x, y, z) + i\beta(x, y, z), \tag{2.1}$$

along the spatial coordinates (x, y, z). Here, $\beta \in \mathbb{R}$ describes the absorption, i.e the attenuation and $\delta \in \mathbb{R}$ the dispersion, i.e. phase shifting properties of an object.

In the following, we go into the details of the physical mechanism behind the complex refractive index and how it is related to the measured hologram at the detector. We further derive the projection approximation for weakly scattering and thin objects to remove the z coordinate dependency from Eq. 2.1 and to simplify the reconstruction problem. Information can be found in [41] and [42], among others.

2.1.1 β - Photoelectric Absorption

The absorption of photons in matter is known as the photoelectric absorption and is illustrated in Fig. 2.1a. In this case, an electron bounded to an atom is ejected from one of the bounding shells into the continuum. The photon interacts with the atom and excites it into a state, where an electron is ejected. Removing an electron from one of the shells ionizes the atom and leaves it in an unstable energy state. The hole is then refilled by the two following mechanisms.

The first one is illustrated in Fig. 2.1b and is the Fluorescent X-ray emission.

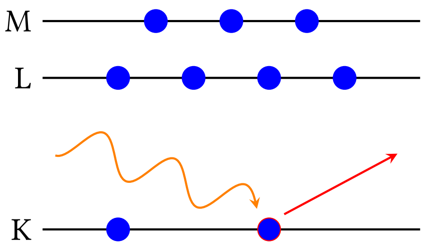

(a) Photoelectric absorption

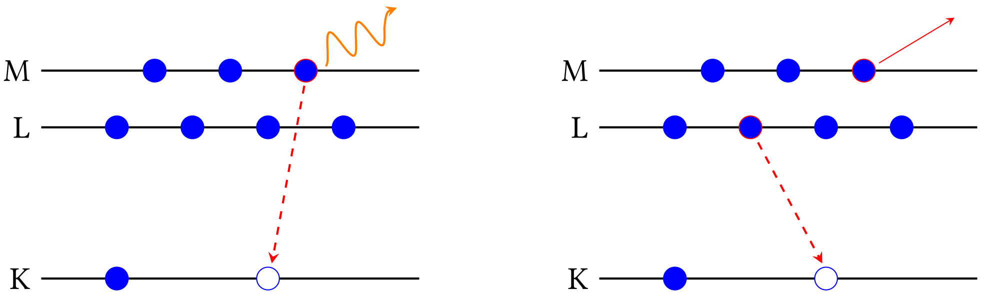

(b) Fluorescence radiation

(c) Auger electron emission

Figure 2.1: Illustration of the photoelectric absorption of X rays (a), followed by two effects: (b) Fluorescence radiation and (c) Auger electron emission. Electron movements are indicated by red arrows and radiation by an orange wave. (a) The energy of the incoming X-ray radiation is transformed to an electron, which is then ejected from its shell. The atom enters an unstable state with an electron hole that needs to be refilled. (b) The electron hole is filled by one of the outer shell electrons from the L or M shell. In the drawing, an electron from the M shell moves to the K shell and the difference between the binding energies of both shells is released as fluorescence radiation. (c) Alternatively is the released energy transformed to a second electron in the same atom. The second electron is then ejected and the remaining atom is energetically stable.

Here, an electron from one of the outer shells fills the created hole in the inner shell. In this course, the electron releases energy in form of radiation that is called fluorescence radiation. The energy of the radiation is exactly equal to the difference between the binding energies of the two involved shells. The radiation has thus a very discrete energy spectrum. The fluorescence radiation can be emitted into every direction. To measure fluorescence radiation, it is common to place the detector in a 90° angle to the illumination direction, where almost no Thomson scattering (Sec. 2.1.2) appears in the signal.

The second mechanism is the Auger electron emission and is illustrated in Fig. 2.1c. An electron from one of the outer shell fills the created hole in the inner shell. However, instead of emitting fluorescence radiation, the released energy is transferred to a second electron of the same atom, which is ejected in this course. The energy state of the remaining atom is stable again and no further fluorescence radiation emitted.

The photoelectric absorption can be quantified by a differential, which is the number of photons $\mathrm{d}N$ absorbed per material thickness $\mathrm{d}z$ with

$$\frac{\mathrm{d}N}{\mathrm{d}z} = -Nv\sigma. \tag{2.2}$$

Here, the absorption is described by the total number of photons N times the Naperian attenuation coefficient $v\sigma$ with the absorption cross section σ of a specific molecule and v the number of molecules. The absorption cross section is material dependent and given by

$$\sigma = (\mu_\Delta/\rho)\frac{M}{L} \tag{2.3}$$

where μ_Δ is the mass absorption coefficient, ρ the mass density, M the molar mass and L the Avogadro constant. From the perspective of photons as an electromagnetic wave-field, Eq. 2.2 can be directly related to intensities by a differential of the intensity attenuation $\mathrm{d}\mathcal{I}$ per thickness $\mathrm{d}z$ with

$$\frac{\mathrm{d}\mathcal{I}}{\mathrm{d}z} = -\mu_\Delta \mathcal{I}_0. \tag{2.4}$$

Solving the differential equation yields the Intensity $\mathcal{I}(z)$, parameterized by the object thickness z, which is also known as the Beer-Lambert law:

$$\mathcal{I}(z) = I_0 e^{-\mu_\Delta z}. \tag{2.5}$$

The attenuation coefficient μ_Δ can be derived from the absorption cross section Eq. 2.3 by a reformulation and a sum over all involved materials with

$$\mu_\Delta = L\sum_j (\rho^j \sigma^j)/M^j. \tag{2.6}$$

In the refractive index of a material, the absorption property is encoded into a single scalar value β:

$$\text{Absorption} : \beta \in \mathbb{R},\ 0 < \beta \ll 1. \tag{2.7}$$

This value is related to the absorption coefficient μ, by also taking the wave number k of the illumination and the object thickness d into account with

$$\mu = 2\beta k d. \tag{2.8}$$

The β values of different materials can have been widely studied and can be e.g. found in [43, 44].

2.1.2 δ - wave-field Dispersion

The Thomson scattering describes the elastic scattering of X rays at a free electron. It can be interpreted as the low-energy limit of the inelastic Compton scattering. The scattering signal at the detector can be characterized by a differential, the so-called differential scattering cross section. The cross section σ is a quantity that describes the scattering efficiency of a material. The efficiency is given by the differential cross section, defined by the scattered photons which arrive at the detector with respect to the total number of incident photons, normalized to the areas. The differential cross section for scattering at a single free electron is defined by

$$\frac{\mathrm{d}\sigma}{\mathrm{d}\Omega} = \frac{\Phi_{\mathrm{det}}}{\mathrm{d}\Omega} \cdot \frac{1}{\Phi_{\mathrm{ref}}}, \tag{2.9}$$

where Φ_{ref} is the photon count per second of the illumination, Φ_{det} is the photon count per second at the detector and $\mathrm{d}\Omega$ is the opening solid angle. This is illustrated in Fig. 2.2. The solid angle is the detector area divided by the distance squared A/r^2, where A is a circular area. This quantity is a discrete measure from the particle model of a photon and is related to the probability that a single photon is observed a the detector at a specific point of time. For wave model based equations, we should express the differential cross section with respect to an electromagnetic wave-field. The transition can be done by first using the intensity $\mathcal{I}_{\mathrm{det}}$ instead of photon counts per second:

$$\frac{\mathrm{d}\sigma}{\mathrm{d}\Omega} = \frac{\mathcal{I}_{\mathrm{det}}(r^2\mathrm{d}\Omega)}{\mathrm{d}\Omega} \cdot \frac{1}{\mathcal{I}_{\mathrm{ref}}}, \tag{2.10}$$

and then calculating the intensity as a time average $< \cdot >$ over the magnitude of the Poynting vector $\vec{S} \in \mathbb{R}^3$ of the electromagnetic wave-field, perpendicular to the observed area with

$$\vec{S} = \vec{E} \times \vec{H} \tag{2.11}$$

$$\mathcal{I} =< |\vec{S}| > . \tag{2.12}$$

Here, $\vec{E} \in \mathbb{R}^3$ is the electric field, $\vec{H} \in \mathbb{R}^3$ is the magnetic field strength and × is the cross product. The differential cross section is then given by

$$\frac{\mathrm{d}\sigma}{\mathrm{d}\Omega} = \frac{< |\vec{S}_{\mathrm{det}}| > r^2}{< |\vec{S}_{\mathrm{ref}}| >}. \tag{2.13}$$

Because we are only observing magnitudes, we can substitute the magnetic field $\vec{H}$ of the Poynting vector with the electrical $\vec{E}$ field, without changing the result by:

$$< |\vec{E} \times \vec{H}| >=< |\vec{E} \times \frac{\vec{B}}{\mu_0}| >= \frac{1}{\mu_0 c} < |\vec{E}|^2 >, \tag{2.14}$$

where $\vec{B}$ is the magnetic flux density, μ_0 magnetic permeability of vacuum and c the speed of light. Inserting into the differential cross section yields

$$\frac{\mathrm{d}\sigma}{\mathrm{d}\Omega} = \frac{< |\vec{E}_{\mathrm{det}}|^2 > r^2}{< |\vec{E}_{\mathrm{ref}}|^2 >}. \tag{2.15}$$

From the point of view of classical physics with a wave-field model, the scattering process at a non-relativistic, free electron can be described by the following. The electric field of the photon meets, which interacts with the electron charge and excites it into an oscillation that follows the electric field. An oscillation always contains an acceleration term, which, in the case of a charged particle, leads to the generation of radiation. This effect is also known in the case of bremsstrahlung and the generation of synchrotron radiation. Here, it leads to the scattering of X rays. Due to the periodic acceleration, the electron becomes an oscillating electromagnetic dipole whose direction of oscillation depends on the polarization of the incoming electric field. Since a dipole does not radiate an electromagnetic field uniformly, the polarization of the arriving wave-field in the cross-section is therefore observation position dependent and must be taken into account. The illumination wave-field $\vec{E}_{\mathrm{ref}}$ is our point of reference and remains position independent. The electric wave-field magnitude $|\vec{E}_{\mathrm{ref}}|$ at the detector with respect to the reference attenuates by the observation distance and the polarization. The polarization of $\vec{E}_{\mathrm{det}}$ is given by the polarization of $\vec{E}_{\mathrm{ref}}$ minus the orthogonal projection onto the observation vector $\vec{r}_{\mathrm{det}}$, i.e. the proportion of polarization $\mathrm{pol}(\vec{E}_{\mathrm{det}})$ in the direction of observation with

$$\mathrm{pol}(\vec{E}_{\mathrm{det}}) = \vec{e}_{\mathrm{ref}} - (\vec{e}_{\mathrm{ref}} \cdot \vec{r}_{\mathrm{det}}) \cdot \vec{r}_{\mathrm{det}}. \tag{2.16}$$

The intensity at the detector with respect to the reference then holds

$$< |\vec{E}_{\mathrm{det}}|^2 >= \frac{1}{\mu_0 c} r_0^2 (1 - (\vec{e}_{\mathrm{ref}} \cdot \vec{r}_{\mathrm{det}})^2) \frac{1}{r^2} |E_{\mathrm{ref}}|^2, \tag{2.17}$$

where · is the scalar product. The parameter r_0 is the classical electron radius. Substituting this into Eq. 2.15 yields

$$\frac{\mathrm{d}\sigma}{\mathrm{d}\Omega} = r_0^2 (1 - (\vec{e}_{\mathrm{ref}} \cdot \vec{r}_{\mathrm{det}})^2), \tag{2.18}$$

where r_0 is also known as the classical electron radius or Thomson scattering length:

$$r_0 = \frac{e^2}{4\pi\epsilon_0 m_0 c^2}. \tag{2.19}$$

The derived equation Eq. 2.18 is the differential cross-section for scattering at a single electron and is proportional to the classical electron radius squared r_0^2. In matter, this process takes place on a large scale. The scattering can also be described on the size scale of atoms. For this purpose, the differential cross-section is extended with the so-called atomic form factor $f(K)$, which corresponds to the Fourier transform of the electron density. With the assumption that a photon only scatters once, the cross section is then calculated by:

$$\frac{\mathrm{d}\sigma}{\mathrm{d}\Omega} = r_0^2(1 - (\vec{e}_{\mathrm{ref}} \cdot \vec{r}_{\mathrm{det}})^2)|f(K)|^2, \tag{2.20}$$

where K is the scattering vector towards observation point. The form factor magnitude $|f(k)|$ can be measured experimentally, e.g. with crystallography.

From the polarization term of Eq. 2.20, it is evident that the smallest signal is measured at a 90° angle with respect to the propagation direction, i.e. in direction of $\vec{e}_{\mathrm{ref}}$. Consequently, most of the scattering signal is recorded if the detector is placed at small angles to the propagation direction of $\vec{E}_{\mathrm{ref}}$. In this case, it is also possible to acquire holograms with X rays (Sec. 2.2) and to simplify the description of free-space propagation for small scattering angles (Sec. 2.3).

Note that the Thomson scattering is an energy conservation mechanism and only results in the dispersion of the illumination, without absorbing energy. On the length scale of image pixels, this effect describes the induced phase shift of the incoming wave-field, depending on the material. In the refractive index, this property is encoded into a single scalar value δ:

$$\text{Dispersion: } \delta \in \mathbb{R},\ 0 < \delta \ll 1. \tag{2.21}$$

The dispersion quantity δ is related to the Thomson scattering by the atomic form factor at $K = 0$ and the Thomson scattering length r_0 with

$$\delta = r_0 f(0) \frac{2\pi}{k^2} L \frac{\rho}{m_A}, \tag{2.22}$$

where k is the wave number of the illumination, ρ is the mass density, m_A is the atomic mass and L is the Avogadro constant. This value is related to the induced phase shift ϕ_Δ of a weakly scattering object of thickness d by

$$\phi = -k\delta d. \tag{2.23}$$

The δ values of different materials can have been widely studied and can be e.g. found under [43, 44].

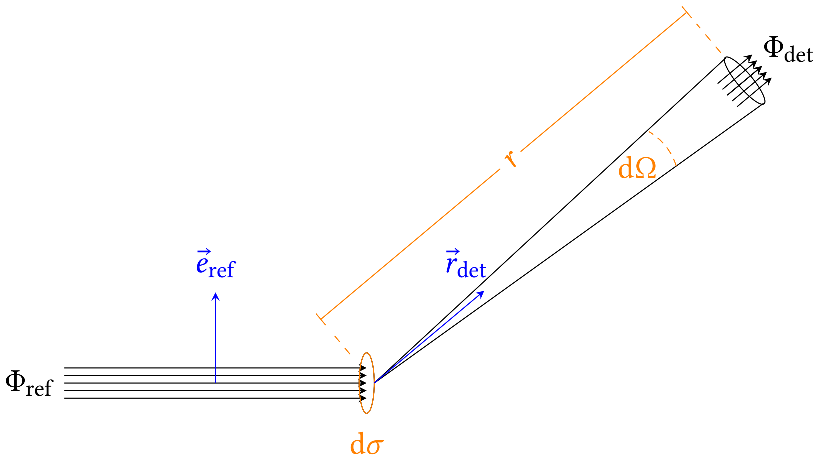

Figure 2.2: Illustration of the differential cross section that can be used to describe the scattering signal strength at the detector. The differential cross section for scattering at a non-relativistic single and free electron is described by the photons flux Φ_{det} at the detector with respect to the total photon flux Φ_{ref} inside of a unit area $\mathrm{d}\sigma$ in the reference direction $\vec{e}_{\text{ref}}$. The photons flux Φ_{det} describes only the photons that are scattered into the solid angle $\mathrm{d}\Omega$ in observation direction $\vec{r}_{\text{det}}$. The differential cross-section value is independent from the observation distance r and depends only on the angle between $\vec{e}_{\text{ref}}$ and $\vec{r}_{\text{ref}}$ as well as the Thomson scattering length r_0 of Eq. 2.19.

2.1.3 Projection Approximation

In this thesis, a projection approximation for the measured object is applied, which is described in [42] and works as follows. In the presence of a scattering and absorbing object with the refractive index $n(x, y, z)$ and with respect to a monochromatic wave-field $\psi(x, y, z)$ of wavelength λ and wave number $k = \frac{2\pi}{\lambda}$, the Maxwell equations describe the wave properties whose solutions are also solutions of the modified Helmholtz Equation

$$\left[\nabla^2 + k^2 n^2(x, y, z)\right] \psi(x, y, z) = 0. \tag{2.24}$$

We choose a separation approach for ψ and introduce the X-ray beam ψ as a monochromatic plane wave $\exp(ikz)$ in vacuum, combined with an envelope function A, which describes the amplitude variation such that

$$\psi(x, y, z) = A(x, y, z) \exp(ikz) . \tag{2.25}$$

We further assume that the direction propagation is z and introduce the paraxial approximation that the amplitude of ψ varies only slowly in propagation direction. The second derivative of A with respect to z becomes:

$$\frac{\delta^2}{\delta z^2} A(x, y, z) \approx 0. \tag{2.26}$$

The scattering of the beam is then described by the inhomogeneous paraxial equation, which we get by inserting $\psi(x, y, z)$ in Eq. 2.24:

$$\{2ik\frac{\delta}{\delta z} + \nabla^2_{xy} + k^2[n^2(x, y, z) - 1]\}A(x, y, z) = 0. \tag{2.27}$$

In this work, we assume a sufficiently thin object such that the scattering inside of the object with refractive indices $n(x, y, z)$ is sufficiently weak to assume that the paths of the incoming beam rays do not change. We follow the projection approximation of Paganin, Sec. 2.2, Eq. 2.39 [42]. We are then able to neglect the Laplacian ∇_{xy} of Eq. 2.27 and get the differential equation for the scattered beam

$$\frac{\delta}{\delta z}A(x, y, z) = \frac{k}{2\mathrm{i}}[1 - n^2(x, y, z)]A(x, y, z). \tag{2.28}$$

We can now calculate the exit wave-field ψ_{exit} behind a sample of thickness d by solving this differential equation under a known incident beam at position $z = 0$ with description $\psi_0 = A(x, y, 0)$ such that

$$\psi_{\text{exit}}(x, y) = A(x, y, d) = \exp\left(\int_0^d \frac{k}{2\mathrm{i}}[1 - n^2(x, y, z)]\; dz\right)\psi_0. \tag{2.29}$$

We evaluate the term $1 - n^2(x, y, z)$, while for readability neglecting the spatial coordinates, which is given by

$$1 - n^2 = -\delta^2 - 2\mathrm{i}(1 - \delta)\beta + 2\delta + \beta^2. \tag{2.30}$$

In practice, δ and β for the measured materials are usually much smaller than one by some orders of magnitude. Under the condition $\delta, \beta \ll 1$, we assume

$$\delta^2, \beta^2 \approx 0, \tag{2.31}$$

$$1 - \delta \approx 1, \tag{2.32}$$

which yields the approximation

$$1 - n^2 \approx 2(\delta - \mathrm{i}\beta) \tag{2.33}$$

Inserting this into Eq. 2.29 gives us the final projection approximation of the complex refractive index for the exit wave-field ψ_{exit} behind the measured object with

$$\psi_{\text{exit}}(x, y) = \exp\left(-\mathrm{i}k \int_0^d \delta(x, y, z) - \mathrm{i}\beta(x, y, z)\; dz\right)\psi_0. \tag{2.34}$$

To simplify the notation of these equations, we substitute the argument of the exponential function and define the object $\tilde{O}$ in refractive notation by

$$\tilde{O}(x,y) = -k \int_0^d \delta(x,y,z) - \mathrm{i}\beta(x,y,z)\; dz = \phi(x,y) + \mathrm{i}\frac{1}{2}\mu(x,y). \tag{2.35}$$

We further also omit in the following the notation of the spatial coordinates for Eq. 2.35. The reconstructions in this work will aim to recover the projected refractive index approximation $\tilde{O}$ from the measured data, where ϕ encodes the phase shifting properties and μ encodes the attenuation properties of the object.

2.2 Full-Field X-Ray Microscopy

In microscopy, a divergent beam from a light source is typically used to optically magnify an illuminated object and make very small structures visible. Microscopy with coherent and monochromatic hard X rays is an established method to investigate condensed matter since with coherent light, both effects of the complex refractive index, as described in Sec. 2.1, can be exploited for imaging [1, 27, 30, 45]. With X rays, the interior of closed samples can be investigated without mechanically damaging the object and the hard X-ray regime allows a resolution up to nanometers and a considerable penetration depth of the illumination [7]. Using a full-field microscopy setup [1, 45, 46] is especially attractive for biological samples as structures in the length scale from mm to nm [14, 46] can be made visible while minimizing the radiation dose by acquiring whole images with one single exposure. Placed on a rotational stage, whole tomograms of samples can be measured and reconstructed by using phase contrast and absorption contrast information. This section describes the basics of the NFH setup which was used in this work. We go into the details of the setup for lensless imaging and the resolution that can be theoretically achieved. Depending on the setup geometry, we further define different measurement regimes that determine which forward model has to be used.

2.2.1 Lensless Full-Field Imaging

The following describes a lensless setup for full-field microscopy with hard X rays as shown in [46], following the holographic principle. A sketch is shown in Fig. 2.3. Although it contains a focusing optic, the setup is called lensless because there is no objective lens between the sample and the detector. The setup is as follows: An X-ray source, outside of the scope of this figure, creates a coherent and monochromatic X-ray beam which enters the sketch from the left side. The beam is focused by a fresnel zone plate (FZP) [47–49]. An FZP is a focusing optic, which consists of a circular absorbing or phase grating. For imaging, we are interested in the first order cone and so the others have to be blocked. The zero order is the direct beam that would damage the detector if let through. The direct beam is blocked by two systems, a beam stop and an order sorting aperture (OSA). A beam stop that is positioned directly behind the FZP blocks the part of the zero order diffraction which coincidences with the first order diffraction. In this setup, the beam stop not only blocks the direct beam but also the whole bottom half of all cones, leaving the top half cone for imaging. In the focal spot at distance f behind a FZP lies the OSA, which blocks the rest of the direct beam as well as the cones from other diffraction orders. For full-field imaging, the sample has to be positioned behind the focus in a distance such that the sample is fully illuminated by the X rays. Because of the cone shape of the beam, the image of the sample is magnified. The magnification depends on the opening angle of the cone, the sample position and the position of the detector. For the following, we define three numbers that correspond to three coordinates in the experimental setup. The number 0 is the focal spot position of the FZP, 1 is the sample position and 2 is the position of the detector. We further define the following distances:

$$z_{01}\text{: Distance between focal spot and sample,} \tag{2.36}$$

$$z_{12}\text{: Distance between sample and detector,} \tag{2.37}$$

$$z_{02}\text{: Distance between focal spot and detector.} \tag{2.38}$$

The focal length f is approximately given by the radius of the FZP r_f and the numerical aperture N_A:

$$\mathrm{f} \approx \frac{r_f}{N_A}. \tag{2.39}$$

2.2.2 Measurement Regimes

We consider an object that is illuminated by a coherent, monochromatic and a parallel X-ray beam. The object interacts with the X rays according to Sec. 2.1 by absorption and phase shifting. Behind the object exits a wave-front which in an idealized model is still monochromatic, with amplitude variations and different phases, depending on the spatial position. The propagation behind the object can be described by the Huygens' Principle, i.e. the wave-front starts to self-interact, described by the concept that each spatial position behind the object is the source of a new spherical wave. This is crucial to acquire a phase contrast image with only intensity measurements available. The wave-front needs to be propagated far enough such that the detector, which has a limited spatial resolution, is capable to capture the interaction above the signal-to-noise ratio. Only then, the data contains sufficient information to reconstruct the object properties, i.e. the complex refractive index per spatial position. In this sense, the acquired data by the detector can be sorted into different categories, depending on the overall geometry of the measurement setup. For this purpose, the characteristic length z_c describes when certain approximations of the free-space propagation become invalid. In this holographic regime, the outgoing waves of all parts of the object interact with each other. With respect to the size of the measured object w_o and the wavelength λ of the illumination, the characteristic length z_c is given by

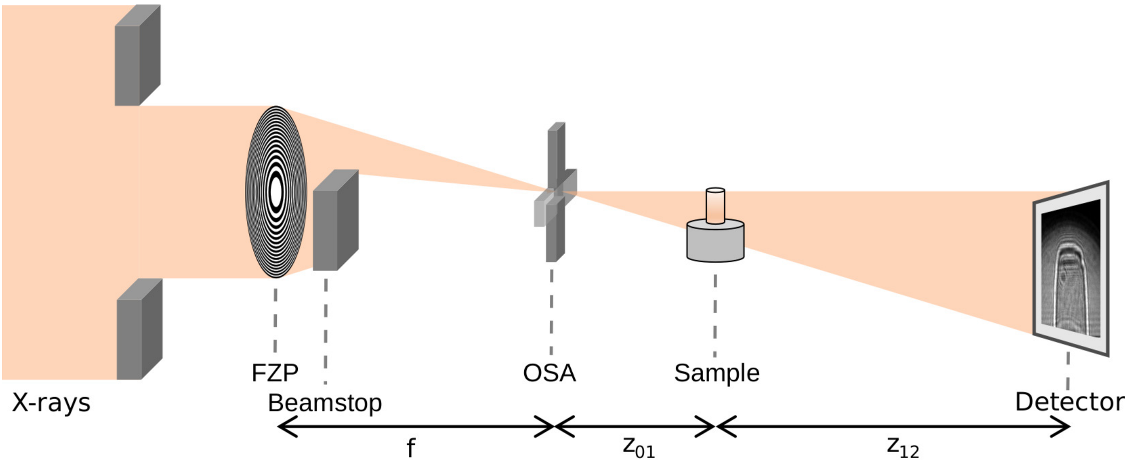

Figure 2.3: Lensless, full-field imaging setup, based on a FZP for NFH microscopy. The image has been adapted from [46]. The FZP focuses the incoming coherent monochromatic X rays to the focal spot located at a distance f behind the FZP. There, an OSA is placed that blocks the higher diffraction orders of the FZP. The sample is put on a sample holder on a rotation stage into the diverging cone-shaped beam of the FZP at a distance z_{01}. Behind the sample, the X rays propagate to the detector that is placed at the sample-to-detector distance z_{12}. To protect the detector from radiation damage, the direct beam is blocked by a beamstop behind the FZP.

$$z_\mathrm{c} = \frac{w_o^2}{\lambda}. \tag{2.40}$$

The categories are then defined by comparing the characteristic distance to the effective distance z_eff between the illuminated sample and the detector. For very large distances, the free-space propagation can be described by a simple Fourier transform with respect to the spatial coordinates. The corresponding category is the Far-Field regime and holds as long as

$$\text{Far-Field: } z_\mathrm{eff} \gg z_\mathrm{c}. \tag{2.41}$$

The approximation breaks down if the effective distance is reduced and reaches the proximity of the characteristic length. The corresponding category is called Fresnel regime and holds if

$$\text{Fresnel: } z_\mathrm{eff} \approx z_\mathrm{c}. \tag{2.42}$$

In this case, the description of the wave propagation becomes more complex and a different convolution kernel than the Fourier transform is required. The convolution kernel is presented in Sec. 2.3. Sometimes, this regime is also called Near-Field regime and somtimes additionally divided into two subcategories, the Fresnel and the Near-Field regime. The Near-Field is then defined for distances that hold

$$\text{Near-Field: } z_{\text{eff}} \ll z_{\text{c}}. \tag{2.43}$$

The final regime is the contact region, where the measured data yields only images with absorption contrast, if

$$\text{Contact: } z_{\text{eff}} = 0. \tag{2.44}$$

Given the projection approximation of Sec. 2.1.3, the intensities at each spatial point can then be calculated by applying the Beer-Lambert law.

A visualization of the different hologram types that can be expected in these regimes is shown in Fig. 2.4. The simulated object is a phantom which consists of four dots, two pure absorption objects (black dots) and two pure phase objects (gray dots). In the contact regime, only an absorption contrast is visible, given by the two absorption objects. In the Far-Field regime, the hologram can be described by a two-dimensional Fourier transform of all four objects. In between, near-field/Fresnel regime typical fringes appear around all objects. It can also be seen that phase-shifting results a stronger contrast in this regime than absorption.

Note that the characteristic length and therefore the related propagation distance for each regime, strongly depends on the length scales we want to measure. The consequence is, that the regime is mostly predetermined and very difficult to change. In this work, we consider the near-field/Fresnel regime.

2.2.3 Spatial Resolution

The theoretical resolution limit for imaging with FZPs is directly related to the length scale of the outer most structure [46, 50]. In general, the resolution with a focusing optic is limited by the Rayleigh criterion, which defines the numerical aperture size that is at least required to achieve a certain resolution. Given a numerical aperture N_A, the resolution Δ_r is then approximately calculated by

$$\Delta_r \approx 1.22 \frac{\lambda}{2N_A}, \tag{2.45}$$

where λ is the wavelength of the illumination. The parameter Δ_r is equivalent to the diameter of the focal spot, which lies at distance f with:

$$f \approx \frac{r_n^2}{n\lambda}, \tag{2.46}$$

where n is the number of zones, r_n is distance from the outer zone border to the center of the FZP. For each zone n on the FZP (phase shifting and free zone), the width w_n of the zone follows

$$w_n = \frac{r_n}{2n}. \tag{2.47}$$

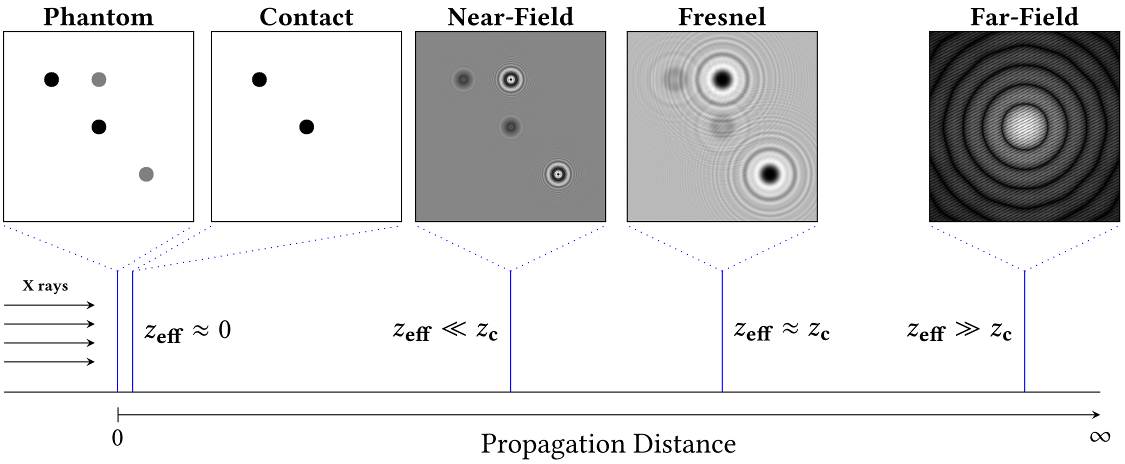

Figure 2.4: Visualization of the different hologram types that can be expected in various detector distances. The simulated object is a phantom which consists of four dots, two pure absorption objects (black dots) and two pure phase objects (gray dots). The regimes are usually divided into the contact, the near-field, the Fresnel and the Far-Field regime. In the contact regime, only an absorption contrast is visible. In the Far-Field regime, the hologram can be described by a two-dimensional Fourier transform. In between, in the near-field and Fresnel regime, regime-typical fringes appear around the objects.

The numerical aperture is defined as the sine of the opening angle α of the half cone, which is approximately the ratio of the FZP radius to the focal length. For a circular FZP in vacuum, where the blocking zones completely block the illumination, the numerical aperture $N_{A,m}$ for each diffraction order m can with this approximation also be calculated by

$$N_{A,m} = \sin \alpha_m \approx \frac{m\lambda}{2w_n}. \tag{2.48}$$

Since we are only interested in the first diffraction order, we can set $m = 1$ and insert Eq. 2.48 into Eq. 2.45 yielding the resolution limit Δ_r, depending on the outer zone width w_n:

$$\Delta_r = 1.22\ w_n. \tag{2.49}$$

The resolution limit Δ_r describes the spot size of the focus. It thus defines the spatial resolution for the axes orthogonal to the beam direction. For the depth resolution, we also have to consider the shape of the focus in beam direction. The beam has a Gaussian profile, such that the change of the beam width w_b is not linear, especially in the proximity of the focus. The Rayleigh criterion in depth therefore results in different values and the depth resolution Δ_d is limited by

$$\Delta_d = \frac{\lambda}{N_A^2}. \tag{2.50}$$

The depth resolution is especially important for the projection approximation of Sec. 2.1.3. It determines the length at which the two objects can no longer be distinguished in the direction of the beam, i.e. their displacement is not recognizable. This is valid for displacements in positive and negative directions and we can define the area, where an object appears sharp as the depth of focus DOF:

$$\mathrm{f} \pm \frac{1}{2}\mathrm{DOF} = \mathrm{f} \pm \Delta_d, \tag{2.51}$$

$$\mathrm{DOF} = 2\Delta_d. \tag{2.52}$$

A necessary condition for the projection approximation is that the whole measured object is smaller than the DOF. Is the object placed in a defocus position, like in Fig. 2.3, it is also common to refer to the DOF as the depth of field.

2.3 Forward Model

The hologram is an intensity image of the arriving wave-field, integrated over time, where the phase information of the complex quantity is lost. This problem is well known as the phase problem [9–13].

The measurement process of a hologram is modeled by propagating ψ_{exit} of Eq. 2.29 to the detector and removing the phase information by taking the squared magnitude of the propagated wave-field. With the assumption that the object is illuminated by an aberration free coherent beam with constant amplitude, the equation for the exit wave ψ_{exit} behind the object $\tilde{O}$ is given by

$$\psi_{\mathrm{exit}}(\tilde{O}) = \exp\left(\mathrm{i} \cdot \tilde{O}\right) \sqrt{a_0} \exp\left(\mathrm{i} \cdot \phi_0\right), \tag{2.53}$$

with $a_0 \in \mathbb{R}$ being the illumination amplitude and $\phi_0 \in \mathbb{R}$ being the illumination phase offset. We summarize the processes of the object illumination, the interaction with the X rays and the wave-field propagation to the detector into an operator $\mathcal{D}_{\mathrm{Fr}}(\tilde{O})$ and take the squared magnitude to model the measurement $\mathcal{I}_{\mathrm{det}}$:

$$\mathcal{D}_{\mathrm{Fr}}(\tilde{O}) = \mathcal{F}^{-1} \circ \exp\left(-i \cdot \pi \frac{(k_x^2 + k_y^2)}{\mathrm{Fr}}\right) \circ \mathcal{F} \circ \psi_{\mathrm{exit}}(\tilde{O}) \tag{2.54}$$

$$\mathcal{I}_{\mathrm{det}} = \left|\mathcal{D}_{\mathrm{Fr}}(\tilde{O})\right|^2. \tag{2.55}$$

The operator $\mathcal{D}_{\mathrm{Fr}}$ is an approximation of the free space propagation for the near field and is called the Fresnel propagator in operator form [42]. Here, the function $\mathcal{F}$ describes the 2D Fourier transform of the wave-field and $\mathcal{F}^{-1}$ its inverse respectively with respect to the spatial coordinates (x, y) and frequency parameters (k_x, k_y). The Fresnel number Fr, which is relevant for the reconstruction of $\tilde{O}$, depends on the whole measurement setup and includes the geometry of the focusing object, the spatial distances between each setup component, the illumination energy and the dimensions of the detector pixel. In a parallel beam setting, the Fresnel number Fr is derived from the pixel size of the detector Δx, the wavelength of the source λ and the propagation distance between sample and detector z_{12} with

$$\mathrm{Fr} = \frac{\Delta x^2}{\lambda z_{12}}. \tag{2.56}$$

In order to enable microscopy through holographic imaging, the object has to be placed into a divergent beam in a defocused position. The Fresnel number Fr must then also incorporate the magnification through the cone beam, which can be derived from the Fresnel scaling theorem [42]. The theorem states that the cone beam setup can be transformed to an equivalent parallel beam setup by calculating a new effective propagation distance $z_{12}^* = Mz_{12}$ from the object magnification M. The divergent beam magnifies the sample by a factor

$$M = \frac{z_{01} + z_{12}}{z_{01}} \tag{2.57}$$

that is given by the proportion of the total propagation distance $z_{01} + z_{12}$ to the focus-object distance z_{01}. The Fresnel number Fr for an equivalent parallel beam becomes

$$\mathrm{Fr} = \frac{\Delta x^2}{\lambda M z_{12}}. \tag{2.58}$$

2.4 Data Noise Models

The forward model is only an approximation of the actual measurement system with simplifying assumptions about the physics, the measured object and the measurement instruments, including a perfectly coherent and monochromatic illumination and a perfectly precise detector. However, no system is perfect and each component in the measurement system, from the illumination, over the optics to the detector electronic, introduces an error with respect to the forward model. This leads to data noise which is either randomly distributed or results in patterns in the data with a distinct structure. Commonly, both different types are called unstructured and structured distortions. For a reconstruction, a noise model is needed that describes the assumptions how a measured hologram will deviate from an ideal hologram which is estimated by the forward model. Both types of noise are visualized in Fig. 3.1. The following sections will go into the details about the unstructured noise models that are common in X-ray imaging as well as into the sources of structured distortions and the assumptions that are made.

2.4.1 Structured Distortions

Structured distortions (Fig. 3.1a) impose distinct patters in the data. The source of those patterns are usually hardware components which are used in the measurement setup at the beamline. These hardware components then leave visible patterns in the measured hologram. Those patterns can for example be the structure of the FZP, dust particles on the hardware, windows of the vacuum tubes or fringes of the beamstop. Furthermore, the illumination during an experiment does not necessarily remain stable and can drift or can change otherwise. Also, storage rings are typically refilled with new electrons from time to time, resulting in sudden variations in illumination. Are these variations too strong over time, it can become challenging to separate the illumination from sample in a hologram. Even after normalizing the illumination, e.g. with a flat-field approach (Sec. 3.1), there is then a risk that refilling causes remaining patterns in the reconstruction input, i.e. structured distortions. For single shot imaging at free-electron lasers, the illumination pattern can change drastically between each shot.

A simple approximation of the structured distortions caused by the illumination or objects in the beam, is to introduce it as an additional scattering object in the measurement system. We can also apply the thin object approximation of Sec. 2.1.3 to this object. The beam ψ_0 is then distorted by a multiplicative perturbation component P such that the forward model for the measurements $\mathcal{I}_{\text{det}}$ becomes

$$\mathcal{I}_{\text{det}} = \left| \mathcal{F}^{-1} \circ \exp\left(-\mathrm{i} \cdot \pi \frac{(k_x^2 + k_y^2)}{\text{Fr}} \right) \circ \mathcal{F} \circ \exp\left(\mathrm{i}\tilde{O} \right) \; P \, \psi_0 \right|^2 . \tag{2.59}$$

Modeling the structured distortions as a scattering objects in the setup allows for a noise correction during the data preprocessing phase. The correction approach will be described in Sec. 3.1. Another source of structured distortions are vibrations of the system. Vibrations are rigid and non-rigid movements of the measurement components over time. They result in shifts, rotations or deformations of large structures. We assume here vibrations to be sufficiently small to ignore such type of deformations.

2.4.2 Unstructured Noise

Unstructured noise (Fig. 3.1b) is the most common type of noise that causes data distortions. In the case of imaging with X rays, the most important source of noise is photon noise and appears always for finite exposure times. Photon noise is a quantum effect that originates in the discrete nature of photons. The arrival of photons at each detector pixels can be modeled by a stationary random process $X(t)$, where t is time point of observation, and the outcome a binary number that states true if a photon arrived and false if not. Typically, this process is integrated over a certain time interval Δt, the exposure time interval of an acquired image. For X-ray holography, it is appropriate to consider only exposure intervals instead of single observations, leaving us with different random distributions $X_{\Delta t}$, which depend on the exposure time. We start with a very short illumination, also called a low-dose image. The photon noise then follows a Poisson distribution which is derived from the binominal distribution $f_{X_{\text{bin}}}$:

$$f_{X_{\text{bin}}}(k) = \binom{n}{k} p^k (1-p)^{n-k}, \; k \in \mathbb{N}_0, \tag{2.60}$$

with a know probability of a photon event $p \in [0,1]$, a known maximum number of photon events $n \in \mathbb{N}$ and with an expected value of $E\{X\} = np$. We get the Poisson distribution $f_{X_{\text{poiss}}}$ by removing the restrictions on the number of possible photons with $n \longrightarrow \infty$. We keep the expectation value unchanged, yielding:

$$f_{X_{\text{poiss}}}(k) = \frac{E\{X\}^k \cdot e^{-E\{X\}}}{k!},\ k \in \mathbb{N}_0. \tag{2.61}$$

Here, A is the expected photon count with respect to a certain exposure time Δt. For a sufficient large exposure time, the discrete nature of photons will be averaged out and we can change the model at the detector from discrete photons to continuous intensities. The Poisson distribution then approaches a Gaussian distribution $f_{X_{\text{gauss}}}$ and the discrete photon count parameter $k \in \mathbb{N}_0$ can be replaced by a continuous intensity parameter $x \in \mathbb{R}$ with

$$f_{X_{\text{gauss}}}(x) = \frac{1}{\sqrt{2\pi\sigma}} e^{-\frac{1}{2}\left(\frac{x-E\{X\}}{\sigma}\right)^2}, \tag{2.62}$$

where σ is the variance with $\sigma = E\{(X - E\{X\})^2\}$.

There are also other sources of noise in the measurement system with rather unknown distributions that add to the photon noise at the detector. This includes readout noise, which results from imprecise electronics, thermal noise and others. The specific random distributions of every noise sources are currently unknown. The central limit theorem could be in principle applied to assume in total a Gaussian distributed noise in the data. However, the optimal unstructured noise model is still an open research question and should be investigated in future works.

Unstructured noise is often handled by the reconstruction algorithm, for example by creating the target function of the optimization problem accordingly, which will be described in Sec. 3.2.1.

3 Baseline Algorithm and Test Data Framework

The main topic of this work is the reconstruction of refractive indices from data of a NFH microscopy setup at a synchrotron radiation light source. In contrast to many other imaging methods, especially in the field of medical imaging where a relatively well definable set of objects are measured, one has to expect that all kinds of objects are probed. The range of samples includes very weakly interacting objects such as biological samples, which only phase shift, to strongly interacting objects with significant absorption. The same holds for the shape of the samples, which have an infinite variety in infinite combinations, from smooth and round structures to very edged objects with high spatial gradients in the refractive index between the object and its surroundings.

The variety is even more increased by different possibilities for the realization of the setup through different choices of the instrumentation. Different optics can be employed to focus the X-ray beam. Each optic has different aberration characteristics and requires a specific setup geometry. The X-ray energy and exposure time can also vary, which affects the noise in the recorded data. The list of variations can be arbitrarily extended. The consequence is that a large variety of measurement setups and reconstruction algorithm to address scientific questions exists and a claim about what the state-of-the-art system is cannot be easily made.

While the investigation in this work was done with respect to certain issues in the reconstruction problem, which can be generalized, the reference of the developed improvements was nevertheless a very specific measurement setup in combination with a specific reconstruction algorithm. Under these conditions, experimental data was acquired, the simulation framework was designed and the basic algorithm implemented. In this chapter, the projected gradient descent (PGD)-based reference algorithm is derived, which is investigated and improved in the following chapters. For benchmarking, four different experimental data sets have been acquired, which are presented with their motivation. The experimental data is used in Ch. 4 and Ch. 5. For Ch. 5, additional simulation data is created to isolate certain features. The simulation data is also shown here.

3.1 Data Preprocessing

Before performing a reconstruction with the idealized forward model, most of the structured distortions in the data (Sec. 2.4.1) can be removed from the measured hologram in a preprocessing step by an empty beam correction, the so-called flat-field correction (FFC). [51–53]. We define the Fresnel propagation kernel $\mathcal{D}_{\mathrm{Fr}}(\psi)$ for wave-fields ψ with

$$\mathcal{D}_{\mathrm{Fr}}(\psi) = \mathcal{F}^{-1} \circ \exp\left(-\mathrm{i} \cdot \pi \frac{(k_x^2 + k_y^2)}{\mathrm{Fr}}\right) \circ \mathcal{F} \circ \psi. \tag{3.1}$$

The flat-field-correction assumes that the distortion of the hologram $\mathcal{I}_{\mathrm{det}}$ in the detector plane is given by a multiplication of the propagated perturbation function P and the original hologram $\mathcal{I}_{\mathrm{raw}}$ with

$$\mathcal{I}_{\mathrm{det}} = |\mathcal{D}_{\mathrm{Fr}}(\exp\left(\mathrm{i}\tilde{O}\right)\ P\ \psi_0)|^2 \approx \mathcal{I}_{\mathrm{flat}}\mathcal{I}_{\mathrm{raw}}, \tag{3.2}$$

$$\mathcal{I}_{\mathrm{flat}}\mathcal{I}_{\mathrm{raw}} = |\mathcal{D}_{\mathrm{Fr}}(P)|^2 \cdot |\mathcal{D}_{\mathrm{Fr}}(\exp\left(\mathrm{i}\tilde{O}\right)\psi_0)|^2. \tag{3.3}$$

To remove the structured distortions from the raw detector data, it can then be divided by the propagated perturbation function, which is called the flat-field or also empty beam image since it represents the illumination without an object in the detector plane. We get the corrected hologram $\mathcal{I}_{\mathrm{cor}}$ by

$$\mathcal{I}_{\mathrm{cor}} = \frac{\mathcal{I}_{\mathrm{det}}}{\mathcal{I}_{\mathrm{flat}}}. \tag{3.4}$$

An estimation of the flat-field is calculated by averaging multiple measurements without an object over a certain time period. A principle component analysis (PCA) can be performed, which creates orthogonal components, sorted by their statistical variance. A PCA is an orthogonal linear transformation which transforms the coordinate system of the data. Removing an arbitarely number of the last components from the PCA reduces the dimension of the measurement space to the modes that explain the beam-dynamics the most. For each raw hologram the illumination is then extracted by a projection onto those components. This removes the object, which is only explained by the removed components. The flat-field of a measured hologram is calculated by a projection $\mathcal{P}$ onto those components. Let Ω_C be the selected flat-field components of the PCA result. The flat-field $\mathcal{I}_{\mathrm{flat}}$ of a measured hologram $\mathcal{I}_{\mathrm{det}}$ is then given by

$$\mathcal{I}_{\mathrm{flat}} = \mathcal{P}_{\Omega_C}\mathcal{I}_{\mathrm{det}}, \tag{3.5}$$

and consequently the flat-field corrected hologram $\mathcal{I}_{\mathrm{cor}}$ by

$$\mathcal{I}_{\mathrm{cor}} = \frac{\mathcal{I}_{\mathrm{det}}}{\mathcal{P}_{\Omega_C}\mathcal{I}_{\mathrm{det}}}. \tag{3.6}$$

Figure 3.1 demonstrates the effect of the FFC. In (a) an example of $\mathcal{I}_{\mathrm{det}}$ is shown, without an object in the beam. The image is distorted mostly by structured distortions. Applying a FFC yields $\mathcal{I}_{\mathrm{cor}}$, shown in (b). Reducing the structured distortions also reduces the statistical dependence between pixel values and results in mostly uncorrelated pixels, which is important for the cost function for reconstruction, derived in the next section Sec. 3.2.1. The requirements for the validity of the FFC approach have been investigated in [51].

3.2 Reconstruction of Refractive Indices

A common approach to retrieve the projected refractive indices $\tilde{O}$ is to formulate the inverse problem as an optimization problem.

The goal here is to find a cost function which minimum yields the desired reconstruction result under a given set of measured data. This form of reconstruction problem is very typical in imaging systems and is intensively studied, so that a large variety of algorithms already exists if a canonical formulation of a cost function is found. In the following, the cost function for NFH is derived and formulated as a common least squares optimization problem. The reference algorithm of this work is presented that reconstructs the projected refractive indices by solving the presented optimization problem.

3.2.1 Cost function

A basic cost function can be derived from the maximum likelihood (ML) principle. It could be seen in Sec. 3.3, that the values of our measured holograms reach the order of $10^3 - 10^4$ count, which lies in the same order of the actual photon counts at the detector. Although a normal distribution would be a reasonable assumption, the reference algorithm here is based on a Poisson distribution noise model and was already shown to be feasible for the reconstruction of $\tilde{O}$ for strongly interacting objects.

We adapt the Poisson distribution function Eq. 2.61 such that it calculates the noise distribution for measurements in NFH under a Poisson noise model.

The observation k in the Poisson distribution Eq. 2.61 becomes the measured data set and the expectation value becomes the estimation from the forward model. The resulting function calculates the likelihood $p(\mathcal{I}_{\text{det}}^j|\tilde{O})$ that the measurements $\mathcal{I}_{\text{det}}$ for pixel indices j are observed under a given object $\tilde{O}$, i.e.:

$$p(\mathcal{I}_{\text{det}}^j|\tilde{O}) = \frac{E\{X\}^k \cdot e^{-E\{X\}}}{k!}, \tag{3.7}$$

$$E\{X\} = \left[\left|\mathcal{D}_{\text{Fr}}(\tilde{O})\right|^2\right]^j, \tag{3.8}$$

$$k = \mathcal{I}_{\text{det}}^j. \tag{3.9}$$

The reconstruction target is then the object $\tilde{O}$ that maximizes this likelihood function for all pixels. The computational complexity of calculating the maximizing $\tilde{O}$ can be reduced by maximizing the log likelihood function instead. Applying the natural logarithm removes the exponential function while preserving the position of the maximum.

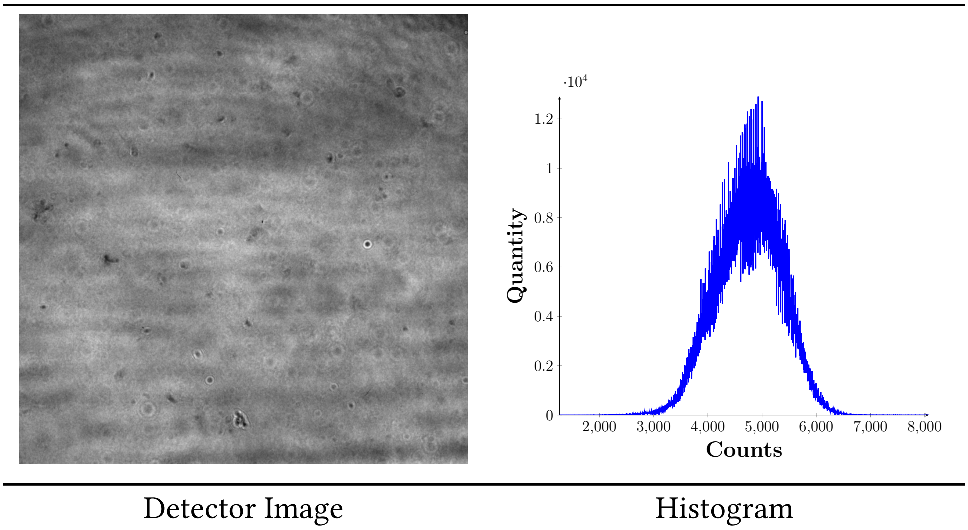

(a) Statistical analysis of an image without an object in the beam. The image is distorted mostly by structured distortions. Visible patterns are circles which result from the FZP, dust particles on exit windows of vacuum tubes or the detector and horizontal stripes, probably from the beam stop and/or the monochromator. For randomly distributed noise, the histogram on the right would, due to the central limit theorem, produce a Gaussian curve. However, the statistical dependence between neighbor pixels invalidates the central limit theorem and an otherwise recognizable superimposed Gaussian shows heavy fluctuations.

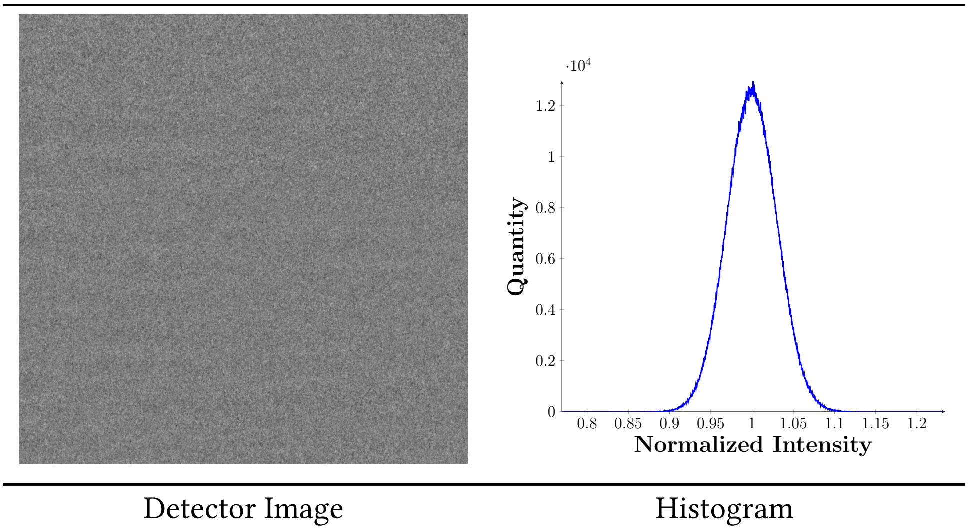

(b) Statistical analysis of the flat-field corrected image from (a), processed by the method of Sec. 3.1. The image is distorted mostly by randomly distributed, unstructured noise. Some patterns from the unprocessed image (a), like the horizontal stripes, are still imprinted. The histogram on the right side becomes approximately a Gaussian distribution, which shows the reduction of the statistical dependence between neighbor pixels.

Figure 3.1: Visualization of the flat-field correction. Empty raw hologram with (a) structured distortions and corrected hologram with mostly (b) unstructured noise.

The reconstruction target $\tilde{O}^*$ is then defined as the object $\tilde{O}$ that maximizes the log likelihood function for all pixel indices j, under the observation $\mathcal{I}_{\text{det}}$ with

$$\tilde{O}^* = \underset{\tilde{O}}{\text{argmax}} \sum_j \ln p(\mathcal{I}^j_{\text{det}}|\tilde{O}), \tag{3.10}$$

$$\ln p(\mathcal{I}^j_{\text{det}}|\tilde{O}) = \mathcal{I}^j_{\text{det}} \ln \left\{ \left[\left| \mathcal{D}_{\text{Fr}}(\tilde{O}) \right|^2 \right]^j \right\} - \left[\left| \mathcal{D}_{\text{Fr}}(\tilde{O}) \right|^2 \right]^j - \ln \left\{ \mathcal{I}^j_{\text{det}}! \right\}. \tag{3.11}$$

Since the last term does not change with a variation of $\tilde{O}$, we can ignore this term for the optimization problem. Additionally, in practice, the aim is often to find the minimum of the negative log likelihood to convert it to a minimization problem. The reconstruction problem then becomes

$$\tilde{O}^* = \underset{\tilde{O}}{\text{argmin}} \sum_j - \ln p(\mathcal{I}^j_{\text{det}}|\tilde{O}), \tag{3.12}$$

$$\tilde{O}^* = \underset{\tilde{O}}{\text{argmin}} \sum_j \left[\left| \mathcal{D}_{\text{Fr}}(\tilde{O}) \right|^2 \right]^j - \mathcal{I}^j_{\text{det}} \ln \left\{ \left[\left| \mathcal{D}_{\text{Fr}}(\tilde{O}) \right|^2 \right]^j \right\}. \tag{3.13}$$

For further reduction of the computational complexity, we remove the logarithm in the cost function by using the Taylor expansion of second order $\mathcal{T}_2$ around the point $\sqrt{\mathcal{I}_{\text{det}}}^j = \left| \mathcal{D}_{\text{Fr}}(\tilde{O}) \right|^j$ [54], yielding

$$f(x) = x^2 - \mathcal{I}^j_{\text{det}} \ln \left[x^2 \right] \tag{3.14}$$

$$\mathcal{T}_2 f(x; \sqrt{\mathcal{I}_{\text{det}}}^j) = \mathcal{I}^j_{\text{det}} - \mathcal{I}^j_{\text{det}} \ln \mathcal{I}^j_{\text{det}} + 2(x - \sqrt{\mathcal{I}_{\text{det}}}^j)^2. \tag{3.15}$$

The first two terms of this approximation are constant and can be ignored for the optimization problem. Also the constant factor can be removed. The remaining term on the right side, summed over all pixels and normalized, gives us the basic cost function in form of a least squares approach:

$$\tilde{O}^* = \underset{\tilde{O}}{\text{argmin}} \frac{1}{2} \left\| \left| \mathcal{D}_{\text{Fr}}(\tilde{O}) \right| - \sqrt{\mathcal{I}_{\text{det}}} \right\|_2^2, \tag{3.16}$$

which is approximately equivalent to solving the maximum likelihood problem of Eq. 3.10. The amplitude-based least squares approach can also be interpreted as a data fidelity problem where, the goal is to find the best representation of the measured data in the sense of the squared Euclidean distance. It is also possible to arrive at the same cost function then, instead of a Poisson distributed photon noise (shot noise), an additive Gaussian thermal noise is assumed [55]. For a Gaussian photon noise model, the result would be an intensity based instead of an amplitude based least squares approach [54].

This inverse problem is ill-posed, highly under-determined and does not have a unique solution [56, 57]. Additionally, there is a 2π ambiguity in the real part of $\tilde{O}$ when the exit wave Eq. 2.53 is calculated. Mathematically, the least squares approach tries to solve an optimization problem on a non-convex set with a non-linear forward model because of the magnitude operation. Physically, this manifests, among other things, in the twin-image problem [57].

We can reduce the number of possible solutions by introducing constraints on the reconstructed values. This can for example be done by restricting the reconstruction to physically valid values. In the X-ray regime, it is known that the interaction with electrons results in phase shifts that are only negative. Additionally, we can assume that the measured object does not contain an X-ray source itself such that the absorption is only positive. We model this non-negative electron density constrain by creating a set Ω_P as being the set of physically valid reconstruction values with

$$\Omega_P = \left\{\forall\, x \in \tilde{O} : \mathrm{Re}(x) \in (-\infty, 0],\ \mathrm{Im}(x) \in [0, \infty)\right\}. \tag{3.17}$$

Given a single exposure hologram $\mathcal{I}_{\mathrm{det}}$, the reconstruction problem for the refractive index in NFH can then be formulated using a regularized least-squares approach

$$\tilde{O}^* = \underset{\tilde{O}}{\operatorname{argmin}} \frac{1}{2} \left\| \left|\mathcal{D}_{\mathrm{Fr}}(\tilde{O})\right| - \sqrt{\mathcal{I}_{\mathrm{det}}} \right\|_2^2 + \mathcal{X}_{\Omega_P}(\tilde{O}). \tag{3.18}$$

The term $\mathcal{X}_{\Omega_P}$ is an indicator functions, defined by

$$\mathcal{X}_{\Omega_P}(\tilde{O}) = \begin{cases} 0 & \tilde{O} \in \Omega_P \\ +\infty & \text{else} \end{cases} \tag{3.19}$$

that models prior knowledge of the setup and the object. An alternative selection of the cost function is Eq. 3.16, formulated as a constrained problem:

$$\tilde{O}^* = \underset{\tilde{O} \in \Omega_P}{\operatorname{argmin}} \frac{1}{2} \left\| \left|\mathcal{D}_{\mathrm{Fr}}(\tilde{O})\right| - \sqrt{\mathcal{I}_{\mathrm{det}}} \right\|_2^2 \tag{3.20}$$

Both minimization problems can be solved by a PGD-based algorithm, which applies a forward-backward splitting approach to the problem. The PGD-based reference algorithm for this work is presented in the next section.

3.2.2 Projected Gradient Descent for phase retrieval

We begin with the construction of the basic solver that finds a solution for Eq. 3.18. A PGD approach solves this problem by splitting the cost function into two separate problems, (i) the data fidelity and (ii) the constraint. A global solution is then found by an alternation between both problems which are solved by (i) a weighted gradient descent towards the minimum of the data fidelity term and (ii) a projection onto the convex set $\Omega = \Omega_P$. A solution of the general minimization problem

$$\tilde{O}^* = \underset{\tilde{O}}{\operatorname{argmin}}\, f(\tilde{O}) + \mathcal{X}_{\Omega}(\tilde{O}), \tag{3.21}$$

is then calculated by a loop over the two basic operations. (i) A gradient descent step or Landwer-iteration and (ii) a projection onto the constraint set Ω_P, until a predefined stopping criterion, e.g. a maximum iteration number, is reached:

$$\begin{aligned}(i)\ \tilde{O}_{i+1} &= \tilde{O} - \alpha \nabla f(\tilde{O}_i),\\ (ii)\ \tilde{O}_{i+2} &= \mathcal{P}_{\Omega_P}(\tilde{O}_{i+1}).\end{aligned}$$

Here, α is the step size for the gradient descent and $\nabla f(\tilde{O})$ is the Wirtinger-derivatives-based gradient of the data fidelity term, given by [20, 58, 59] with

$$f(\tilde{O}) = \frac{1}{2}\| |\mathcal{D}_{Fr}(\tilde{O})| - \sqrt{\mathcal{I}_{\text{det}}} \|_2^2, \tag{3.22}$$

$$\nabla f(\tilde{O}) = -i \cdot \overline{\exp\left(\mathrm{i}\tilde{O}\right)} \cdot \mathcal{D}_{Fr}^{-1}\left(\mathcal{D}_{Fr}(\tilde{O}) - \sqrt{\mathcal{I}_{\text{det}}} \odot \operatorname{sgn}\left(\mathcal{D}_{Fr}(\tilde{O})\right)\right), \tag{3.23}$$

$$\operatorname{sgn}(x) = \begin{cases} 0 & \text{if } x = 0 \\ \frac{x}{|x|} & \text{else} \end{cases}. \tag{3.24}$$

For gradient descent methods, it is in general not recommended to use a standard gradient descent step for the optimization of a non-convex function f in form of $x_{i+1} = x_i - \alpha \nabla f(x_i)$ [60, 61]. This standard algorithm is known for having trouble with optimizing functions that contain local minima, flat surfaces or ravines. Instead, we make use of the Nesterov accelerated gradient (NAG) (NAG) [62, 63] with momentum γ and step size η. The modified gradient ∇g is given by:

$$\nabla g(\tilde{O}_i) = \gamma \nabla g(\tilde{O}_{i-1}) + \eta \nabla f(\tilde{O}_i - \gamma \nabla g(\tilde{O}_{i-1})). \tag{3.25}$$

with $\nabla g(\tilde{O}_0) = 0$ and $\nabla f(\tilde{O})$ is the non-accelerated gradient of the data fidelity term.

We get a projector $\mathcal{P}_{\Omega_P}$ of $\tilde{O}$ onto Ω_P by projecting the real and imaginary part separately and pointwise onto the defined intervals:

$$\mathcal{P}_{\Omega_P}(\tilde{O}) = \min\left(0, \operatorname{Re}(\tilde{O})\right) + i \cdot \max\left(0, \operatorname{Im}(\tilde{O})\right). \tag{3.26}$$

As a denoising method, a (iii) weak Gaussian filter is applied at the beginning of each iteration. This yields the complete PGD algorithm:

$$\begin{aligned}(iii)\ \tilde{O}_{i+1} &= \text{gauss\_filt}(\tilde{O}_i)\\ (i)\ \tilde{O}_{i+2} &= \tilde{O}_{i+1} - \nabla g(\tilde{O}_{i+1})\\ (ii)\ \tilde{O}_{i+3} &= \mathcal{P}_{\Omega_P}(\tilde{O}_{i+2})\end{aligned}$$

with a Nesterov momentum accelerated gradient $\nabla g(\tilde{O}_i)$ is shown in Alg. 0.

Algorithm 0: Basic reconstruction of $\tilde{O}$

```
Input: Pre processed measurements $\mathcal{I}_{\text{det}}$, update rate $\eta$ for the gradient step, Nesterov
       momentum $\gamma$, filter coefficients $\Omega_F$, initial guess $\tilde{O}_0$, maximum iterations $k_{\max}$
Output: Approximated solution $\tilde{O}^*$

$g_0 \leftarrow 0$
$k \leftarrow 0$
while $k < k_{\max}$ do
    $y_{k+1} \leftarrow \tilde{O}_k - \gamma g_k$
    $g_{k+1} \leftarrow \gamma g_k + \eta \nabla \left[ \frac{1}{2} \left\| |\mathcal{D}_{Fr}(y_{k+1})| - \sqrt{\mathcal{I}_{\text{det}}} \right\|_2^2 \right]$
    $\tilde{O}_{k+1} \leftarrow \mathcal{P}_{\Omega_P}(\tilde{O}_k - g_{k+1})$
    $k \leftarrow k + 1$
end
$\tilde{O}^* \leftarrow \tilde{O}_{k_{\max}}$
return $\tilde{O}^*$
```

3.3 Experimental data

The experimental data that was used in this work was acquired at the P05 nano-endstation at PETRA III at DESY, Hamburg, operated by Helmholtz-Zentrum Hereon. An NFH setup was used for nano-tomography. Relevant literature of the setup can be found in [8, 46, 64, 65] and a sketch of the setup is shown in Fig. 2.3 [46]. The distance between the focal spot of the FZP and the sample is in the order of 133 mm. The detector is placed downstream behind the sample at a distance in the order of 20 m.

With this setup, the detector is placed in the so-called near-field or Fresnel regime with respect to the measured sample size. The detector is a scintillator (10 µm Gadox) sCMOS camera (Hamamatsu C12849-101U) with 6.5 µm pixel size at 16 bit image depth and 2048 × 2048 pixels. The used FZP has two major disadvantages, which are important for the experiments but also one very important advantage for the reconstruction algorithm. First, the FZP has a low focusing efficiency and requires a setup with large distances for z_{01} and z_{12}. Furthermore, around 80 % of the incoming beam is blocked leaving only 20 % of beam intensity for the measurement. The consequence is a long exposure time per hologram which lies between 500 ms and 2 s for 2000 to 5000 counts at the detector. The type of counts, photon or electron counts, depends on the detector. The relevance of the count number is explained in Sec. 2.4. The advantage is that the FZP produces a wavefront which can be assumed to be sufficiently precise spherical wave-front such that an empty beam correction by the method described in Sec. 3.1 can be performed.

A large variation of different objects is measured on the beamline. Some object properties are particularly important for the reconstruction in NFH. One is the interaction

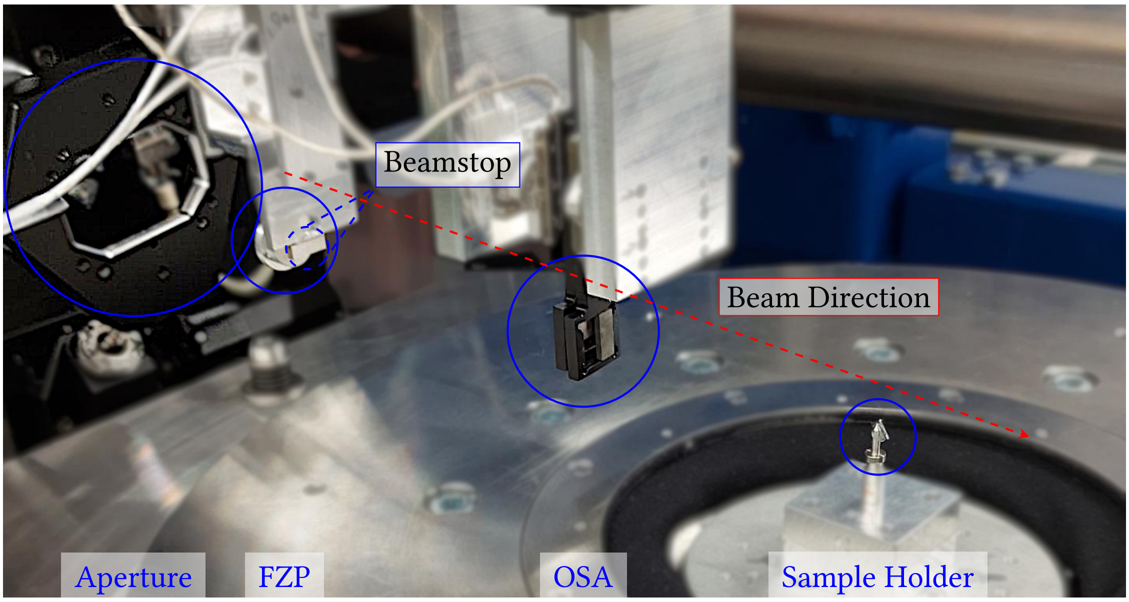

Figure 3.2: The image of the experimental setup was taken at the P05 endstation at PETRA III at DESY, Hamburg. The hardware components correspond the components at the same position like in the sketch of Fig. 2.3. The detector is positioned 20 m downstream from the image above.

strength between the sample and the illumination. The variation ranges from weakly interacting objects with a phase shift below the phase-wrapping limit of 2π rad, to moderately strong interaction with phase shifts above 2π rad and weak absorption, to strongly interacting objects with phase of multiple factors of 2π rad and strong absorption. Another important object property are the spacial frequencies in the refractive indices of the object which are differently biased in the reconstruction. Strong jumps, e.g. at the object/vacuum interface have a different reconstruction behavior than weak curvatures and smooth surfaces.

For Ch. 4, the experimental test objects are selected with a focus on the interaction strength of the object. The samples used in this work have a diameter between 8 µm and 150 µm. The energy of the illumination was chosen to be in the hard X-ray regime between 11 keV and 17 keV. The measured data in Fig. 3.3a covers weakly interacting samples which do not exceed phase shifts of π rad to multi material samples that produce a phase range beyond 6π rad. The samples are shortly introduced now:

A spider hair [66–68], which can be assumed to be a purely phase-shifting object with values less than π rad. A cactus needle and a piece of a human tooth, prepared by focused ion beam milling. Both with phase shift values in the proximity of 2π rad. A biodegradable magnesium-based wire implant that is partially corroded and induces phase shifts with values beyond 6π rad [23, 69, 70].

Further object specific properties are the following:
The spider hair possesses many fine structures fading into the background. The flat-

Sample	Energy	r_n	w_n	z_{01}	z_{02}	t
Spider hair	11.0 keV	150 µm	50 nm	79.95 mm	19.661 m	1.0 s
Cactus Needle	17.0 keV	150 µm	50 nm	28.54 mm	19.652 m	0.8 s
Tooth	17.0 keV	150 µm	50 nm	81.708 mm	19.652 m	0.8 s
Magnesium-based wire	11.0 keV	150 µm	50 nm	43.70 mm	19.661 m	1.5 s

Table 3.1: Parameters according to Sec. 2.2, for the setup shown in Fig. 2.3. The illumination energy, the radius of the FZP r_n, the width of its outer most structure w_n, the cone beam geometry z_{01}, z_{01} and the sample exposure time t.

field-correction in the cactus needle and tooth samples left an area in the upper part of the hologram which has a lot of noise. The tooth sample contains dense structures on top and at the bottom, as well as a strongly interacting particle in the upper right corner, which are residuals from the sample preparation. In the magnesium-based wire sample, the flat-field-correction left a vertical gradient in the hologram background.

Most of the parameters for the Fresnel number of the forward model of Sec. 2.3 are known very precisely, either by vendor specification or by measurements of the setup itself. Sometimes, however, individual parameters can only be roughly estimated or the overall accuracy of the Fresnel number is not sufficient for a reconstruction. In the example of the P05 endstation, this is the case for the focus-to-sample distance z_{01}, which can only be determined up to a precision of ±5 mm, during the experiment.

3.4 Simulation Data

An additional selection of simulated phantoms was used in Ch. 5 to test different focus criteria. The phantoms in Fig. 3.3b were created to isolate the properties of certain shapes. The first phantom, a cell, simulates the measurement of a biological object. The focus is on the presence of many small details without extreme edges or too large smooth surfaces. The second phantom, a simple triangle, tests two edge cases: The triangle has strong edges at the boundary between the object and object-free space, oriented in three different directions: One in each orthogonal direction and one in a diagonal direction. Furthermore, the triangle has a smooth surface in the center, i.e. a surface that interacts with the illumination without spatial gradients. The next object, the projection of a sphere, targets the typical weakness of reconstruction algorithms to have problems with weakly curved surfaces. The spatial gradient to the center of the sphere is continuously decreasing while the absolute phase shift value is increasing.

The simulation of a measured hologram with respect to a reference object basically results from the forward model of the setup in Fig. 2.3. To create the hologram, the parameters of the cone beam setup have to be defined and the model then converted to an equivalent parallel beam setup. The parameters to set for the Fresnel number Fr of the cone beam model are as follows: (i) the illumination wavelength λ, (ii) the detector pixel size Δx, (iii) the focus-to-object distance z_{01}, (iv) the object-to-detector distance

z_{12}. The test objects for simulations in this work are defined as discrete phantoms on a Cartesian grid. They are derived from two-dimensional images whose gray values are normalized to the closed interval $[0, 1]$. With discrete pixel indices, the phantom can be expressed as a function f:

$$f : \mathbb{N}_0^2 \mapsto G, \tag{3.27}$$

$$G := \{g \in \mathbb{R} \mid 0 \leq g \leq 1\}, \tag{3.28}$$

which maps the pixel indices $x, y \in \mathbb{N}_0$ to a gray value. The phantoms are simulated as single material phantoms with a fixed δ/β ratio for a given wavenumber k. A maximum thickness $d_{\max}$ is specified for each of the phantoms and the projection approximation of Eq. 2.35 is applied to obtain the projected complex refractive index, which is calculated for each pixel with the thickness function d:

$$d(x, y) = d_{\max} \cdot f(x, y). \tag{3.29}$$

The pixel number of the phantom must match the setup geometry, which means that a sufficient sampling rate of the Fresnel propagation operator in frequency space must be ensured. This is at least $1/\mathrm{Fr}$ pixel per spatial dimension orthogonal to the propagation direction [71]. If required, the phantom has to be padded by a constant zero until the required pixel number is reached. This number can be much larger than the simulated pixel number of the detector. To create the hologram, a source illumination ψ_0 has to be defined and the result of the forward model Eq. 2.55 be calculated. The resulting hologram is usually larger than the field of view (FOV) of the detector. To match the detector size, the hologram has then to be cropped centrally to the number of pixels of the detector.

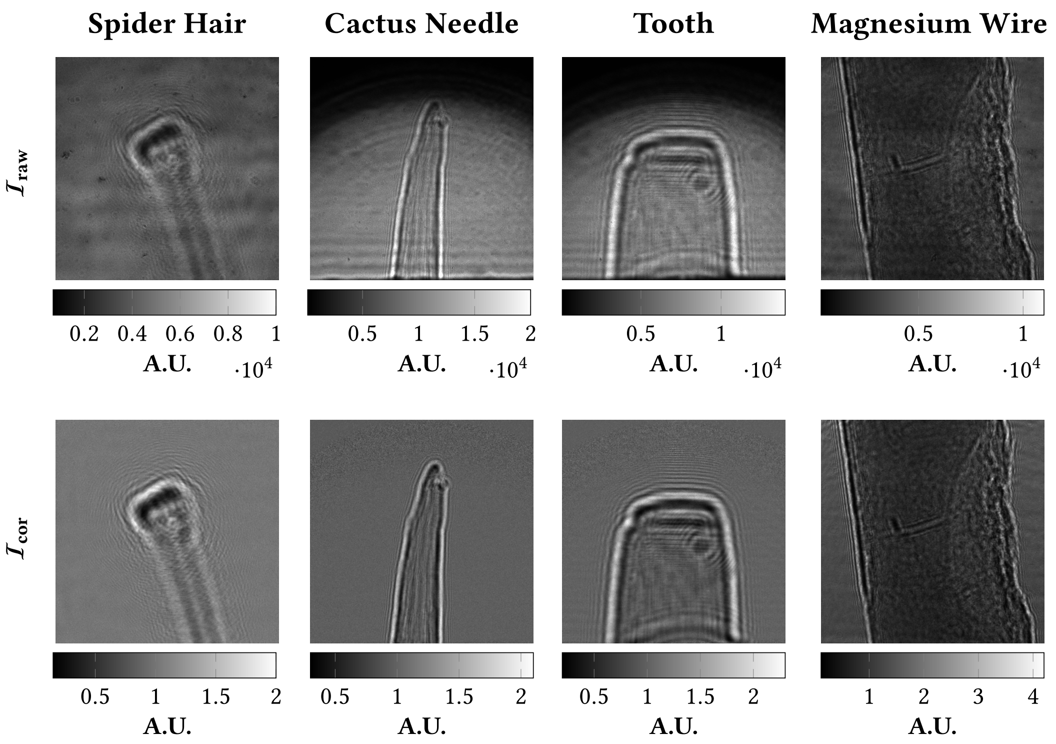

(a) Experimental data, showing the raw detector data (top) and the flat-field corrected holograms (bottom). The objects were chosen due to their increasing interaction strength with X rays. The data covers weakly interacting samples which do not exceed phase shifts of π rad to multi material samples that produce a phase range beyond 6π rad.

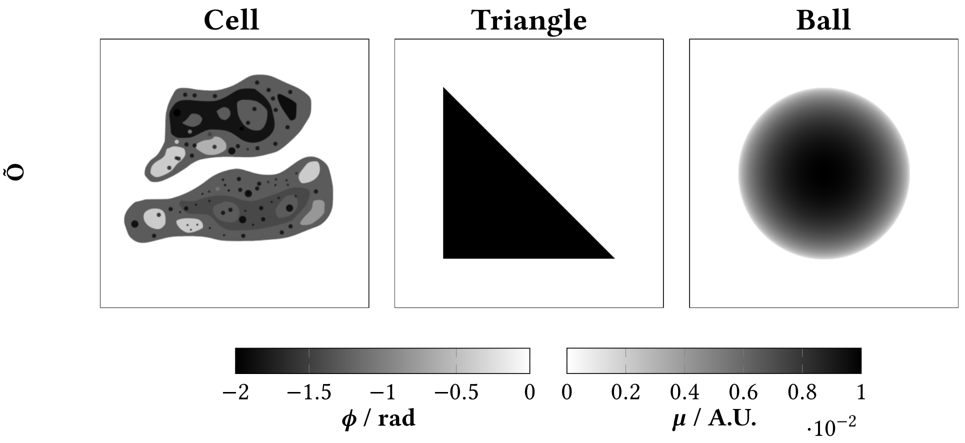

(b) Simulated objects. The simulated objects are mixed objects, phase shiting (ϕ) and absorbing (μ) according to the color bars. The following shapes were created: A biological cell with lot of small and sharp features. A triangle with strong edges in combination with a smooth surface. A ball object which contains a large range of small image gradients.

Figure 3.3: Experimental data (a) and simulated objects (b) that have ben used as test objects in Chapters 4 and 5 of this work.

Analysis and Suppression of Reconstruction Artifacts

4

This chapter is based on the publication [21] and contains further background and details regarding the compensated reconstruction artifacts.

The goal of a reconstruction in NFH is to compute the complex refractive indices of a measured object from a recorded hologram. Further information about the reconstruction target can be found in Sec. 2.1.3. In Sec.3.2, the reconstruction problem was derived in its mathematical form and was described as ill-posed and highly under-determined without a unique solution.

In practice, the available approaches that compensate for the missing information can be split into experimental and algorithmic approaches. They reach from adaptions of the experiment to the incorporation of prior knowledge into the reconstruction algorithm, for example in form of additional object constraints or regularization schemes.

Naturally, some approaches alleviate the under-determination by performing more than one measurements per reconstructed ROI. For each measurement, the experimental setup is then slightly changed to add more variation to the data. This includes for example the scanning with overlaps like ptychography [27–29] or also the full-field measurement setup, of this work but with measurements in multiple distances [14, 30, 31, 72, 73].

An additional object constraint which can be applied is the positive density constraint and was already presented in Sec. 3.2.1. The combination of this prior together with a spatial support constraint can be found in various algorithms [20, 32, 33, 72]. A different kind of physics related constraint can be derived from the known relationship between phase shift and absorption values, also called the δ/β coupling [43, 44, 74]. This coupling is in general linear and the proportional quantity material dependent. It can be used as a prior in the reconstruction algorithm for example by explicit material constraints [72] or by coupling with joint sparsity regularization [75].

Regularization techniques add more implicit priors about the object and can be applied in arbitrary mathematical domains. Here, enforcing sparsity in wavelet, shearlet or in the gradient domain with a Lasso regularization is a common choice [76–81], as well as Tikhonov regularization which favors smoothness and smaller values [72, 75, 77, 82, 83].

Unfortunately, each of these approaches comes with certain trade-offs: Measuring more data is not always possible or not always desired, be it because of limits in the available measurement time or restrictions on the measurement setup. This is especially true in the case of single-pulse imaging at X-ray free-electron lasers or *in situ/operando* studies

[22–25, 53]. Employing a spatial support constraint is not always possible and can be computationally very expensive to determine. Objects which are larger than the ROI for example do not posses a compact support. Furthermore, the support has to be defined. A manual approach requires advanced knowledge about the reconstruction result beforehand while an automatic adaption during the reconstruction adds further computational complexity [34, 53]. The required hyper-parameters can grow arbitarely. This renders a spatial support constraint impractical, especially for time sensitive *in situ* and *operando* measurements. The problem with domain specific regularization is that they always introduce a bias into the reconstruction. The strength of the bias depends on the regularized domain and the regularization weights. Is the bias too strong, artifacts, blur or other effects can alter the reconstruction result.

This chapter performs an extended analysis of the artifacts that occur for reconstructions with the PGD-based reconstruction algorithm of Sec. 3.2.2, if the mentioned restrictions are abandoned. This includes measurements in multiple distances, employing a spatial support constraint, constraints based on the δ/β relationship and computationally intensive regularization such as total variation. The artifacts are divided into categories. Each of the categories is dedicated to one section in this chapter, where the cause is investigated and at least one counter-strategy is developed. In the last section, different combination of the proposed methods are applied to the experimental data from Sec. 3.4. The results are compared to each other with respect to remaining artifacts and computational time.

4.1 Truncation of the hologram

The wave field after interaction with object is propagated to the detector, where the interference pattern is recorded as a hologram. However, due to a limited FOV of the detector, it is not able to record the complete arriving wavefront such that the hologram in the detector plane is truncated. In the following, we will derive a mathematical expression for the truncation and use $\overline{\mathcal{I}}_{\text{det}}$ for the hologram intensities at the detector plane and $\mathcal{I}_{\text{det}}$ the captured hologram by the detector, which is truncated.

The hologram, captured by the detector, is an image of a rectangular area inside of the wavefront in the detector plane. Outside of the detector area, no signal is recorded. The truncation with respect to a non-truncated hologram can be described by defining all values outside of the detector area to be zero. We define the truncation operation $\text{trunc}(\overline{\mathcal{I}}_{\text{det}})$ of an non-truncated hologram $\overline{\mathcal{I}}_{\text{det}}$ by a multiplication with a two dimensional function $\text{trc}(x,y)$, yielding the truncated measurements $\mathcal{I}_{\text{det}}(x,y)$ with:

$$\mathcal{I}_{\text{det}}(x,y) = \text{trunc}(\overline{\mathcal{I}}_{\text{det}}(x,y)) = \text{trc}(x,y) \cdot \overline{\mathcal{I}}_{\text{det}}(x,y). \tag{4.1}$$

If all values outside of the detector area should be zero, the truncation operator is a two dimensional rectangular function $\mathrm{trc}_0(x, y)$:

$$\mathrm{trc}_0(x, y) = \begin{cases} 0, & \text{if } |x| > \frac{w_x}{2} \text{ or } \quad |y| > \frac{w_y}{2} \\ \frac{1}{2}, & \text{if } |x| = \frac{w_x}{2} \text{ and } |y| = \frac{w_y}{2} \\ 1, & \text{if } |x| < \frac{w_x}{2} \text{ and } |y| < \frac{w_y}{2} \end{cases}, \tag{4.2}$$

where (w_x, w_y) are the detector dimensions in each spatial direction and (x, y) the spatial coordinates. The spatial coordinates $(0, 0)$ are aligned to the center of the detector. Using zeros as truncation values in the context of the PGD algorithm of Sec. 3.2.2 is problematic, since it results in singularities in the gradient of Eq. 3.23. In practice, the truncated hologram is often padded by a constant value different from zero. After the flat-field-correction of Sec. 3.1, this value is typically one, since the flat-field-correction aims to normalize the empty beam intensities. This is then equivalent to an object free area of the beam. To account for that, the rectangular function can be modified to a function $\mathrm{trc}_1(x, y)$ by replacing the zero with a normalization factor $1/\overline{\mathcal{I}}_{\mathrm{det}}$, which is the inverse of the non-truncated hologram.

$$\mathrm{trc}_1(x, y) = \begin{cases} \frac{1}{\overline{\mathcal{I}}_{\mathrm{det}}(x,y)}, & \text{if } |x| > \frac{w_x}{2} \text{ or } \quad |y| > \frac{w_y}{2} \\ \frac{1}{2}(1 + \frac{1}{\overline{\mathcal{I}}_{\mathrm{det}}(x,y)}), & \text{if } |x| = \frac{w_x}{2} \text{ and } |y| = \frac{w_y}{2} \\ 1, & \text{if } |x| < \frac{w_x}{2} \text{ and } |y| < \frac{w_y}{2} \end{cases}, \tag{4.3}$$

The truncation of the hologram causes data inconsistencies and yields to reconstruction artifacts, which are especially present at the border of the truncation area. In the next section, we investigate the artifacts that appear when the truncation operators $\mathrm{trc}_0(x, y)$ and $\mathrm{trc}_1(x, y)$ are used and analyze the source of those artifacts.

4.1.1 Truncation artifacts

There are multiple sources of inconsistencies at the detector edge. First, the scattering angles and the propagation distance to the detector can be so large that not all information can be captured by the FOV of the detector. This effect can for example be seen in the Fresnel region hologram of Fig. 2.4 at the upper and bottom right hologram borders, where the fringes are truncated. Nevertheless, the truncated area contains important information about the scattering object, which are then unavailable. Second, objects outside of the FOV can scatter into the FOV of the detector towards high propagation distances. The resulting fringes then belong to areas that are not necessarily considered during reconstruction and also lead to inconsistencies. However, the biggest issue with respect to the forward model is the introduction of a strong edges after truncation. The caused artifacts result from a combination of two effects: (i) spectral leakage and (ii) the amplification of high frequency (HF) errors, caused by the forward model. The spectral leakage results from the usage of the Fourier transform in the forward model and can manifest in so-called Gibbs artifacts [84–86]. The multiplication of $\overline{\mathcal{I}}_{\mathrm{det}}$ with the rectangular function in the spatial domain is equal to a convolution of the spectrum of $\overline{\mathcal{I}}_{\text{det}}$ with a sinc function. The sinc function is a sine function with an increasing damping factor towards infinity. the one-dimensional sinc function is defined as

$$\operatorname{sinc}(x) = \frac{\sin(\pi x)}{\pi x}. \tag{4.4}$$

The truncation operator in the Fourier domain is hence given as a convolution of the Fourier transform of $\overline{\mathcal{I}}_{\text{det}}$ with the Fourier transformed truncation operation $\operatorname{trc}(x, y)$. Using $\operatorname{trc}_0(\overline{\mathcal{I}}_{\text{det}})$ of Eq. 4.2 for truncation, the Fourier transform $\mathcal{F}$ of the truncation operator is the convolution of two one-dimensional sinc functions, one for each spatial direction:

$$\mathcal{F} \circ \operatorname{trunc}(\overline{\mathcal{I}}_{\text{det}}(x, y)) = w_x \operatorname{sinc}(w_x k_x) \circledast w_y \operatorname{sinc}(w_y k_y) \circledast \left[\mathcal{F} \circ \overline{\mathcal{I}}_{\text{det}}(x, y)\right], \tag{4.5}$$

where (k_x, k_y) are the coordinates in the Fourier domain.

The truncation operation hence heavily distorts the frequency spectrum of the hologram. The introduced error is amplified by the Fresnel free space propagator, which is particularly sensitive to high spatial frequencies (Sec.4.4). The free space propagator is required to perform operations in the detector and the object plane. The error which is introduced in the object plane is shown in Fig 4.1 with a simple example in a one-dimensional space:

We define the non-truncated hologram $\overline{\mathcal{I}}_{\text{det}}$ (Fig. 4.1a) as a constant intensiy and the wave-field $\overline{\psi}_{\text{det}}$ in the detector plane with zero phases and the square root of the hologram as the amplitudes:

$$\overline{\mathcal{I}}_{\text{det}}(x) = 1.2, \tag{4.6}$$

$$\overline{\psi}_{\text{det}}(x) = \sqrt{\overline{\mathcal{I}}_{\text{det}}(y)} \exp\left(\mathrm{i}0\right). \tag{4.7}$$

We then propagate this wave-field to the object plane, yielding the exit wave-field $\overline{\psi}_{\text{exit}}$:

$$\overline{\psi}_{\text{exit}}(x) = \mathcal{D}_{Fr}^{-1}(\overline{\psi}_{\text{det}}(x)). \tag{4.8}$$

The resulting intensity $|\overline{\psi}_{\text{exit}}|^2$ is shown in Fig. 4.1b. We now apply both truncation operators, $\operatorname{trc}_0(\overline{\mathcal{I}}_{\text{det}})$ and $\operatorname{trc}_1(\overline{\mathcal{I}}_{\text{det}})$ to the hologram. The truncation results $\mathcal{I}_{\text{det}}$ are shown in Fig. 4.1c and Fig. 4.1d. We again define the wave-field in the detector plane by Eq. 4.7, but this time with the truncated holograms $\mathcal{I}_{\text{det}}$. The results are propagated back to the object plane and the intensities are shown in Fig. 4.1e and Fig. 4.1f.

The FOV of the detector corresponds to a certain area in the reconstruction result, that is called ROI in this thesis. The observable effects in the ROI can be described as the following:

The intensities of $\overline{\psi}_{\text{exit}}$, i.e. the back-propagated and non-truncated wave-field $\overline{\psi}_{\text{det}}$ are also just a constant and the image in the ROI is distortion free. Both truncation operation causes a value jump, i.e. a sharp edge at the FOV border. The resulting effects on the

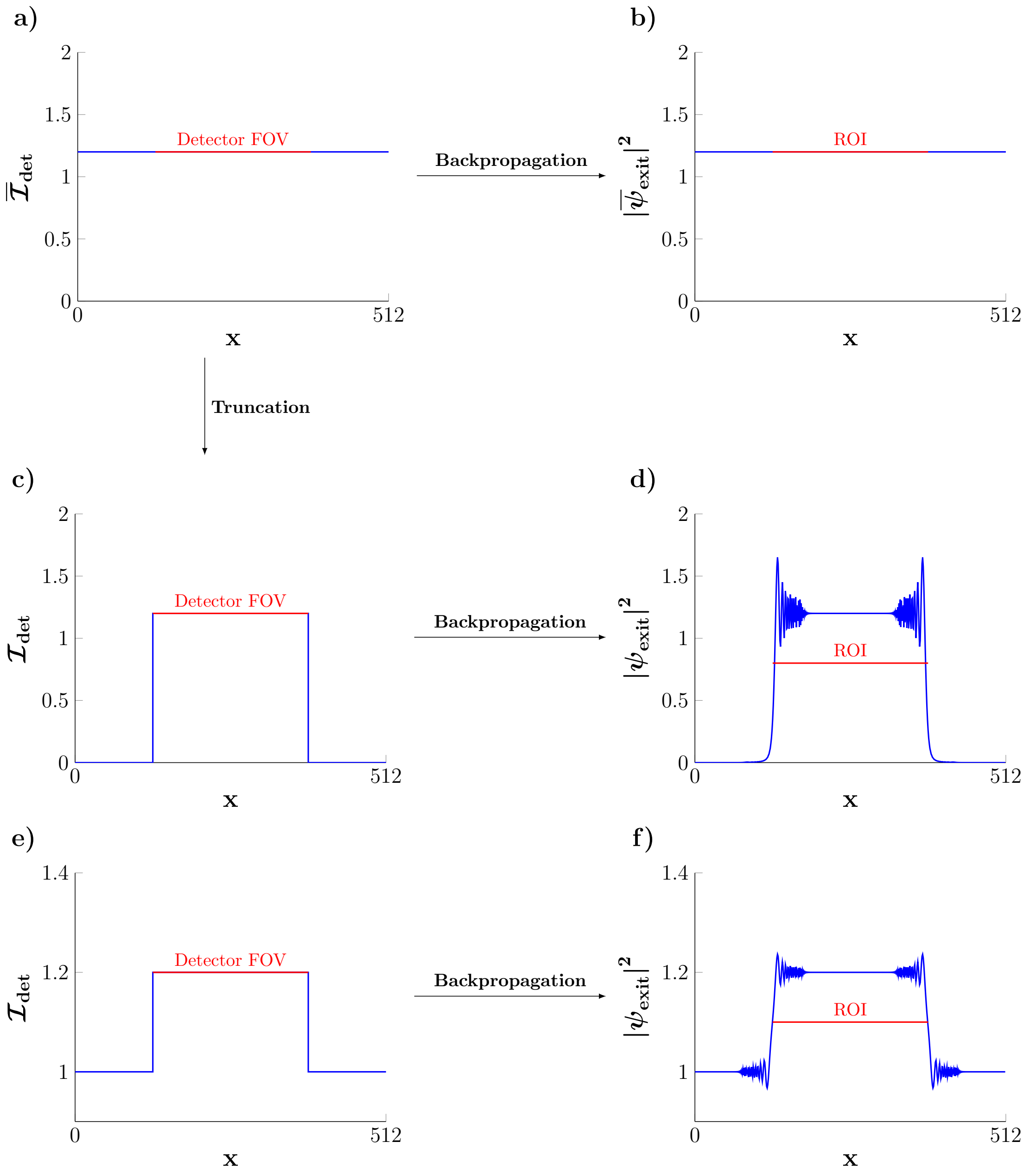

Figure 4.1: Demonstration of how truncation of the signal in the detector plane affects the signal in the object plane. (a) The non-truncated hologram $\overline{\mathcal{I}}_{\text{det}}(x)$ is a constant. The coverage of the detector is the detector FOV, marked in red. (b) The back-propagated hologram yields also a constant. (c) Because of the limited FOV of the detector, the hologram is truncated. (d) The intensities of the back-propagated and truncated hologram by function $\text{trc}_0(x)$ (Eq. 4.2) contains truncation (TR) artifacts inside of the ROI in the object plane. They are a mixture of spectral leakage and propagation fringes of the introduced edges. (e,f) The same problems appears if a hologram is paddded by a constant of one, which can be represented by a second truncation function $\text{trc}_1(x)$ (Eq. 4.3).

object plane are similar. The edges in the truncated holograms $\mathcal{I}_{\text{det}}$ are interpreted as real structure and back-propagated to the object plane. The distortions in the ROI follow a sine like function and the width of the distorted area increases with the propagation distance.
These type of structures also appear in the two dimensional case. The image in the object plane is retrieved by reconstructing the refractive indices of the measured object (Sec. 3.2.2). The same artifact structures are also present if a reconstruction is performed with a truncated hologram, which is shown in the reconstruction results in Fig. 4.2. The appearing distortions are slightly different for each object but follow all a sine like function. Most common artifacts are ring like or stripe artifacts, caused by the propagation of object corners and edges. Without proper preprocessing of the hologram, the introduced data inconsistencies by the truncation operation leads therefore to TR artifacts that can affect the whole ROI in the reconstruction. In the next sections, we will derive a new preprocessing approach to solve the truncation problem. The new preprocessing is summarized in Alg. 1. Also, the reference PGD-based algorithm Alg. 0 will be extended, which is shown in Alg. 2.

4.1.2 Compensation with padding

To develop a reasonable extension of the required hologram, we first investigate how an extension of the hologram in the detector plane changes the image in the object plane. In the beginning of this section, we have described the truncation operation in Eq. 4.1 for the truncated hologram $\mathcal{I}_{\text{det}}(x, y)$ as a multiplication between $\overline{\mathcal{I}}_{\text{det}}(x, y)$ and $\text{trc}(x, y)$. We can model the padding of the truncated hologram also by a multiplication with a padding function $\text{pad}\,(x, y)$, such that

$$\mathcal{I}_{\text{det}}(x, y)\ \text{pad}\,(x, y) = \text{trc}(x, y)\ |\mathcal{D}_{\text{Fr}}(\overline{\psi}_{\text{exit}}(x, y))|^2\ \text{pad}\,(x, y)\,. \tag{4.9}$$

In the ideal case, the padding operation is the inverse of the truncation operation and the original hologram $\overline{\mathcal{I}}_{\text{det}}$ can be retrieved by

$$\text{pad}\,(x, y) = \text{trc}^{-1}(x, y), \tag{4.10}$$

$$\text{s.t.}\ \ \mathcal{I}_{\text{det}}(x, y)\ \text{pad}\,(x, y) = \overline{\mathcal{I}}_{\text{det}}(x, y). \tag{4.11}$$

In the following, we try to find an approximate description of the padding operation in the object plane. We have seen a similar structure of Eq. 4.9 already in the data preprocessing of the base line algorithm Sec. 3.1 in Eq. 3.3. There, the effect of an illumination disturbance in the object plane on a hologram can then be calculated approximately as a multiplication between the non-disturbed hologram and the function of distortion. We use here the same theory and assume that the padding function pad is a propagated function of distortion P from the object plane to the detector plane. We define the truncation function as

$$\text{pad}\,(x, y) = |\mathcal{D}_{\text{Fr}}(P(x, y))|^2. \tag{4.12}$$

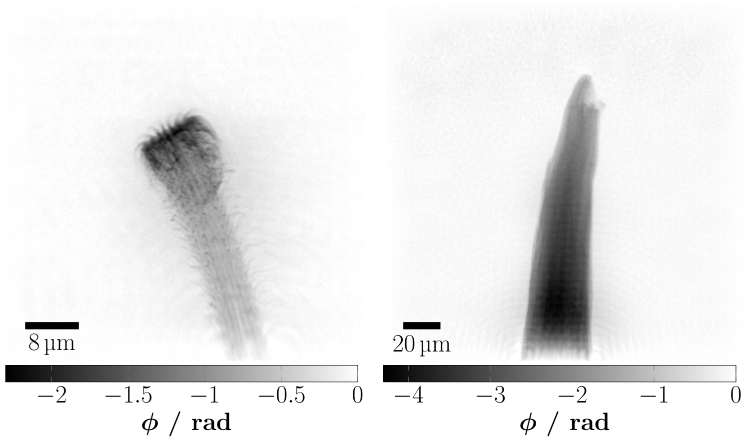

(a) Spider attachment hair

(b) Cactus needle

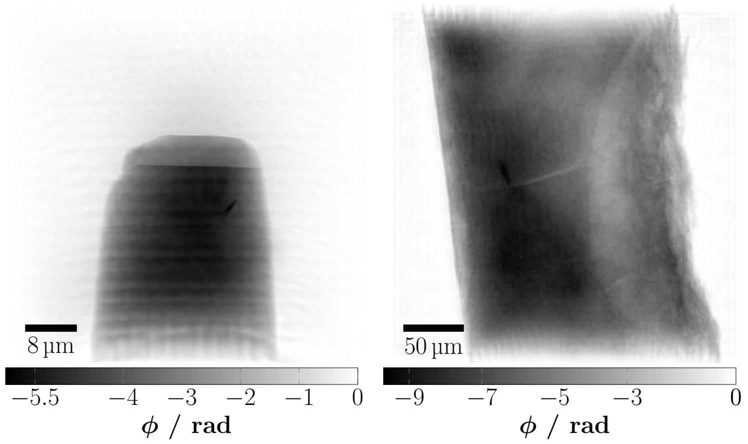

(c) Tooth

(d) Magnesium-based wire

Figure 4.2: TR artifacts appearing in reconstructed phase images. To illustrate the importance of solving the truncation problem of recorded holograms, the objects were already reconstructed by the improved algorithm of Sec. 4.5, without truncation correction. The results are heavily distorted by TR artifacts, which are caused by a combination of spectral leakage and the free space propagation of edge structures at the truncation border. Most common artifacts are ring like artifacts caused by the propagation of object corners and lattice like stripes caused by propagated object edges and inconsistent hologram padding. The truncation problem also resulted in a weakly reconstructed magnesium-based wire, where we would expect phase shift values of at least the double magnitude.

We make use of the flat-field approximation of Sec. 3.1 and write down the padding of the hologram $\mathcal{I}_{\text{det}}$ with respect to the object plane as

$$\mathcal{I}_{\text{det}} = |\mathcal{D}_{\text{Fr}}(P)|^2\, |\mathcal{D}_{\text{Fr}}(\psi_{\text{exit}})|^2 \approx |\mathcal{D}_{\text{Fr}}(P\,\psi_{\text{exit}})|^2. \tag{4.13}$$

Since the padding function for the hologram is always real-valued, a possible solution of the function P in the object plane is then given by the back-propagation of the padding function with zero phase from the detector plane to the object plane with

$$P = \mathcal{D}_{Fr}^{-1}(\sqrt{\text{pad}}\,\exp{(\mathrm{i}0)}). \tag{4.14}$$

We can use the same approximation for the truncation function, which is also always real-valued and define the truncation operation T in the object plane as

$$T = \mathcal{D}_{Fr}^{-1}(\sqrt{\text{trc}}\,\exp{(\mathrm{i}0)}). \tag{4.15}$$

The truncation and padding are then described in the object-plane as the following. The original exit-wave $\overline{\psi}_{\text{exit}}$ is modified by both operations, yielding a wave-field ψ_{exit} which is defined as

$$\psi_{\text{exit}} = P\;T\;\overline{\psi}_{\text{det}}. \tag{4.16}$$

It is evident that in this model, the padding P corrects the truncation operation T, if

$$P = T^{-1}, \tag{4.17}$$

$$\text{s.t.}\;\; \overline{\psi}_{\text{exit}} = P\;\psi_{\text{exit}}. \tag{4.18}$$

An example of the one-dimensional case is demonstrated in Fig. 4.3. The hologram $\overline{\mathcal{I}}_{\text{det}}$ (a) is truncated by the function trc_1 of Eq. 4.3, yielding the truncated hologram $\mathcal{I}_{\text{det}}$ in (c). As it was already seen in Fig. 4.1 of Sec. 4.1.1, the respective exit-wave ψ_{exit} in the object plane in (d) is distorted by TR artifacts around the truncation edges. The truncation function trc_1 is shown in (e), which we propagate to the object plane and retrieve so T, shown in (f). Multiplying the TR artifact distorted exit wave-field ψ_{exit} in (d), by the inverse of the back-propagated truncation function T^{-1}, recovers again the exit wave intensities $\overline{\psi}_{\text{exit}}$, shown in (b).
Unfortunately, the true function trc_1 of Eq. 4.3 is unknown, since it depends on the non-truncated hologram $\overline{\mathcal{I}}_{\text{det}}$. We can, however, use an approximation $\text{trc}_a(x, y)$ and replace the function $\overline{\mathcal{I}}_{\text{det}}(x, y)$ in Eq. 4.3 by a constant a_0 and get

$$\text{trc}_a(x,y) = \begin{cases} \frac{1}{a_0}, & \text{if } |x| > \frac{w_x}{2} \text{ or } \;\; |y| > \frac{w_y}{2} \\ \frac{1}{2}, & \text{if } |x| = \frac{w_x}{2} \text{ and } |y| = \frac{w_y}{2} \\ 1, & \text{if } |x| < \frac{w_x}{2} \text{ and } |y| < \frac{w_y}{2} \end{cases}. \tag{4.19}$$

We set pad = trc_a^{-1}, calculate P accordingly and repeat the steps of Fig. 4.3. The result is shown in Fig. 4.4 and the truncation corrected exit-wave-field intensities in panel (b).

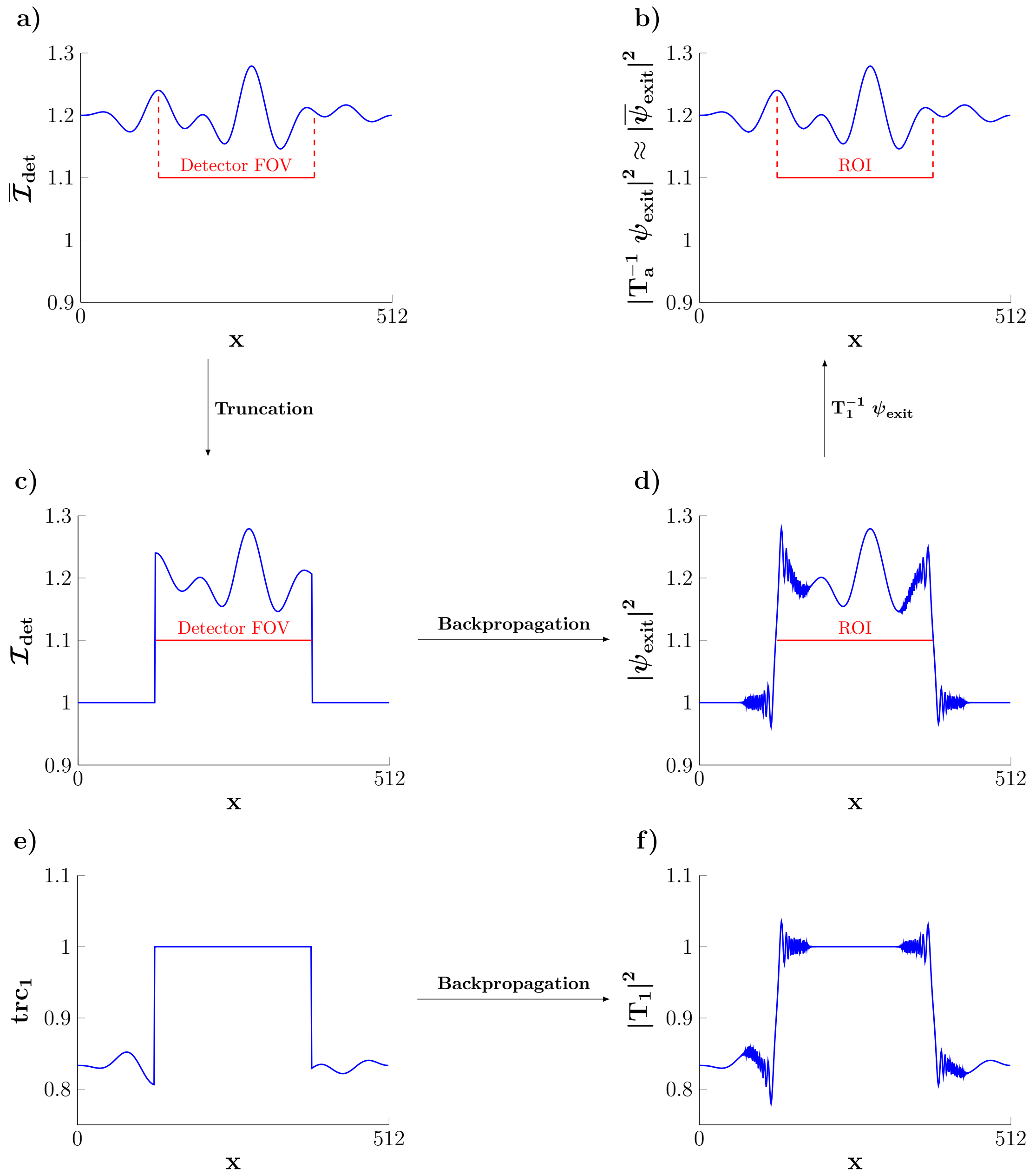

Figure 4.3: Demonstration of the truncation correction in the object plane by a back-propagated truncation-function. (a) Non-truncated hologram $\overline{\mathcal{I}}_{\mathrm{det}}(x)$ in the detector plane. (b) Intensities of non-truncated exit wave-field $\overline{\psi}_{\mathrm{exit}}(x)$. (c) Truncated hologram by function $\mathrm{trc}_1(x)$ (Eq. 4.3). (d) Intensities of $\psi_{\mathrm{exit}}(x)$, the back-propagated and truncated hologram, distorted by TR artifacts. (e) Truncation function $\mathrm{trc}_1(x)$. (f) Intensities of T_1, the back-propagated truncation function. Multiplying the TR artifact distorted exit wave-field ψ_{exit} in (d), by the inverse of the back-propagated truncation function T^{-1}, recovers again the exit wave intensities $\overline{\psi}_{\mathrm{exit}}$, shown in (b).

At the right truncation edge, the TR artifacts inside of the ROI are well corrected. The small difference between the border value and a yields a good suppression. At the left truncation edge, the artifacts are suppressed, but this side still suffers from artifacts, due to the large remaining offset. In general, the better a_0 matches the border value of the truncated hologram, the better the TR artifacts can be suppressed.
The correction of artifacts with this approach is limited to the accuracy of the a_0 value. In the one dimensional case, finding the optimal a_0 value is trivial, which is just the intensity of the border pixel in the hologram. However, in the two dimensional case, a simple repetition of each border pixel will create edges in orthogonal and diagonal directions. We therefore have to choose a different approach to extend the recorded hologram other than choosing a constant value.
A possible solution for matching the marginal values in two directions is to mirror the original hologram into each, orthogonal and diagonal direction. Mirroring matches the border values at each pixel while providing a reasonable continuation in every spatial direction. However, mirroring also shifts the truncation problem to the new borders, where the mirrored hologram ends. This problem is solved in the next section, by applying an appropriate window function. We define two operations to represent padding with a constant and mirroring as

$$\mathrm{pad}_c\left(\mathcal{I}_{\mathrm{det}}, a_0\right) = \mathrm{padconst}\left(\mathcal{I}_{\mathrm{det}}, a_0\right), \tag{4.20}$$

$$\mathrm{pad}_m\left(\mathcal{I}_{\mathrm{det}}\right) = \mathrm{mirr}\left(\mathcal{I}_{\mathrm{det}}\right). \tag{4.21}$$

4.1.3 Compensation with window functions

To find a reasonable solution of the truncation problem, we have to consider two aspects of the forward model that have an influence on the TR artifacts. The first aspect is that the Fresnel propagation kernel amplifies inconsistent structures, especially structures with high spatial frequencies, like edges. The second aspect is that the truncation causes spectral leakage in the discrete implementation of the Fourier transform in the propagation kernel, the Fast Fourier Transform (FFT). Conveniently, spectral leakage is a well studied problem in signal theory and a solution will also reduce the propagation problem of edge structures, which we see in the following.
A common approach to reduce spectral leakage is to introduce a slow fade towards the truncation edge. This is typically done by designing a window function to be applied to the data [87, 88]. Such a window is specifically designed to reduce the spectral leakage in the Fourier domain. A common approach is to fade the data with a Hamming, Hann or Blackman window function. However, applying these window functions significantly changes the data and therefore alters the reconstruction result. Especially for the reconstruction of physical values, this is an undesired behavior. Since we are interested in physical correctness of the reconstruction and not only in an optically appealing result, we need an alternative approach that (i) preserves the original data of the detector FOV , (ii) reduces spectral leakage and (iii) does not introduce artificial edges that will be propagated by the free-space propagation.

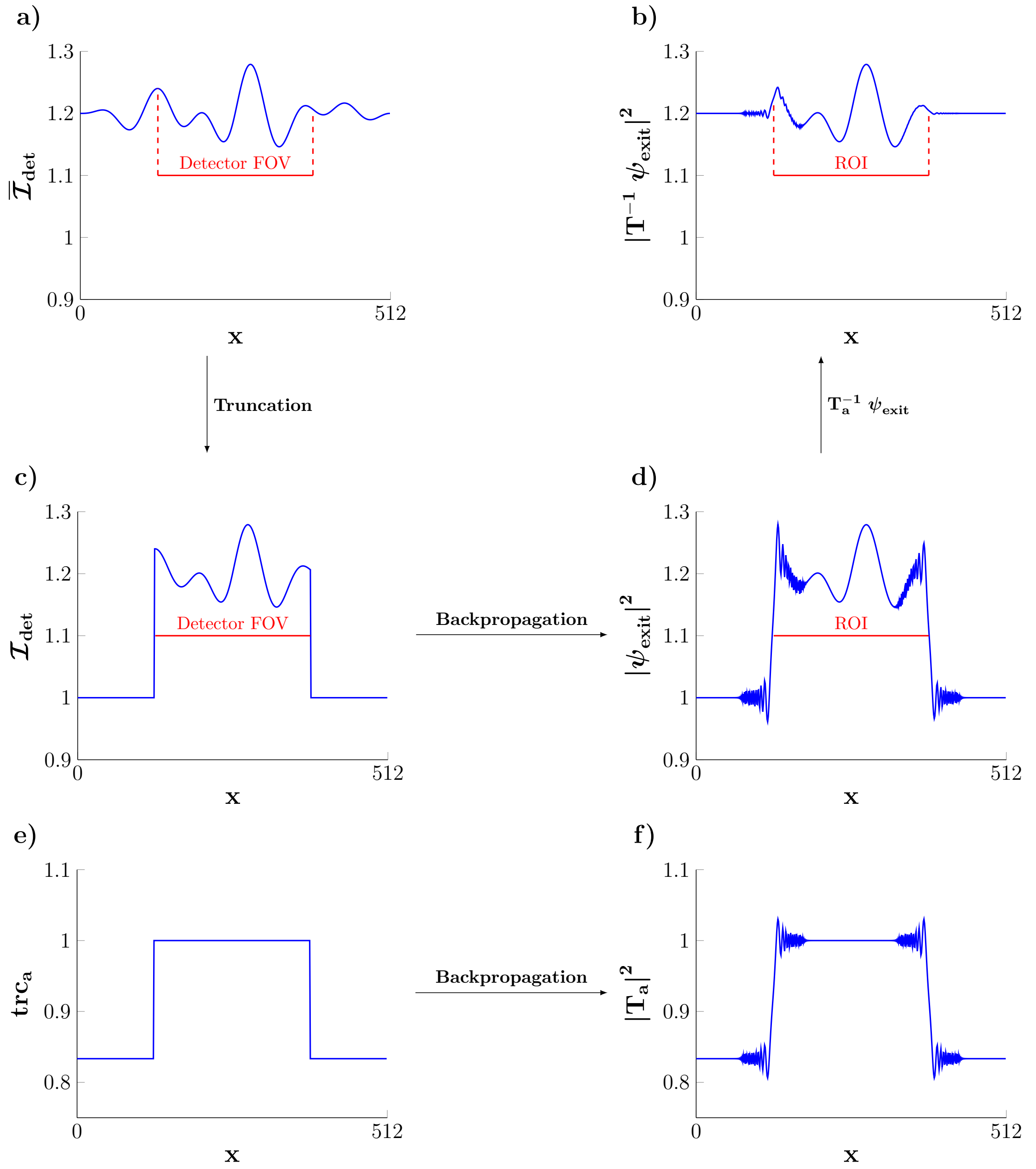

Figure 4.4: Demonstration of the truncation correction in the object plane by an approximated truncation-function. (a) Non-truncated hologram $\overline{\mathcal{I}}_{\mathrm{det}}(x)$ in the detector plane. (b) Intensities of non-truncated exit wave-field $\overline{\psi}_{\mathrm{exit}}(x)$. (c) Truncated hologram by function $\mathrm{trc}_1(x)$ (Eq. 4.3). (d) Intensities of $\psi_{\mathrm{exit}}(x)$, the back-propagated and truncated hologram, distorted by TR artifacts. (e) Approximated truncation function $\mathrm{trc}_a(x)$. (f) Intensities of T_a, the back-propagated truncation function. Multiplying the TR artifact distorted exit wave-field ψ_{exit} in (d), by the inverse of the back-propagated truncation function T^{-1}, removes most of the TR artifacts in the ROI, shown in (b).

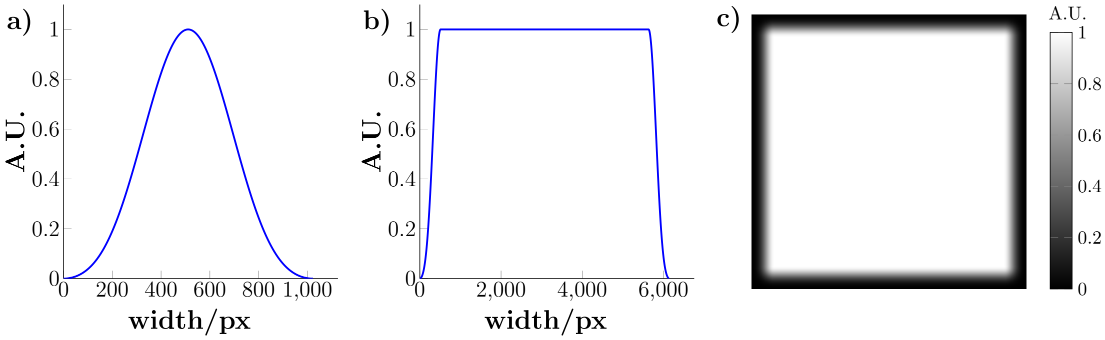

Figure 4.5: Blackman window function. (a) A one dimensional Blackman function is sampled to the size w of Eq. 4.22. (b) The window function is split in half and the gap filled with ones, until desired fading start and fading end is reached. From that, the two dimensional window function $\mathcal{W}$ (c) is derived by a repetition in each direction.

An assumption of the FFT is that the input data is periodic and the sampled data covers a full period and can therefore be repeated into each spatial direction. If the input data does not cover a full period of a signal, spectral leakage will occur again. The goal of fading towards a constant value is to transform the data into a pseudo periodic signal, before a Fourier transform is applied. As a value to which the data should be faded, the already derived constant a_0 of Sec. 4.1.2 can be used. Due to the previous mirroring, fading can now be performed outside the original hologram, without leaving an edge at its border. To this end, we have to modify the mentioned window functions that would otherwise alter the original hologram. A one dimensional Blackman window $y(x, y)$, for example, can be calculated by

$$y(w, x) = 0.42 - 0.5 \cdot \cos\left(\frac{2\pi x}{w-1}\right) + 0.08 \cdot \cos\left(\frac{4\pi x}{w-1}\right). \tag{4.22}$$

Here, w is the window width and x the one dimensional spatial coordinate. The process of creating a two dimensional fading window is shown in Fig. 4.5.

To preserve a fading free area in the center, we split the one dimensional window Fig. 4.5a at the center and continue to fill the gap with the constant value one, until the desired starting points and end points for the fading are reached. The result is then zero padded to match the size of the input data. The new one dimensional window is shown in Fig. 4.5b. From that, the two dimensional window function is derived by a repetition of the one dimensional function into each spatial direction, yielding Fig. 4.5c that leaves a rectangular shaped fading free area in the center. The extended hologram is then faded to a constant value a_0. Fading a mirrored hologram $\mathcal{I}_{\text{det}}$ with the two dimensional fading window $\mathcal{W}$ to the constant a_0 can than be realized by the function $\text{fade}\left(\mathcal{I}_{\text{det}}, a_0\right)$ with:

$$\text{fade}\left(\mathcal{I}_{\text{det}}, a_0\right) = \left[\left(\mathcal{I}_{\text{det}} - a_0\right) \otimes \mathcal{W}\right] + a_0, \tag{4.23}$$

where the operator ⊗ is the Hadamard product.

4.1.4 Preprocessing Approach

The developed compensation techniques for TR artifacts are summarized in a common preprocessing algorithm. This includes the FFC from Sec. 3.1, the mirroring approach of Sec. 4.1.2 and the window function approach of Sec. 4.1.3.

As a final step for data preprocessing, we still have to consider the required sampling rate of the Fresnel propagation kernel, which determines the minimum data size. According to the Nyquist criterion, at least two times the maximum frequency of the Fresnel propagation kernel is required. Although the kernel is a chirp and does not have a maximum frequency, it has been shown that this function should be sampled at least by $N \geq \frac{1}{\mathrm{Fr}}$ in each spatial direction, where Fr is the Fresnel number from Sec. 2.3 [71]. A possible method to match the required resolution in the frequency domain is to apply a constant padding operation on the hologram into each spatial directions. Since we have already faded the extended hologram towards a constant value a_0, we can pad with the same constant towards each spatial direction, until the required sampling rate for the Fresnel propagation kernel is reached. The final preprocessing algorithm is shown in Alg. 1 and illustrated in Fig. 4.6.

Algorithm 1: Preprocessing of reconstruction input $\mathcal{I}_{\mathrm{det}}$

```
Input: Detector data $\mathcal{I}_{\mathrm{raw}}$, synthetic flat field $\mathcal{I}_{\mathrm{flat}}$, Offset $a_0$
Output: Preprocessed detector data $\mathcal{I}_{\mathrm{cor}}$

$\mathcal{I}_{\mathrm{cor}} \leftarrow \frac{\mathcal{I}_{\mathrm{raw}}}{\mathcal{I}_{\mathrm{flat}}}$    ▷ Flat-field correction of the hologram
$\mathcal{I}_{\mathrm{cor}} \leftarrow \mathrm{pad}_m(\mathcal{I}_{\mathrm{cor}})$    ▷ Mirroring of the corrected hologram in eight directions
$\mathcal{I}_{\mathrm{cor}} \leftarrow \mathrm{fade}(\mathcal{I}_{\mathrm{cor}}, a_0)$    ▷ Application of a two dimensional, modified window function
$\mathcal{I}_{\mathrm{cor}} \leftarrow \mathrm{pad}_c(\mathcal{I}_{\mathrm{cor}}, a_0)$    ▷ Constant padding of the hologram with the value $a_0$
return $\mathcal{I}_{\mathrm{cor}}$
```

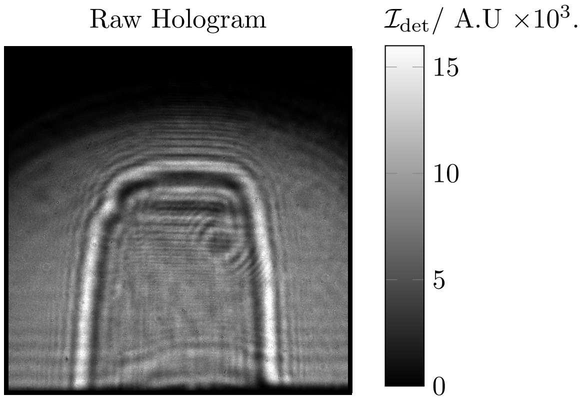

(a) Input hologram for preprocessing

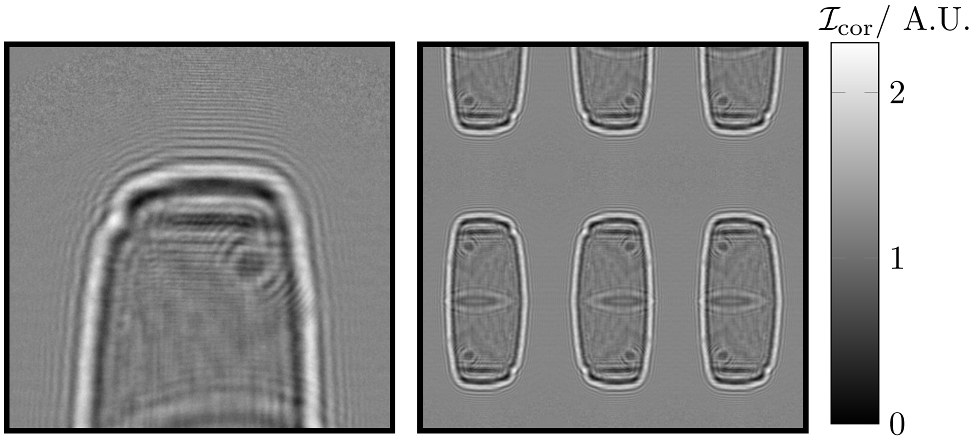

(b) As an approach to solve the truncation problem, the flat-field-corrected hologram (left) is mirrored in every spatial direction (right)

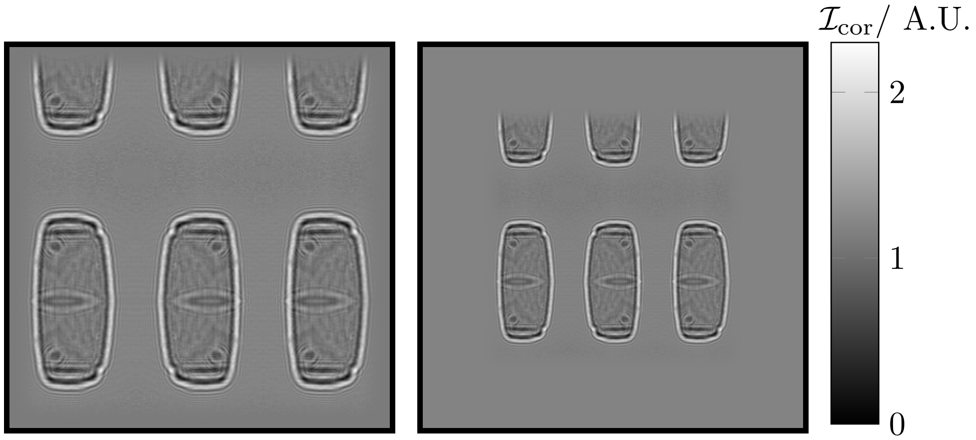

(c) The hologram is then multiplied by a modified Blackman window (left) to smoothen out the outer most borders after mirroring. The result is padded by a constant (right), to match the required sampling rate of the Fresnel propagation kernel.

Figure 4.6: Preprocessing scheme for a raw hologram to reduce structured distortions and to avoid TR artifacts.

4.1.5 Application to the reference algorithm

We also incorporate the prior information of how the input data is preprocessed as a regularization into the reference algorithm Alg. 0. We know that parts of the input hologram are a copy of the original hologram, faded by a window function. We also know that the marginal area has been padded by a constant value. In fact, the reconstructed object by the algorithm is only the central part of the reconstructed data. We can make use of this information in an additional step in the solver. At the end of each iteration, the current ROI of the reconstructed object will be cut out. At the beginning of each iteration, we repeat the preprocessing steps mirroring, fading and padding also for the reconstructed object. The new algorithm is shown in Alg. 2.

Algorithm 2: Basic reconstruction of $\tilde{O}$, which also considers the modified preprocessing.

```
Input: Preprocessed measurements $\mathcal{I}_{\text{cor}}$, update rate $\eta$ for the gradient step, Nesterov
       momentum $\gamma$, filter coefficients $\Omega_F$, initial guess $\tilde{O}_0$, maximum iterations $k_{\max}$
Output: Approximated solution $\tilde{O}^*$

$g_0 \leftarrow 0$
$k \leftarrow 0$
while $k < k_{\max}$ do
    $\tilde{O}'_k \leftarrow \text{gauss}_{\Omega_F}\left(\text{pad}_c\left(\text{fade}(\text{pad}_m\left(\tilde{O}_k\right), 0), 0\right)\right)$
    $y_{k+1} \leftarrow \tilde{O}'_k - \gamma g_k$
    $g_{k+1} \leftarrow \gamma g_k + \eta \nabla \left[\frac{1}{2} \left\| |\mathcal{D}_{\text{Fr}}(y_{k+1})| - \sqrt{\mathcal{I}_{\text{cor}}} \right\|_2^2\right]$
    $n_{k+1} \leftarrow \mathcal{P}_{\Omega_P}(\tilde{O}'_k - g_{k+1})$
    $\tilde{O}_{k+1} \leftarrow \text{cutroi}(n_{k+1})$
    $k \leftarrow k + 1$
end
$\tilde{O}^* \leftarrow \tilde{O}_{k_{\max}}$
return $\tilde{O}^*$
```

4.2 Offset in the Flat-Field-Correction

The FFC (Sec. 3.1) is a method to remove the structured distortions in the acquired hologram. Prior to the actual measurement of the hologram $\mathcal{I}_{\text{det}}$ with an object, several measurements without an object are carried out to characterize the empty beam. The hologram is then corrected by a division with an synthetic flat-field. In the ideal case, the division normalizes the model of the illumination to a constant one. Because of the dynamic of the beam, the synthetic flat-field can often not completely characterize fluctuations and this procedure only works up to a certain degree. After the flat-field-correction, we still observe noise, sometimes structured patterns of the measurement setup and a global normalization offset from the targeted constant one. In the following, we will investigate how a global offset in the normalization affects the reconstruction and manifests in low frequency (LF) artifacts.

4.2.1 Low frequency artifacts

We start the investigation of the source of LF artifacts resulting from a normalization offset, by first formally writing down the normalization of the global intensity. We recall that a flat-field corrected image $\mathcal{I}_{\mathrm{cor}}$ can be obtained with a division of the detector intensities $\mathcal{I}_{\mathrm{det}}$ with an synthetic flat-field $\mathcal{I}_{\mathrm{flat}}$:

$$\mathcal{I}_{\mathrm{cor}} = \frac{\mathcal{I}_{\mathrm{det}}}{\mathcal{I}_{\mathrm{flat}}} = \frac{|\psi_{\mathrm{det}}|^2}{\mathcal{I}_{\mathrm{flat}}}. \tag{4.24}$$

The wave-field in the detector plane ψ_{det} can be expressed as a multiplication of the illumination function ψ_0 with the object transfer function $\exp\left(\mathrm{i}\tilde{O}\right)$ and a subsequent convolution with the Fresnel free-space propagator:

$$\psi_{\mathrm{det}} = \mathcal{D}_{\mathrm{Fr}}\left(\exp\left(\mathrm{i}\tilde{O}\right)\psi_0\right), \tag{4.25}$$

The illumination ψ_0 contains a global intensity b_0 which should be normalized by the FFC. The synthetic flat-field also contains a global intensity c_0. We get the flat-field-corrected intensities $\mathcal{I}_{\mathrm{cor}}$ with:

$$\mathcal{I}_{\mathrm{cor}} = \frac{\left|\mathcal{D}_{\mathrm{Fr}}\left(\exp\left(\mathrm{i}\tilde{O}\right)\sqrt{b_0}\hat{\psi}_0\right)\right|^2}{c_0\hat{\mathcal{I}}_{\mathrm{flat}}}. \tag{4.26}$$

Since a convolution is a linear operation and the illumination has no negative amplitudes, the global intensity of the illumination can be isolated with

$$\mathcal{I}_{\mathrm{cor}} = \frac{b_0}{c_0}\frac{\left\|\mathcal{D}_{\mathrm{Fr}} \circledast \left(\exp\left(\mathrm{i}\tilde{O}\right)\hat{\psi}_0\right)\right|^2}{\hat{\mathcal{I}}_{\mathrm{flat}}}. \tag{4.27}$$

Part of the cost function Eq. 3.18 of the baseline algorithm is the regularization with a non-negative electron density constraint. The complex non-negativity constraint determines the physically correct interval of phase shift and absorption. While the forward model is invariant to a global constant phase shift, the reconstructed absorption is directly related to the global illumination amplitude of the input data for the reconstruction, i.e. $\mathcal{I}_{\mathrm{cor}}$. The absorption part of the non-negative electron density constraint set Ω_P was defined as

$$\mathrm{Im}(\Omega_P) = \left\{x \in \mathrm{Im}(\tilde{O}) : x \in [0, \infty]\right\}. \tag{4.28}$$

However, this is inaccurate. According to the Beer-Lambert law (Sec. 2.1.1), an absorption value is a relative value that is determined from the difference between the illumination intensity and the intensity of the exit wave-field. The lower threshold of one in Eq. 4.28 is therefore only correct for one specific illumination intensity, i.e. a value of one. A normalization different from one should be respected in the lower threshold. Specifically, the relationship between the normalization can be better described by the following non-negativity constraint for the absorption:

$$\mathrm{Im}(\Omega_P) = \left\{x \in \mathrm{Im}((\tilde{O})) : x \in [-\log(\sqrt{b_0/c_0}), \infty]\right\}. \tag{4.29}$$

The non-negativity constraint for the phase-shift values remains invariant with

$$\mathrm{Re}(\Omega_P) = \left\{x \in \mathrm{Re}(\tilde{O}) : x \in [-\infty, 0]\right\}. \tag{4.30}$$

The problem is illustrated in Fig. 4.7, which shows a series of reconstructed phase images of the tooth sample, with different normalization factors. We observe the appearance of nebular like LF artifacts. It can be seen that even a pattern which appears like a global phase shift, can be in fact an LF artifact, caused by an inconsistent absorption constraint. The forward model is invariant to global phase shifts and thus the artifact is not the result of a missing global phase-shift in the illumination model.

In case of an ideal global intensity normalization, it holds that $b_0/c_0 = 1$ and consequently $-\log(\sqrt{b_0/c_0}) = 0$, which matches the original constraint set Eq. 4.28. For deviations of the normalization from one, the original constraint set is wrong, which results in LF artifacts. In the following, we derive the modification Eq. 4.29 of the non-negative electron density constraint Ω_P.

4.2.2 Compensation with forward model adaption

In the following, we aim to correct for the global normalization error of the FFC.

We introduce a constant value a_0 in the reconstruction problem, which characterizes the normalization offset by the factor b_0/c_0 of Eq. 4.27 with

$$a_0 = \frac{b_0}{c_0}. \tag{4.31}$$

The incorporation of the offset correction can be done in multiple ways, depending on the interpretation. There are at least three interpretations, for each of which we can derive a separate reconstruction problem. They are all equivalent and can be transformed into each other.

We start from the perspective of a flat-field-correction. Here, the offset a_0 is a missing scaling factor in the empty beam components which have been previously derived by a PCA approach from empty beam images. Since the flat-field-correction is done by a division with an artificial flatfield, we can account for the scaling factor by an additional division after flat-field-correction to neutralize the quotient b_0/c_0 of Eq. 4.27. To

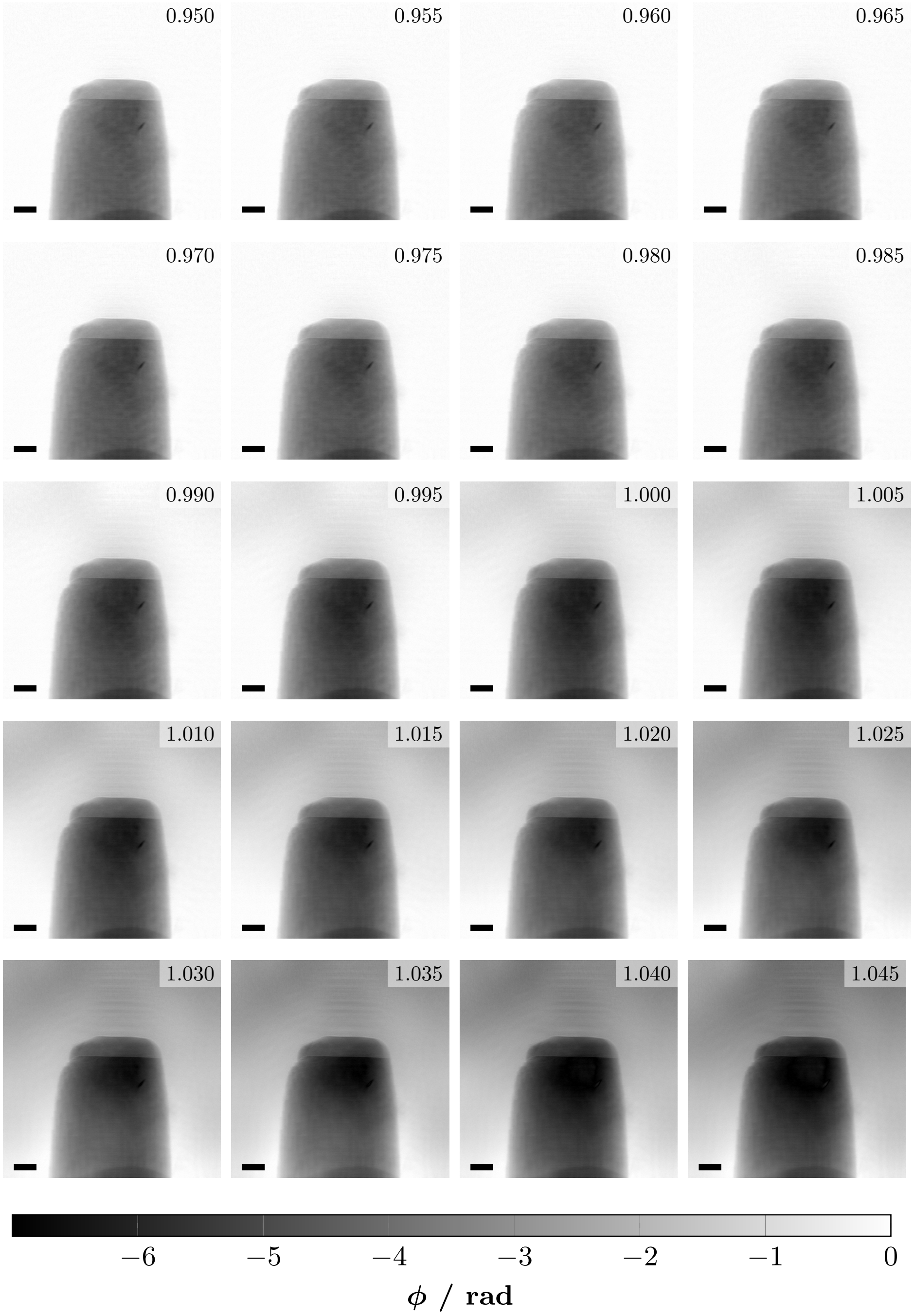

Figure 4.7: LF artifacts caused by a global offset in the FFC. Shown here is a reconstruction series of the tooth sample if an artificially introduced offset. The offset is achieved by a multiplication of the flat-field corrected image with a constant intensity a_0, whose value is shown in the upper right corner of each image. The reconstruction is sensitive to at least the third decimal place of a_0. The objects were already reconstructed by the improved algorithm of Sec. 4.5, to demonstrate this problem.

dynamically optimize the a_0 value with this interpretation, the reconstruction problem becomes

$$\tilde{O}^*, a_0^* = \underset{\tilde{O},\, a_0}{\operatorname{argmin}} \; \frac{1}{2} \left\| |\mathcal{D}_{Fr}(\tilde{O})| - \sqrt{\frac{\mathcal{I}_{\text{cor}}}{a_0}, 1} \right\|_2^2 + \mathcal{X}_{\Omega_P}(\tilde{O}) \tag{4.32}$$

with the non-negativity constraint

$$\Omega_P = \; \left\{ \forall \; x \in \tilde{O} : \operatorname{Re}(x) \in [-\infty, 0], \; \operatorname{Im}(x) \in [0, \infty] \right\}. \tag{4.33}$$

Another interpretation arises if we applied a truncation correction with constant padding, according to Sec. 4.1.2. The constant padding can be interpreted as the extension of the hologram with an empty beam area. The intensity in this area in the hologram is then equal to the intensity of the source $|\psi_0|^2$. This should be considered in the forward model by matching this value and introducing an additional constant illumination in the cost function. To dynamically optimize a_0 with this interpretation, the reconstruction problem becomes

$$\tilde{O}^*, a_0^* = \underset{\tilde{O},\, a_0}{\operatorname{argmin}} \; \frac{1}{2} \left\| |\mathcal{D}_{Fr}(\tilde{O})\sqrt{a_0}| - \sqrt{\operatorname{pad}_c\left(\mathcal{I}_{\text{cor}}, a_0\right)} \right\|_2^2 + \mathcal{X}_{\Omega_P}(\tilde{O}) \tag{4.34}$$

with the non-negativity constraint Ω_P for this variant:

$$\Omega_P = \; \left\{ \forall \; x \in \tilde{O} : \operatorname{Re}(x) \in [-\infty, 0], \; \operatorname{Im}(x) \in [0, \infty] \right\}. \tag{4.35}$$

A reformulation of this reconstruction problem gives us the non-negativity constraint that was shown in Eq. 4.29. To this end, we write down the Fresnel propagation $\mathcal{D}_{\text{Fr}}(\tilde{O})$ as

$$\mathcal{D}_{\text{Fr}}(\tilde{O}) = \hat{\mathcal{D}}_{\text{Fr}} \circ \exp\left(\mathrm{i}\tilde{O}\right) \tag{4.36}$$

$$\hat{\mathcal{D}}_{\text{Fr}} = \mathcal{F}^{-1} \circ \exp\left(-i \cdot \pi \frac{(k_x^2 + k_y^2)}{\text{Fr}} \right) \circ \mathcal{F} \tag{4.37}$$

and move the value a_0 into the transmission $\exp\left(\mathrm{i}\tilde{O}\right)$ function by

$$\begin{aligned}
\mathcal{D}_{\text{Fr}}(\tilde{O})\sqrt{a_0} &= \hat{\mathcal{D}}_{\text{Fr}} \circ \exp\left(\mathrm{i}\tilde{O}\right)\sqrt{a_0} \\
\mathcal{D}_{\text{Fr}}(\tilde{O})\sqrt{a_0} &= \hat{\mathcal{D}}_{\text{Fr}} \circ \exp\left(\mathrm{i}\tilde{O}\right)\exp\left(\log\sqrt{a_0}\right) \\
\mathcal{D}_{\text{Fr}}(\tilde{O})\sqrt{a_0} &= \hat{\mathcal{D}}_{\text{Fr}} \circ \exp\left(\mathrm{i}(\tilde{O} - i\log\sqrt{a_0})\right) \\
\mathcal{D}_{\text{Fr}}(\tilde{O})\sqrt{a_0} &= \mathcal{D}_{\text{Fr}}(\tilde{O} - \mathrm{i}\log\sqrt{a_0}).
\end{aligned} \tag{4.38}$$

Normalizing the hologram (Eq. 4.32) or introducing a constant illumination in the forward model (Eq. 4.34) is therefore equivalent to shifting the imaginary part of the reconstructed values, i.e. shifting the point of zero on the imaginary axis. We obtain a third reconstruction problem by considering this shift in the non-negativity constraint and adapt the lower threshold. We get:

$$\tilde{O}^*, a_0^* = \underset{\tilde{O},\, a_0}{\operatorname{argmin}} \frac{1}{2} \left\| |\mathcal{D}_{Fr}(\tilde{O})| - \sqrt{\mathcal{I}_{\text{cor}}} \right\|_2^2 + \mathcal{X}_{\Omega_P(a_0)}(\tilde{O}), \tag{4.39}$$

with the adapted non-negativity constraint Ω_P for this variant:

$$\Omega_P(a_0) = \left\{ x \in \tilde{O} : \operatorname{Re}(x) \in [-\infty, 0],\ \operatorname{Im}(x) \in [-\log(\sqrt{a_0}), \infty] \right\}. \tag{4.40}$$

The flat-field-correction offset a_0 can thus be both included as a hyper-parameter in the objective function in at least three different ways. It can also be used to find the correct value for the a_0 value of the truncation correction with constant padding in Sec. 4.1.2.

4.2.3 Application to the cost function

We saw in Sec. 4.2.2, that there are at least three possibilities to compensate LF artifacts by a correction of the global illumination offset. However, it is still an open research question whether the loss functions Eq. 4.32, Eq. 4.34 and Eq. 4.39 offer a good metric for the optimization of a_0. The constant a_0 could then be optimized for example by including it as an additional optimization parameter into the downhill simplex-based method of Ch. 5, which uses the same metric.

Until a good metric has been found, the cost function Eq. 3.18 here is therefore implicitly modified by changing the non-negative electron density constraint with the approach of Eq. 4.40. The value a_0 is then not automatically optimized and set as a prior. The PGD algorithm is not modified.

4.3 Overestimation of reconstructed values

The forward model of NFH is a non-linear model and the resulting reconstruction problem non-linear and non-convex. These types of inverse problems tend to have multiple local minima, which can trap or slow down iterative algorithms as they try to find a path to a global optimum. An algorithm may also converge to different local minima depending on the initial values. To overcome this problem, acceleration techniques can be used to speed up the algorithm and to escape local minima. One example is the NAG which can be added to gradient-based reconstruction methods. The NAG accumulates the gradient steps over multiple iterations and thereby increases the step size in the respective directions. This approach however entails the risk of overestimating the result in the direction of the accumulation. In NFH, the reconstruction is performed in a multidimensional space, where each dimension represents one pixel of the reconstructed image. Overestimating the gradient then yields an overestimation of single pixel values in the reconstructed image. In practice, this effect can be observed in reconstructions with an integrated Nesterov momentum by the appearance of extreme values in pixels that are locally isolated. Although reconstruction acceleration techniques like the NAG are needed to reduce trapping in local minima, overestimation prevents the application of reasonable high momentum values. This affects especially those components in the reconstructed objects, that have a low signal-to-noise ratio (SNR), i.e. that do not have a good representation in the forward model anyway. Section 4.4 has shown that those components are particularly low spatial frequencies of the reconstructed object. Overestimation due to high Nesterov momentum values has therefore two aspects that need to be addressed simultaneously: (i) maintaining high momentum values for low spatial frequency components while (ii) suppressing overestimation of single pixels, i.e. of high spatial frequencies. Before we derive a solution, we begin a deeper investigation into the source of the overestimation.

4.3.1 Overestimation artifacts

In the following, we investigate the appearance of overestimation (OE) artifacts in reconstruction results. The motivation of this chapter was the observation of those kind of artifacts, when the spatial support constraint was removed for the baseline algorithm Alg. 0. We therefore compare the algorithm behaviour with and without a spatial support constraint.

Figure 4.8 demonstrates the appearance of such OE artifacts in the reconstruction of the tooth sample. The number and strength of those artifacts increase with higher values of the Nesterov momentum. These OE artifacts will disappear again in later iterations, which can take a very long time. In general, there is a trade-off between acceleration strength by the Nesterov momentum and the appearance of OE artifacts which have to be balanced out. However, the reconstruction with a PGD-based algorithm is time intensive and thus a Nesterov momentum value as high as possible is desired. To maximize the Nesterov momentum, further improvements of the Nesterov acceleration technique are required that suppress the overestimation of single pixels.

We repeat the plot of Fig. 4.8 for both versions and also add the evolution of absorption values to the plot. The absorption is shown as the maximum absolute value in the current reconstruction result as a function over the iteration number, for the phase and absorption images respectively. The reconstruction was run with an enabled NAG for 5000 iterations. Figure 4.9a shows the results of a reconstruction without a spatial support. Here, it can be observed that the algorithm not only overestimates the result of the phase-shift values as it was already demonstrated in Fig. 4.8, but also the values of the absorption. Moreover, both components of the reconstructed refractive index follow a similar pattern and have their peak at iteration 500. In the reconstruction result of the phase-shift values we can mark a clearly visible OE artifact.

We now repeat the reconstruction but this time with a spatial support constraint that has been manually tuned beforehand and is statically defined. The result is shown in in Fig. 4.9b. Unlike the reconstruction result without a spatial support constraint, the final result here does not suffer from an OE artifact. However, it can be observed in

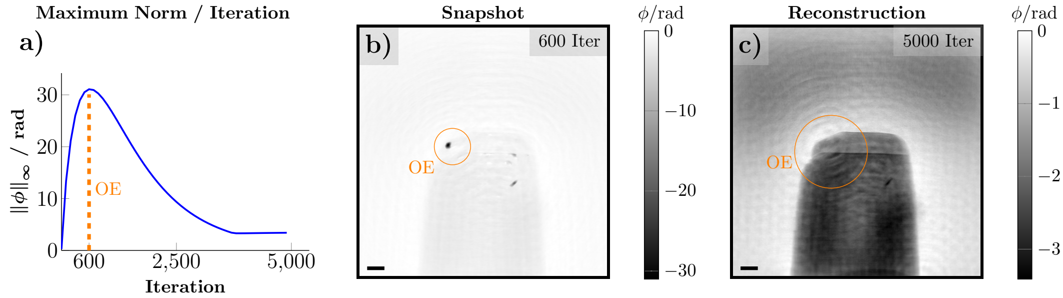

Figure 4.8: Overestimation of the phase shift values during a reconstruction. (a) Plot of the maximum norm of the reconstructed phase image over iterations. The overestimation happens during the first few hundred iterations and reaches a peak at iteration 600 at 30 rad. The algorithm needs around 2500 further iterations to recover. (b) Reconstructed phase image at iteration 600. The related OE artifact can be identified in the top left corner of the object. (c) Reconstructed phase image at iteration 5000. Residuals of the OE artifact from iteration 600 still visibly distort the image.

the maximum plots that a spatial support constraint does not prevent overestimation in general. On the contrary, the reconstruction process becomes rather more dynamical. The overestimation is stronger in the beginning but also recovers faster. Although the goal of the spatial support is to improve the final reconstruction result, the reconstruction time is still prolonged by the recovering process from the overestimation. The appearance of OE artifacts in the reconstruction result is therefore a general issue and not an issue of removing the spatial support constraint. Removing the constraint only changes the number of iterations that are necessary to recover from this type of artifact. In the following sections we derive two compensation techniques for OE artifacts from which we chose one for the final algorithm. The modification of Alg. 2 will be shown as a new algorithm Alg. 3.

4.3.2 δ/β Coupling

In both previous examples, a reconstruction without (Fig. 4.9a) and with a spatial support constraint (Fig. 4.9b), we can observe a similar pair-wise progress pattern for the maximum phase-shift and absorption values. We can argue from this behavior that there is probably a coupling between the absorption and the phase-shifting part of the reconstructed refractive index. A coupling is already known from physics, which is a material dependent coupling of the refractive index. This coupling is known as the δ/β coupling and has been quantitatively analyzed for many materials which can be looked up in various resources [43, 44, 74]. For single material objects, this coupling can be utilized as a regularization for the reconstruction by adding a proportionality constraint to the inverse problem. The regularization effectively reduces the required reconstruction values by half since either the real or the imaginary part of the refractive index is fixed by

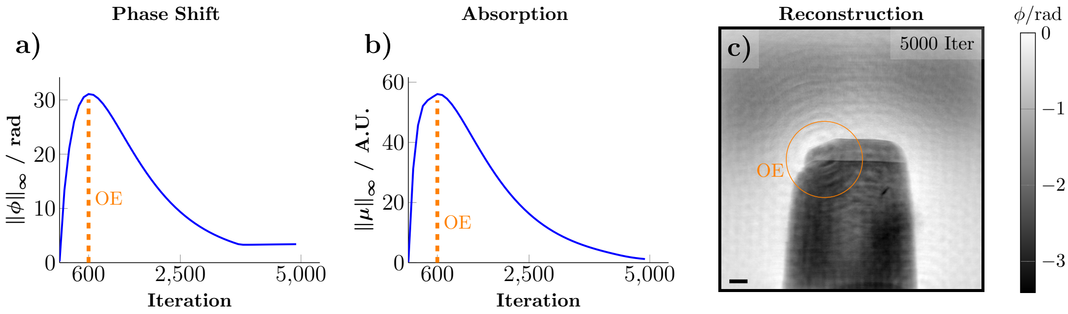

(a) Overestimation during a reconstruction without a spatial support constraint. The overestimation happens not only in the phase shift values (a) but also in the reconstructed absorption (b). The related intensity of the exit wave-field at the point of overestimation is $|\psi_{\text{exit}}| = \exp(-60) \approx 0$ at iteration 600. In the maximum plot, the algorithm took around 2500 iterations to recover. In the reconstructed phase image at iteration 5000 (c), residuals of the OE artifact from iteration 600 still visibly distort the image.

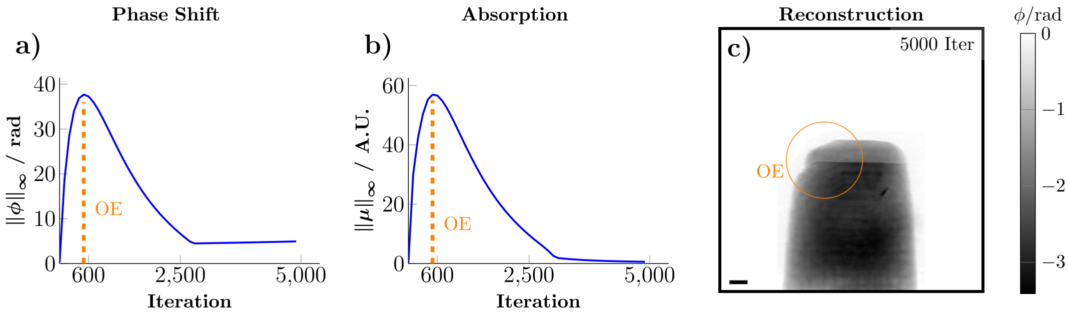

(b) Overestimation during a reconstruction with a spatial support constraint. The overestimation happens also here, not only in the phase shift values (a) but also in the reconstructed absorption (b). The overestimation is stronger than compared to a reconstruction without a spatial support constraint but also recovers fast. In the maximum plot, the algorithm took around 2000 iterations to recover. In the reconstructed phase image at iteration 5000 (c), residuals of the artifact are not visible.

Figure 4.9: Comparison of the overestimation effect between a reconstruction without (a) and with (b) a spatial support constraint. In both versions, it takes more than 2500 iterations to build up and recover the overestimation, which is a significant prolongation of reconstruction time.

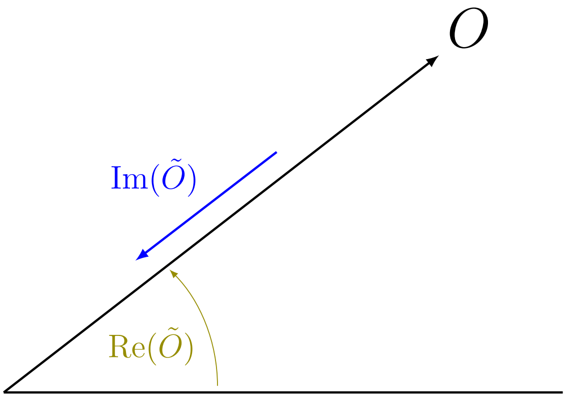

Figure 4.10: Sketch of the complex value of the TF $O = \exp\left(\mathrm{i}\tilde{O}\right)$ at an arbitrarily pixel. The complex value can be drawn as a vector with the polar coordinates $(|O|, \phi) = (\exp\left(-\mathrm{Im}(\tilde{O})\right), \mathrm{Re}(\tilde{O}))$. An overestimation of $\mathrm{Im}(\tilde{O})$, as in Fig. 4.9, causes the vector magnitude to vanish. In this course, the contribution of $\mathrm{Re}(\tilde{O})$ to the output of the forward model becomes negligible and $\mathrm{Re}(\tilde{O})$ cannot be reasonable reconstructed until the algorithm recovered. This effect potentially destabilizes the overall reconstruction.

the proportionality constraint. For multi-material objects however, this is not a feasible option because regularization with a δ/β coupling becomes arbitarely complex. For multiple materials, this approach requires advanced information about the measured specimen, i.e. the exact composition of materials per pixel.

A second type of coupling between the phase-shift and absorption values is of numerical nature, which can be exploited for a regularization. In the forward model Eq. 2.55, the refractive index representation $\tilde{O}$ of the object is transformed into the transmission function (TF) O:

$$O = \exp\left(\mathrm{i}\tilde{O}\right), \tag{4.41}$$

which essentially transforms $\tilde{O}$ into a polar coordinate representation of O. At each spatial position of O, the resulting vector has a magnitude related to $|O| = \exp\left(-\mathrm{Im}(\tilde{O})\right)$ which consequently decreases with increasing $\mathrm{Im}(\tilde{O})$. The argument of the vector is related to $\arg(\mathrm{Re}(\tilde{O}))$. The influences of $\mathrm{Re}(\tilde{O})$ and $\mathrm{Im}(\tilde{O})$ on the vector O are illustrated in Fig. 4.10. For absorption values $\mathrm{Im}(\tilde{O}) \to \infty$, the vector magnitude vanishes, which also suppresses the contribution of the argument to the output of the forward model.

We have seen in Sec. 4.4, that the forward model and the respective loss function of the reconstruction algorithm are sensitive to the Laplacian, the second derivative of the refractive index. With a discretization of O, a numerical differentiation at any point can be achieved by a weighted subtraction from the orthogonal neighbor points with the convolution kernel D^2_{xy}:

$$D_{xy}^2 = \begin{bmatrix} 0 & 1 & 0 \\ 1 & -4 & 1 \\ 0 & 1 & 0 \end{bmatrix}. \tag{4.42}$$

This is equal to the sum of four single subtractions of the center from neighbor points:

$$D_{xy}^2 = \begin{bmatrix} 0 & 1 & 0 \\ 0 & -1 & 0 \\ 0 & 0 & 0 \end{bmatrix} + \begin{bmatrix} 0 & 0 & 0 \\ 0 & -1 & 1 \\ 0 & 0 & 0 \end{bmatrix} + \begin{bmatrix} 0 & 0 & 0 \\ 0 & -1 & 0 \\ 0 & 1 & 0 \end{bmatrix} + \begin{bmatrix} 0 & 0 & 0 \\ 1 & -1 & 0 \\ 0 & 0 & 0 \end{bmatrix} \tag{4.43}$$

The subtraction of two points is the subtraction of two vectors $v_1 = (x_1, y_1)$ with angle ϕ_1 and $v_2 = (x_2, y_2)$ with angle ϕ_2 which results in a vector $v_r = (x_r, y_r)$ of length $|v_r|$ and angle ϕ_r. Length and angle are then given by

$$|v_r| = \sqrt{|v_1|^2 + |v_2|^2 + 2|v_1||v_2|\cos(\phi_2 - \phi_1)} \tag{4.44}$$

$$\phi_r = \phi_1 + \operatorname{arctan2}(|v_2|\sin(\phi_2 - \phi_1), |v_1| + |v_2|\cos(\phi_2 - \phi_1)). \tag{4.45}$$

Let the two vectors be defined by

$$v_1 = \exp\left(\mathrm{i}\tilde{O}_1\right) \tag{4.46}$$

$$v_2 = \exp\left(\mathrm{i}\tilde{O}_2\right). \tag{4.47}$$

For a very large absorption value of $\tilde{O}_2$, the last terms of Eq. 4.44 and Eq. 4.45 vanish and so does the contribution of the vector angle ϕ_2 to the result angle ϕ_r. Conversely, the contribution of the angle ϕ_2 on the objective function is the largest for $\operatorname{Im}(\tilde{O}_2) = 0$, if the absorption is constraint to positive values. A strong overestimation of $\operatorname{Im}(\tilde{O}_2)$ in one pixel therefore heavily interferes with the reconstruction of the phase-shift value ϕ_2. The same issue holds for $\tilde{O}_1$, respectively. In the following we will consider two regularization approaches for absorption values to suppress overestimation to enable a better reconstruction of the phase values.

4.3.3 Compensation with phase-object constraint

An edge case for the regularization of absorption values during the reconstruction is the introduction of a phase-object assumption. A phase object is a sample that does not absorb and is purely phase-shifting. This prior can be added as a strong regularization to the reconstruction by a modification of the non-negativity constraint such that

$$\Omega_P = \left\{x \in \tilde{O} : \operatorname{Re}(x) \in [-\infty, 0],\ \operatorname{Im}(x) = 0\right\}. \tag{4.48}$$

We will now run another reconstruction without a spatial support constraint and with the proposed phase-object assumption. The result can be seen in Fig. 4.11.
Here we can observe that the overestimation disappears completely with this constraint. The reconstruction of the maximum phase-shift value follows a monotonous curve and

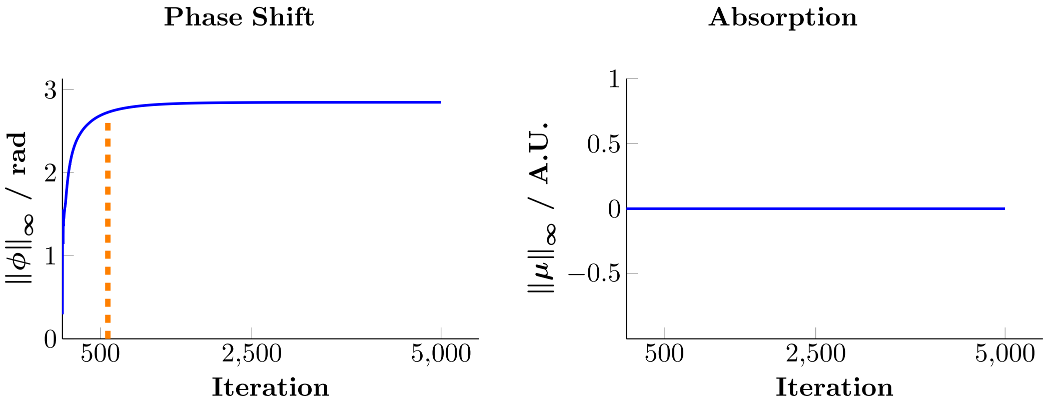

Figure 4.11: Maximum norm of the phase shift and absorption values shown as a function of the iteration number for a reconstruction with a phase-object constraint and without a spatial support constraint. Although the same parameters have been used as before, the overestimation of the phase shift values disappear completely. This is an indication that the vanishing vector theory of Sec. 4.3.2 might indeed be the problem of the overestimation effect.

converges during the first few hundred iterations to a maximum value. In the further progress, this value only increases slowly. The course of the curve can be interpreted as the following. During the first few hundred iterations, the algorithm starts to resolve the high gradient components, i.e. the edges of the reconstructed object due to the forward model bias, c.f. Fig. 4.13. After the edges are resolved, more smaller gradient contributions are added to the reconstruction result. Adding the lowest gradient components to the reconstruction result is then visible as a less steep curve in Fig. 4.11.

With this approach, we have introduced an absolute regularization bias into the result which may be too strong for objects with a strong absorption. One solution could be to remove the phase-object constraint after some time and also enable the reconstruction of absorption values. For high absorbing objects however, the phase-object constraint entails two issues. First, the reconstruction speed of the absorption will be reduced since the reconstruction of absorption values is completely prevented during the first few hundred iterations. Second, the induced error by the constraint scales up rapidly with the interaction strength of the measured object. The consequences could be a performance loss in total. A more reasonable approach would be a moderate regularization of the reconstructed absorption values.

4.3.4 Compensation with regularization of $\mathrm{Im}(\tilde{O})$

In this section we will derive a regularization of the absorption values, which, in contrast to a pure phase-object constraint, can be dynamically controlled by a regularization weight. The regularization should consider each pixel individually and should be self-scaling to avoid excessive regularization for high absorption values which are part of the reconstructed object and not the result of overestimation. The introduced reconstruction bias by the regularization should be as conservative as possible to minimize the induced reconstruction error, especially for strong interacting objects. The goal of the regularization is to prevent vanishing transmission in the function O of Eq. 4.41 as described in Sec. 4.3.2. A Tikhonov regularization with an $\|\cdot\|_2^2$-term is a possible choice which is a smooth function and is applied pixel wise. It also enables controlling of the regularization strength with a prior weight factor β. However, because of the square in the regularization term, the regularization strength and therefore the introduced reconstruction error scales quadratically. To have a better scaling for high absorption values, we remove the square and get the non-quadratic and non-smooth regularization $\|\cdot\|_2$. To employ the regularization, we extend the objective function by an L_2 term for the absorption values, i.e. the imaginary part of $\tilde{O}$. The modified objective function becomes

$$\tilde{O}^* = \underset{\tilde{O}}{\operatorname{argmin}} \frac{1}{2} \left\| \left|\mathcal{D}_{\mathrm{Fr}}(\tilde{O})\right| - \sqrt{\mathcal{I}_{\mathrm{det}}} \right\|_2^2 + \mathcal{X}_{\Omega_P}(\tilde{O}) + \beta \|\mathrm{Im}(\tilde{O})\|_2. \tag{4.49}$$

There are two different ways to integrate the regularization into our solver, the PGD-based algorithm. One possibility is to include a proximal operator. Our goal is to not only apply the regularization onto the solution but also include the regularization into the gradient or more specific, into the Nesterov acceleration. We can account for this additional L_2 regularization by a slight modification of the gradient. We first define a new basis function $\hat{f}(\tilde{O})$ for which the gradient step should be applied, which is then the data feasibility term together with the weighted L_2 regularization

$$\hat{f}(\tilde{O}) = f(\tilde{O}) + \beta \|\mathrm{Im}(\tilde{O})\|_2, \tag{4.50}$$

$$\hat{f}(\tilde{O}) = \frac{1}{2} \left\| \left|\mathcal{D}_{\mathrm{Fr}}(\tilde{O})\right| - \sqrt{\mathcal{I}_{\mathrm{det}}} \right\|_2^2 + \beta \|\mathrm{Im}(\tilde{O})\|_2. \tag{4.51}$$

For this new objective function, we can calculate the gradient, which is the original gradient $\nabla f(\tilde{O})$ and the derivative of the L_2 term, that is applied on the absorption value, i.e. the imaginary part of $\tilde{O}$

$$\nabla \hat{f}(\tilde{O}) = \begin{cases} 0 & \text{if } \tilde{O} = 0 \\ \nabla f(\tilde{O}) + i \cdot \beta \cdot \frac{\mathrm{Im}(\tilde{O})}{\|\mathrm{Im}(\tilde{O})\|_2} & \text{else} \end{cases}. \tag{4.52}$$

Since the derivative for the L_2 norm is undefined at $\mathrm{Im}(\tilde{O}) = 0$, we have to account for that by handling this case separately. The gradient $f(\tilde{O})$ was already defined for this case, yielding a global definition which is just setting the gradient to zero.

We test the new approach with a reconstruction run and replace the phase-object assumption from Sec. 4.3.3 with an L_2 regularization on the absorption values. We should switch off the strong regularization at a certain time point to remove the reconstruction

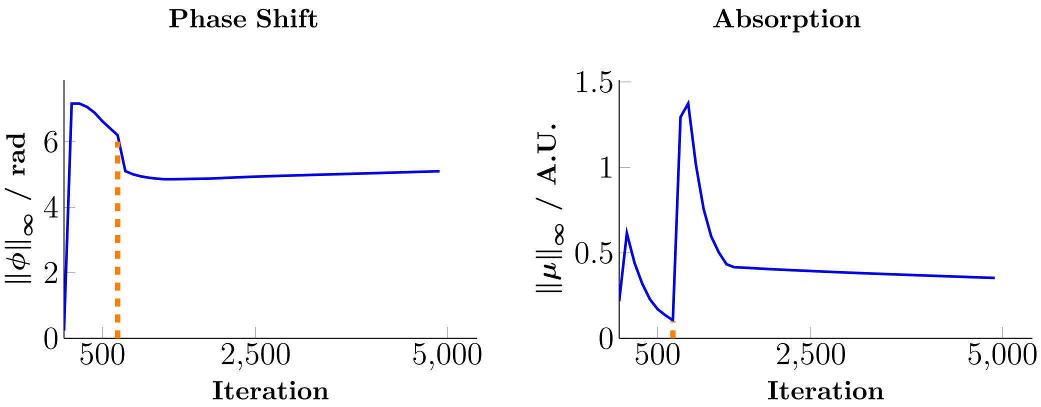

Figure 4.12: Maximum norm of the phase shift and absorption values plotted against the number of iterations for a reconstruction without a spatial support constraint. As an approach, the reconstruction here is extended by a warm-up phase during the first 700 iterations, where the overestimation occurred before. In the warm-up phase, the absorption values $\mathrm{Im}(\tilde{O})$ are strongly regularized. This prevents vanishing magnitudes of the TF O, while still allowing the reconstruction of absorption values, in contrast to a phase-object constraint of Sec. 4.3.3.

bias and give the algorithm time to converge to the best physically valid solution such that the function $\hat{f}(\tilde{O})$ for calculating the gradient becomes

$$\hat{f}(\tilde{O}) = \begin{cases} f(\tilde{O}) + \beta \|\mathrm{Im}(\tilde{O})\|_2 & \text{for iterations} \leq N \\ f(\tilde{O}) & \text{else} \end{cases} . \tag{4.53}$$

For the next reconstruction run, we set the stopping criterion for the regularization to an iteration number shortly after the previous overestimation peak in Fig. 4.8 with $N = 700$. Since the algorithm is already in the recovering process after this point, we can expect that further overestimation of single pixel will not be a significant issue after we switched of the regularization. The resulting maximum norm plots are shown in Fig. 4.12. Here we can observe the following effects: Although phase-shift and absorption values are reconstructed simultaneously, the overestimation during the first few hundred iterations is significantly suppressed. The absorption values converge during the regularized reconstruction to regularization bias distorted values in the order of 10^{-1}.

4.3.5 Application to the reference algorithm

We extend the algorithm Alg. 2 by the overestimation suppression approach of this section. The approach is a regularization of the absorption values with an L_2 term. The regularization is weighted with a factor β, which has to be specified as an input of the reconstruction. In addition to the main loop, the algorithm is extended by a second sub loop to enable updates of the regularization weights during the reconstruction. The L_2 term is applied in the gradient descent step, together with the gradient of the data fidelity term. To separate the step-size of the gradient and the regularization weight of the L_2 term, the weight β is divided by the step-size ∇. The resulting algorithm is shown in Alg. 3.

Algorithm 3: Reconstruction of $\tilde{O}$ with L_2 regularization for $\mathrm{Im}(\tilde{O})$

Input: Preprocessed measurements $\mathcal{I}_{\mathrm{cor}}$ by Alg. 1, list of update rates η for the gradient step, list of Nesterov momentum values γ, list of filter coefficients Ω_F, list of L_2 regularization weights β, initial guess $\tilde{O}_0$, list of maximum iterations k_{max}, parameter j_{max} is given by the list lengths

Output: Approximated solution $\tilde{O}^*$

```
$g_0 \leftarrow 0, \; j \leftarrow 0$
// Regularization levels
while $j < j_{\mathrm{max}}$ do
    $k \leftarrow 0$
    // Iterate in given level
    while $k < k^j_{\mathrm{max}}$ do
        $\tilde{O}'_k \leftarrow \mathrm{gauss}_{\Omega^j_F}\left(\mathrm{pad}_c\left(\mathrm{fade}(\mathrm{pad}_m\left(\tilde{O}_k\right), 0), 0\right)\right)$
        $y_{k+1} \leftarrow \tilde{O}'_k - \gamma^j g_k$
        $g_{k+1} \leftarrow \gamma^j g_k + \eta^j \nabla \left[\frac{1}{2} \left\| |\mathcal{D}_{\mathrm{Fr}}(y_{k+1})| - \sqrt{\mathcal{I}_{\mathrm{cor}}} \right\|_2^2 + \frac{\beta^j}{\eta^j} \|\mathrm{Im}(()y_{k+1})\|_2\right]$
        $n_{k+1} \leftarrow \mathcal{P}_{\Omega_P}(\tilde{O}'_k - g_{k+1})$
        $\tilde{O}_{k+1} \leftarrow \mathrm{cutroi}(n_{k+1})$
        $k \leftarrow k + 1$
    end
    $g_0 \leftarrow g_{k^j_{\mathrm{max}}}$
    $\tilde{O}_0 \leftarrow \tilde{O}_{k^j_{\mathrm{max}}}$
    $j \leftarrow j + 1$
end
$\tilde{O}^* \leftarrow \tilde{O}_0$
return $\tilde{O}^*$
```

4.4 Forward model induced reconstruction bias

The forward model is the core component of the inverse problem of Eq. 3.18. It does not only describes the measured data with respect to the measured object but also amplifies or damps certain features. In other words, it describes the contribution of each object feature to the detector signal and therefore simultaneously to the loss function. It is reasonable to argue that algorithms based on the steepest gradient approach will probably reconstruct the features of the reconstruction target in the order of their impact on the loss function value. The resulting behavior can be described as a forward model reconstruction bias. For object features which have a large impact on the reconstruction target, but a small impact on the loss function, this is quite problematic and can result in artifacts in the order of the feature size. These artifacts can for example appear due to an insufficient SNR, stagnation of the algorithm or an incomplete convergence.

This section aims to describe the reconstruction bias that is induced by a mathematical property of the Fresnel propagation kernel in particular. We will assign the forward model induced reconstruction bias to two types of artifacts and will also derive two compensation techniques to counteract the bias. The two techniques will be combined to a common approach.

4.4.1 Weak reconstruction artifacts

In the following, we investigate, which structures in the object $\tilde{O}$ have the most impact on the cost function Eq. 3.18. For this purpose, we calculate the Taylor expansion of first order of the convolution kernel h of the Fresnel propagation operator Eq. 2.54, which is

$$h(k) = \exp\left(-i \cdot \pi \frac{(k_x^2 + k_y^2)}{\mathrm{Fr}}\right), \tag{4.54}$$

with respect to the k-space coordinates $k = (k_x, k_y)$. The Taylor expansion $\mathcal{T}_1$ of first order around the point $(0, 0)$ yields the following:

$$\mathcal{T}_1 h(k; 0) = 1 - i \cdot \pi \frac{(k_x^2 + k_y^2)}{\mathrm{Fr}}. \tag{4.55}$$

The n-th derivative in the spatial domain can be expressed by a multiplication in the Fourier domain with the factor $(i2\pi k)^n$. With a substitution for the second derivative, we can rewrite the Taylor expansion $\mathcal{T}_1$ as

$$\mathcal{T}_1 h(k; 0) = 1 + \frac{i}{4\pi\mathrm{Fr}} (i2\pi)^2 (k_x^2 + k_y^2). \tag{4.56}$$

Replacing the convolution kernel in the Fresnel propagation operator gives us the approximated Fresnel propagation operator $\mathcal{D}_{\mathrm{Fr}}(\tilde{O})$ as

$$\mathcal{D}_{\mathrm{Fr}}(\tilde{O}) \approx \mathcal{T}_1 h(k; 0) \circ \exp\left(\mathrm{i}\tilde{O}\right) = \exp\left(\mathrm{i}\tilde{O}\right) + \frac{\mathrm{i}}{4\pi\mathrm{Fr}} \nabla^2 \exp\left(\mathrm{i}\tilde{O}\right) \tag{4.57}$$

and with the Taylor expansion of the expression $\exp\left(\mathrm{i}\tilde{O}\right)$, a rough estimation of the signal intensities $\mathcal{I}_{\mathrm{cor}}$ can be calculated by

$$\mathcal{I}_{\mathrm{cor}} \propto |1 + i\tilde{O} + \frac{i}{4\pi\mathrm{Fr}}\nabla^2 i\tilde{O}|^2 \propto |i\tilde{O}| + |\nabla^2 i\tilde{O}|. \tag{4.58}$$

In other words, the detector signal is strongly related to the X-ray transmission and the second spatial derivative of the measured object. For weakly interacting objects, i.e. measured specimens that are nearly pure phase objects, the first term can be neglected and the signal in the detector is dominated by the second spatial derivative. This has significant consequences to the acquired data and the inverse problem. The detector signal and hence the signal-to-noise ratio in the data decreases with the smoothness of object features. Furthermore, the contribution to the function decreases with the smoothness of features, which nevertheless can be large features. This can be observed by the behavior of iterative reconstruction algorithms that object edges, i.e. high spatial frequencies, are reconstructed first while smooth areas, i.e. low spatial frequencies, require a high amount of iterations. This behaviour is illustrated in Fig. 4.13.

If the algorithm stops too early, this can lead to artifacts in form of low frequency patterns (LF artifacts) and weakly reconstructed areas (weak reconstruction (WR) artifacts), especially in areas where the object is smooth. This problem can also appear if the algorithm is stuck in a local minimum and the weakly reconstructed area cannot be resolved even with infinite iterations. Due to the low contribution of those smooth areas to the objective function, it is difficult to judge the progress and quality of the reconstruction only from convergence of the algorithm and the absolute loss value. For higher iteration numbers, the residual loss can be low while the object lacks the reconstruction of large areas.

4.4.2 Compensation with a multigrid approach

The contribution of object features to the data fidelity term of the loss function in Eq. 3.18 decreases from high spatial frequencies to low spatial frequencies, which was explained in Sec. 4.4.1. This can also be interpreted as a characteristic of different convergence rates for different spatial frequencies. A common strategy to account for that is to implement a multigrid method. For this purpose, the reconstruction is split into multiple phases, each allowing for the reconstruction of different length scales with different weights. A Cartesian grid is used which number of sampling nodes increases successively during the reconstruction, i.e. down- and up-sampling. Cartesian down-sampling of an image is a linear operation, a multiplication of the original image with a down-sampling operator $S_{\downarrow}$. The inverse operation is an up-sampling operator $S_{\uparrow}$ that interpolates the down-sampled data onto a finer grid. We get the inverse problem with a Cartesian multigrid approach by adding both operators to the inverse problem such

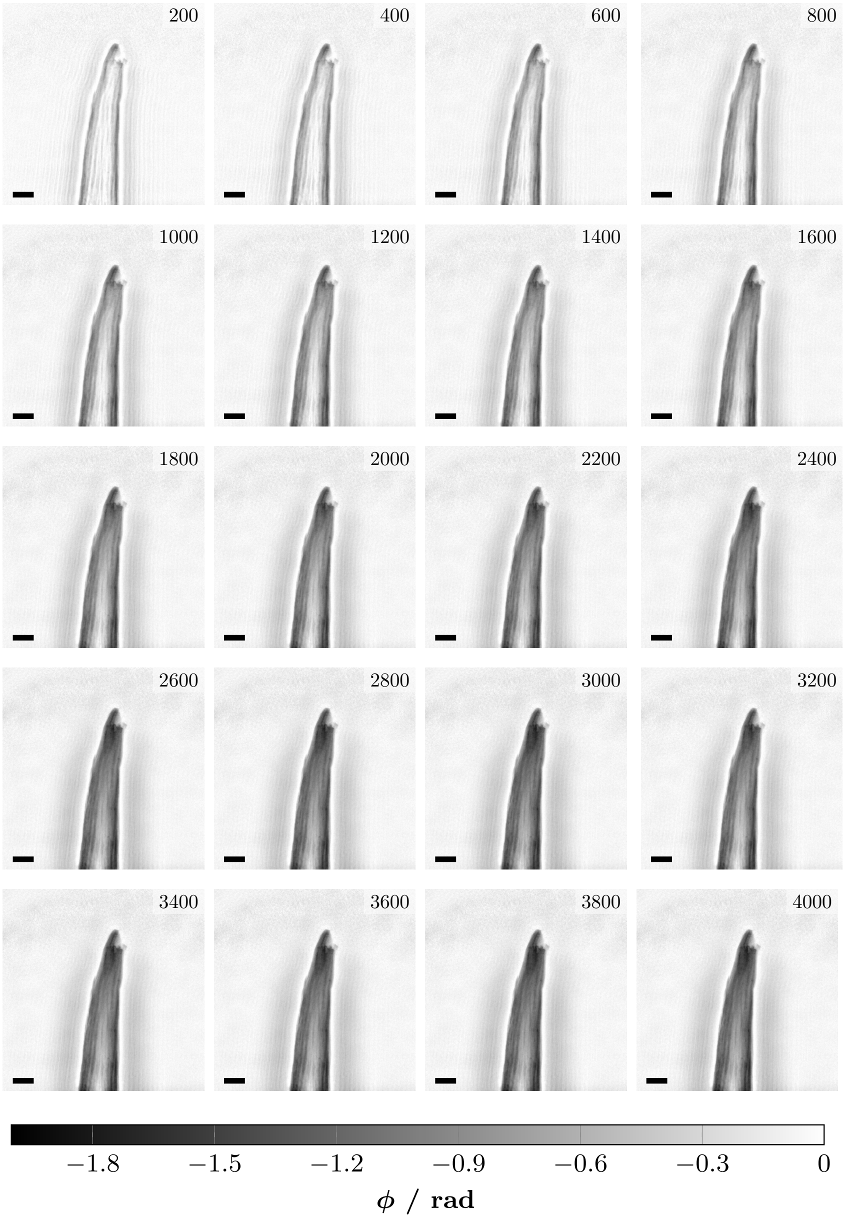

Figure 4.13: Demonstration of the forward model induced reconstruction bias. The figure shows the reconstruction progress of the phase image of the cactus needle sample by a PGD-based approach for solving Eq. 3.18. The algorithm reconstructs the object in the order of feature length scales. Due to the derivation property of the forward model (Eq. 4.58), the edges with the highest loss contribution are reconstructed first, while the smooth objects interior with small spatial gradients takes many iterations to reconstruct. For demonstration purpose, the Nesterov acceleration was turned off by setting $\gamma = 0$. The number at the top right corner shows the iteration number, the scale bar indicates 20 µm.

that we get a reconstruction result $\tilde{O}_j$ on grid j and the respective solution $\tilde{O}$ on the original grid with:

$$\tilde{O}_j^* = \underset{\tilde{O}}{\operatorname{argmin}} \frac{1}{2} \| |\mathcal{D}_{Fr}(\tilde{O})| - \sqrt{S_{\downarrow}^{j} \mathcal{I}_{\text{det}}} \|_2^2 + \mathcal{X}_{\Omega_P}(\tilde{O}), \tag{4.59}$$

$$\tilde{O}^* = S_{\uparrow}^{j} \tilde{O}_j^*. \tag{4.60}$$

In an iterative algorithm approach, the reconstruction can iterate on different grids $S_{\downarrow}^{j}$, $j \in [0, N]$ starting with the highest downsampling factor $j = 0$. The measured data is than sampled onto this grid by the operation $S_{\downarrow}^{j} \mathcal{I}_{\text{det}}$ in the equation above. The reconstruction on each grid is performed until a stopping criterion is reached, for example a fixed iteration number. The solution $\tilde{O}_j^*$ is then interpolated onto a higher grid by the operation $\tilde{O}_{\text{init}} = S_{\downarrow}^{j+1} S_{\uparrow}^{j} \tilde{O}_j^*$ and can be used as an initial guess for further iterations on this higher grid. This process is repeated until the highest resolution grid is reached. The reconstruction is thereby extended by new hyper-parameters, the grid resolution and the iteration number for each grid. Although the algorithm complexity is now increased by the introduction of hyper-parameters, there is a big advantage in computational time. With the same number of iterations, by introducing a multigrid approach, the computation time scales down with the reduction factor of grid nodes. Furthermore, a multigrid approach is a convenient way to stabilize the algorithm since certain critical weights like the gradient update rate and the Nesterov momentum can now be chosen with respect to the reconstructed feature length scale.

4.4.3 Compensation with adaption of Nesterov momentum weights

With the multigrid approach of Sec. 4.4.2, we increased the flexibility of the reconstruction algorithm by introducing length scale specific regularization. We now change the perspective from the spatial domain and interpret the multigrid approach from the view of the Fourier domain. For Cartesian sub-grids, down-sampling reduces the limit of HF which will be included into the reconstruction. Depending on the down-sampling factor, HF and therefore details with small length scales are regularized in the reconstruction. We aim to further refine this length scale specific regularization by introducing an additional non-linear approach to control the reconstruction strength of different frequency components. The goal is to counter the reconstruction bias from the forward model without altering too much with the reconstruction result. To this end, instead of changing the loss function, we adapt the reconstruction acceleration step of the NAG such that the acceleration of the low frequency components is increased. The NAG ∇g is given as

$$\nabla g(\tilde{O}_i) = \gamma \nabla g(\tilde{O}_{i-1}) + \eta \nabla f(\tilde{O}_i - \gamma \nabla g(\tilde{O}_{i-1})). \tag{4.61}$$

Here, γ is the Nesterov momentum, a constant weight factor which is uniform distributed over all frequencies. To adapt the acceleration strength of different frequencies, we change the distribution of γ in the frequency domain to a Gaussian distribution in the frequency domain with a mean of zero and a variance of σ. The gradient, which will be accelerated, first needs to be transformed into the Fourier domain where the non-uniform weight factor will be applied. We summarize the necessary steps into a common operator $\tau(\gamma, \sigma)$ that replaces the original Nesterov momentum γ with

$$\tau(\gamma, \sigma) = \gamma \mathcal{F}^{-1} \circ \exp\left(-2\pi^2(k_x^2 + k_y^2)\sigma^2\right) \circ \mathcal{F}. \tag{4.62}$$

Note, that with the adaption of the Nesterov momentum, we did not change the length scales of the reconstruction, which is defined by the grid S^j of the previous section, but rather the acceleration of different length scales. The original gradient remains untouched, allowing for the reconstruction of every length scale on the defined grid. With this approach, we get a new hyper-parameter to be tuned which is σ, the variance of the Gaussian Nesterov momentum.

4.4.4 Algorithm Extension

We extend the algorithm Alg. 2 by a suppression of HF components with approaches of this section. The HF suppression approach is a selective treatment of different spatial frequency and is focused on improving the reconstruction of low spatial frequencies while simultaneously reducing the reconstruction of high spatial frequencies. The first technique is a multigrid approach. In addition to the main loop, the algorithm is extended by a second sub loop to enable iterations on different grids. The operator $S^j_\downarrow$ samples the measurement on the respective grid with index j. The grid is updated outside of the sub loop by the operator $S^j_\uparrow$. The second technique is a modification of the NAG. For this purpose, the Nesterov momentum γ of Alg. 2 is replaced by the operator τ of Eq. 4.62. The resulting algorithm is shown in Alg. 4.

4.5 Artifact suppressing reconstruction method

In this section, the single reconstruction artifact suppression techniques developed in this chapter (sections 4.1 to 4.4) will be combined into a common ASRM. The algorithm consists of three parts: (i) The data preprocessing, whose techniques were presented in Sec. 3.1 and Sec. 4.1. (ii) The formulation of the objective function, which is to be optimized to reconstruct the refractive index. This is based on Eq. 3.18 and is extended by artifact reduction techniques from sections 4.2 to 4.4. (iii) The solver that minimizes the objective function. This is based on the solver presented in Sec. 3.2.2.

4.5.1 Data Preprocessing

The data preprocessing prepares the raw data from the detector such that the assumptions for the respective reconstruction algorithm are met. This includes the removal of

Algorithm 4: Reconstruction of $\tilde{O}$ with HF suppression

```
Input: Preprocessed measurements $\mathcal{I}_{\text{cor}}$ by Alg. 1, list of update rates $\eta$ for the gradient
       step, list of Nesterov momentum operators $\tau$, list of filter coefficients $\Omega_F$, list of
       down- and upsampling operators $S_\downarrow, S_\uparrow$, initial guess $\tilde{O}_0$, list of maximum
       iterations $k_{\max}$, parameter $j_{\max}$ is given by the list lengths
Output: Approximated solution $\tilde{O}^*$

$g_0 \leftarrow 0,\ j \leftarrow 0$
// Regularization levels
while $j > j_{\max}$ do
    $k \leftarrow 0$
    // Iterate in given level
    while $k < k^j_{\max}$ do
        $\tilde{O}'_k \leftarrow \text{gauss}_{\Omega^j_F}\left(\text{pad}_c\left(\text{fade}(\text{pad}_m\left(\tilde{O}_k\right), 0), 0\right)\right)$
        $y_{k+1} \leftarrow \tilde{O}'_k - \tau^j g_k$
        $g_{k+1} \leftarrow \tau^j g_k + \eta^j \nabla \left[\frac{1}{2}\left\| |\mathcal{D}_{\text{Fr}}(y_{k+1})| - \sqrt{S^j_\downarrow \mathcal{I}_{\text{cor}}}\right\|^2_2\right]$
        $n_{k+1} \leftarrow \mathcal{P}_{\Omega_P}(\tilde{O}'_k - g_{k+1})$
        $\tilde{O}_{k+1} \leftarrow \text{cutroi}(n_{k+1})$
        $k \leftarrow k + 1$
    end
    $\tilde{O}_0 \leftarrow S^j_\uparrow \tilde{O}_{k^j_{\max}}$
    $g_0 \leftarrow S^j_\uparrow g_{k^j_{\max}}$
    $j \leftarrow j + 1$
end
$\tilde{O}^* \leftarrow \tilde{O}_0$
return $\tilde{O}^*$
```

structured distortions in the raw data and solving the truncation problem of the holograms to reduce TR artifacts. All steps are shown in Fig. 4.6 and are the following.

The first step is the flat-field-correction, Sec. 3.1, which aims to remove most of the structured distortions from the raw hologram. For this purpose, a stack of empty beam images is measured and a statistical analysis with principal component analysis applied. The hologram is then normalized by a synthetic flat-field, generated from the PCA components and the measured hologram itself. A flat-field-correction is usually not sufficient to completely remove the structured distortions. For a residual global offset correction, we introduce the correction value $a_0 \in \mathbb{R}$ as a hyper-parameter.

To avoid TR artifacts, the preprocessing of Sec. 4.1.1 is applied. The flat-field corrected hologram is extended by mirroring the data along each spatial axis, into the positive and negative and also into the diagonal directions. This avoids sudden step at the hologram edges and the appearance of artificial propagation fringes, as explained in Sec. 4.1.2. To reduce the spectral leakage which results from the fast Fourier transform in the implementation of the forward model, a two dimensional window function is applied. As a window function, we choose a modified Blackman function as derived in Sec. 4.1.3. The function has been altered such that it is split into two parts and consists of a constant area in the center. The fading by the window function is thus only applied to the hologram extension and the original hologram in the center remains unchanged. The data is faded by the functional towards the hyper-parameter a_0 and then further padded by the constant a_0 until the Nyquist criterion is fulfilled. All preprocessing steps required for the raw data were already summarized in Alg. 1. The preprocessing result is then used as the input hologram for the reconstruction.

4.5.2 Minimization Problem

The ASRM is based on the original objective function Eq. 3.18 and Alg. 2, which we extend with further regularization approaches. The regularization will reduce OE artifacts while improving the reconstruction of low frequency components, effectively reducing WR artifacts. To suppress the OE artifacts, we use the regularization approach of Sec. 4.3 and extend the objective function with an L_2 regularization of the absorption value. This stabilizes the reconstruction of phase shift values.

The minimization problem is further modified to mitigate the forward model induced reconstruction bias and suppress WA artifacts as stated in Sec. 4.4. One of the properties of the forward model is the sensitivity to high spatial frequency components of the TF. This leads to a disproportionately favored reconstruction of high spatial frequencies of the reconstructed refractive indices and thus to instabilities and poor reconstruction of low spatial frequencies. To compensate for this, we introduce a multigrid method and solve the minimization problem on grids of different sizes. This controls the level of details that are reconstructed by spatial filtering, while improving the computational time of the algorithm. The grid is specified by a downsampling $S_{\downarrow}$ operator and an upsampling operator $S_{\uparrow}$, respectively.

Additionally, the new hyper-parameter a_0 of Sec. 4.1.1 and Sec. 4.2.2 is also introduced to suppress LF artifacts. There are several ways to incorporate a_0. The offset correction in the preprocessing step of the raw data has to be for example considered in the non-negative electron density constraint since an intensity offset changes the zero reference for the reconstructed absorption values. We account for that by adjusting the physical constraint Eq. 4.40.

Every introduced regularization induces a reconstruction bias and alters the reconstruction result. The bias can become significantly strong depending on the technique and used regularization weights. This can also manifest in artifacts like blurred objects introduced by Tikhonov regularization [82, 83], missing features from sparsity regularization [89, 90] or staircase artifacts from total variation regularization [79–81]. The aim of a reconstruction in NFH, however, is to correctly reconstruct the refractive indices of the measured object, not only optically but also quantitatively. This goal has not yet been achieved and is the subject of ongoing research. Nevertheless, the reconstruction bias has to be considered and should be minimized in the reconstruction result. To take this into account, the regularization scheme is mostly introduced to warm up the algorithm. The goal of this heuristic approach is to suppress the risk of artifacts, especially in the first few hundred iterations. Starting with a strong regularization, the regularization weights are successively reduced to zero over the course of the reconstruction. As the gradient becomes progressively smaller over time, the accumulation effect of the NAG also decreases, and with it the risk of artifacts due to forward-model-induced reconstruction bias and OE. During the final iterations, the minimization problem contains only physically relevant terms, in particular the data fidelity term and the non-negative electron density constraint. The warm up approach can also be interpreted as using the L_2 regularization, the multigrid approach and the modified NAG to compute a good initial guess. A good guess plays an important role in phase retrieval, because of the non-convexity of the reconstruction problem. We obtain for the cost function

$$\tilde{O}^* = S_\uparrow \left[\underset{\tilde{O}}{\operatorname{argmin}} \frac{1}{2} \left\| \left| \mathcal{D}_{\mathrm{Fr}}(\tilde{O}) \right| - \sqrt{S_\downarrow \mathcal{I}_{\mathrm{det}}} \right\|_2^2 + \mathcal{X}_{\Omega_P}(\tilde{O}) + \beta \| \mathrm{Im}(\tilde{O}) \|_2 \right], \tag{4.63}$$

under the modified non-negative electron density constraint $\Omega_P(a_0)$:

$$\Omega_P(a_0) = \left\{ \forall\, x \in \tilde{O} : \mathrm{Re}(x) \in [-\infty, 0],\ \mathrm{Im}(x) \in \left[-\log\left(\sqrt{a_0}\right), \infty\right] \right\}. \tag{4.64}$$

For the final iterations, the regularization weights of the reconstruction are reduced to zero, i.e. $\beta = 0$ and the sampling operators are set to the identity $S_\downarrow = S_\uparrow = \mathbb{1}$.

4.5.3 Solver

The solver of Eq. 4.63 is based on a PGD approach. The PGD algorithm of Sec. 3.2.2 solves a general minimization problem,

$$\tilde{O}^* = \underset{\tilde{O}}{\operatorname{argmin}}\, f(\tilde{O}) + \mathcal{X}_\Omega(\tilde{O}), \tag{4.65}$$

consisting of a differentiable function $f(\tilde{O})$, and a convex constraint set Ω with an indicator function Eq. 3.19. The algorithm solves both terms of the minimization problem in an alternating manner, using a forward-backward splitting and consists of two main steps: (i) a gradient descent to minimize the function $f(x)$ and (ii) a proximal mapping to minimize the indicator function $\mathcal{X}_{\Omega_P}(\tilde{O})$. The algorithm in Sec. 3.2.2 also uses a weak Gaussian smoothing filter applied in each iteration as a denoising method. In addition, the gradient descent is extended by a NAG. The function $f(x)$, originally consisting of the data fidelity term, is modified by the proposed regularization scheme. To ensure that the L_2 regularization of the absorption is also taken into account in the Nesterov acceleration, we integrate it in the function $f(x)$ and thus also in the gradient descent step. We define the new function $f(\tilde{O})$ as

$$f(\tilde{O}) = \frac{1}{2}\left\|\left|\mathcal{D}_{\mathrm{Fr}}(\tilde{O})\right| - \sqrt{S_{\downarrow}\mathcal{I}_{\mathrm{det}}}\right\|_2^2 + \beta\|\mathrm{Im}(\tilde{O})\|_2, \tag{4.66}$$

and calculate the gradient $\nabla f(\tilde{O})$ for the gradient descent. Since the first derivative of the L_2 term is undefined at the point zero, we introduce a separate definition for this case. The resulting $\nabla f(\tilde{O})$ is the first derivative of the data fidelity term plus the first derivative of the L_2 term on the absorption with

$$\nabla f(\tilde{O}) = -\mathrm{i} \cdot \overline{\exp\left(\mathrm{i}\tilde{O}\right)} \cdot \mathcal{D}_{\mathrm{Fr}}^{-1}\left(\mathcal{D}_{\mathrm{Fr}}(\tilde{O}) - \sqrt{S_{\downarrow}\mathcal{I}_{\mathrm{det}}} \odot \mathrm{sgn}\left(\mathcal{D}_{\mathrm{Fr}}(\tilde{O})\right)\right) + \mathcal{R}(\tilde{O}), \tag{4.67}$$

$$\mathrm{sgn}(x) = \begin{cases} 0 & \text{if } x = 0 \\ \frac{x}{|x|} & \text{else} \end{cases}, \tag{4.68}$$

$$\mathcal{R}(\tilde{O}) = \begin{cases} 0 & \text{if } \tilde{O} = 0 \\ \mathrm{i}\beta\frac{\mathrm{Im}(\tilde{O})}{\|\mathrm{Im}(\tilde{O})\|_2} & \text{else} \end{cases}. \tag{4.69}$$

Using a Nesterov acceleration in the gradient descent always carries the risk of overestimating the actual solution. Due to the forward model induced reconstruction bias, the risk mainly concerns high spatial frequencies. Since high spatial frequencies are well represented in the forward model, we are mainly interested in accelerating the reconstruction of low spatial frequencies with a high Nesterov momentum without destabilizing the reconstruction. We therefore adjust the NAG δg, using the non-uniform momentum method from Sec. 4.4.3 and obtain:

$$\nabla g(\tilde{O}_i) = \tau\nabla g(\tilde{O}_{i-1}) + \eta\nabla f(\tilde{O}_i - \tau\nabla g(\tilde{O}_{i-1})), \tag{4.70}$$

with the adjusted momentum operator τ:

$$\tau = \gamma\mathcal{F}^{-1} \circ \exp\left(-2\pi^2(k_x^2 + k_y^2)\sigma^2\right) \circ \mathcal{F}, \tag{4.71}$$

where $\gamma \in \mathbb{R}$ is a scalar weight, $\sigma \in \mathbb{R}$ is the variance of the Gaussian function, $\mathcal{F}$ is the two-dimensional Fourier transform and (k_x, k_y) are the spatial frequencies in the Fourier transform. The proximal mapping operation of the indicator function for a convex set is a projection onto this set. We have already adapted the interval limits of the set Ω_P in Sec. 4.5.2. We get the new projector $\mathcal{P}_{\Omega_P}(\tilde{O})$ with

$$\mathcal{P}_{\Omega_P}(\tilde{O}) = \min\left(0, \mathrm{Re}(\tilde{O})\right) + \mathrm{i} \cdot \max\left(-\log\left(a_0\right), \mathrm{Im}(\tilde{O})\right). \tag{4.72}$$

The complete algorithm is summarized in Alg. 5.

4.5.4 ASRM Algorithm

Algorithm 5: ASRM reconstruction of $\tilde{O}$ created from a combination of Alg. 2, Alg. 3 and Alg. 4

Input: Preprocessed measurements $\mathcal{I}_{\mathrm{cor}}$ by Alg. 1, list of update rates η for the gradient step, list of Nesterov momentum operators τ, list of L_2 regularization weights β, list of filter coefficients Ω_F, list of down- and upsampling operators $S_\downarrow, S_\uparrow$, initial values for $\tilde{O}_0$, list of maximum iterations k_{max}, parameter j_{max} is given by the list lengths

Output: Approximated solution $\tilde{O}^*$

```
$g_0 \leftarrow 0,\ j \leftarrow 0$
// Regularization levels
while $j < j_{\mathrm{max}}$ do
    $k \leftarrow 0$
    // Iterate in given level
    while $k < k^j_{\mathrm{max}}$ do
        $\tilde{O}'_k \leftarrow \mathrm{gauss}_{\Omega_F^j}\left(\mathrm{pad}_c\left(\mathrm{fade}\left(\mathrm{pad}_m\left(\tilde{O}_k\right), 0\right), 0\right)\right)$
        $y_{k+1} \leftarrow \tilde{O}'_k - \tau^j g_k$
        $g_{k+1} \leftarrow \tau^j g_k + \eta^j \nabla \left[\frac{1}{2}\left\| |\mathcal{D}_{\mathrm{Fr}}(y_{k+1})| - \sqrt{S^j_\downarrow \mathcal{I}_{\mathrm{cor}}} \right\|_2^2 + \frac{\beta^j}{\eta^j} \left\|\mathrm{Im}(()y_{k+1})\right\|_2\right]$
        $n_{k+1} \leftarrow \mathcal{P}_{\Omega_P}(\tilde{O}'_k - g_{k+1})$
        $\tilde{O}_{k+1} \leftarrow \mathrm{cutroi}(n_{k+1})$
        $k \leftarrow k + 1$
    end
    $\tilde{O}_0 \leftarrow S^j_\uparrow \tilde{O}_{k^j_{\mathrm{max}}}$
    $g_0 \leftarrow S^j_\uparrow g_{k^j_{\mathrm{max}}}$
    $j \leftarrow j + 1$
end
$\tilde{O}^* \leftarrow \tilde{O}_0$
return $\tilde{O}^*$
```

4.6 Application to experimental data

4.6.1 Comparison of algorithms

In the following, the artifact reduction methods developed in this chapter will be applied to experimental data in the form of the algorithm derived in Sec. 4.5. In order to compare the presented methods with each other, we divide the developed methods into different categories and summarize them in respective algorithms. For a comparison, we consider the following variants of the ASRM:

Alg. 2:	Reference PGD method Alg. 0 with preprocessing Alg. 1
Alg. 3:	Additional L_2 regularization for the absorption values of $\tilde{O}$
Alg. 4:	Suppression of HF
Alg. 5:	Combination of Alg. 2 to Alg. 4 $\mapsto$ ASRM

All algorithms contain the preprocessing approach Alg. 1 and the cost function extension Eq. 4.40 to suppress TR and LF artifacts. Algorithm 2 is the reference reconstruction Alg. 0 modified by prior knowledge with respect to the preprocessing. Algorithm 3 adds the L_2 regularization for the absorption values to suppress OE artifacts. Alg. 4 does not include the L_2 regularization and only integrates the suppression of the reconstruction of high spatial frequencies. This includes the multigrid method and the adaptation of the NAG to suppress WR artifacts. Algorithm 5 combines all the methods described and is the final algorithm ASRM from Sec. 4.5.
The algorithms were implemented in Python using the PyTorch library for GPU acceleration [91–93]. The reconstruction was performed on the Maxwell computing cluster at DESY on a NVIDIA A100 GPU with 40GB memory [94]. During the reconstruction, all data involved was retained on the GPU.

4.6.2 Choice of parameters

The reconstruction parameters for each sample are shown in Tab. **??** and Tab. 4.2 and were heuristically determined for the four shown objects, based on the observation of stable convergence and a visual inspection of the reconstructed phase images. All reconstruction variants are controlled by fixed iteration numbers, also to compare convergence. For the total iteration number, 2000 iterations seemed to be a good reference for showing the artifact suppressing effects of the proposed approaches. For the multigrid approaches Alg. 4 and Alg. 5, 700 iterations were chosen on the first grid, which is close to the observed overestimation peak in Fig. 4.9a of Sec. 4.3. For the up- and downsampling $S_{\uparrow}$ and $S_{\downarrow}$, respectively, a bilinear interpolation was applied, provided as part of PyTorch[92, 93]. The required downsampling factors and number of iterations were determined by trial and error, but are consistent for the presented reconstructions. Three out of the available parameters remained sample dependent and had to be tuned beforehand and for each hologram separately: (i) the variance σ of τ (Eq. 4.71) as well as the two model parameters (ii) a_0 of Sec. 4.5.1 and (iii) the optimal Fresnel number Fr of the forward model (Eq. 2.54). The regularization parameter β appeared to be in general very robust and could be chosen in the range from 0.1 to 10.

Note, that in the last 500 iterations of each algorithm variant, the proposed regularization was switched off as described in Sec. 4.5.2. This means $\beta = 0$, $\tau = \gamma$ and no downsampling. This removes the regularization induced reconstruction bias of the proposed approaches. The reconstruction result on the final iterations is then computed only on data-driven and physical constraints, i.e. the data fidelity term and the non-negative electron density constraint.

4.6.3 Analysis of reconstruction

The reconstructions should be evaluated with regard to the quality of the final result and the suppression of artifacts according to the following aspects. (i) The interior of the object, which is usually the thickest part of the measured object, should be sufficiently reconstructed. At the same time, (ii) the edges of the object should be sharply reconstructed, while (iii) the noise in the object-free area should remain small. We divide the remaining artifacts after reconstruction into the following categories:

TR:	Truncation artifacts	(Sec. 4.1)
LF:	Low frequency artifacts	(Sec. 4.2)
OE:	Overestimation artifacts	(Sec. 4.3)
WR:	Weak reconstruction artifacts	(Sec. 4.4)

4.6.4 Experimental Data Acquisition

Four datasets were obtained at the beamline P05 at PETRA III, which is located at DESY in Hamburg and operated by Helmholtz-Zentrum Hereon [8, 64, 65]. The data was obtained using the FZP-based setup for NFH as described in Sec. 2.2 and Sec. 3.3. For the demonstration of the artifact suppressing method, the following samples were measured: A spider attachment hair (Fig. 4.14)[66–68], the tip of a cactus needle (Fig. 4.15), a sample of a human tooth prepared by focused ion beam milling (Fig. 4.16) and a partly corroded biodegradable magnesium-based wire (Fig. 4.17)[23, 69, 70, 95]. The measurement parameters for each of the samples are shown in Tab. 3.1. These test objects are a good reference due to their interaction strength with X rays. The projected indices, i.e. the phase shift and the absorption, increase step by step in the above-mentioned object sequence. The decisive factor here was to cover objects that lead to several phase-wraps in the reconstruction.

The raw data was prepared for the reconstruction using the method described in Sec. 4.5.1 (Alg. 1). For the component analysis of the flat-field-correction, 50 empty images were used and the first 30 components of a principal component analysis (PCA) were selected. The data was then reconstructed using the methods described above.

	FWHM for σ in τ at Downsampling				
	16×	4×	2×	1×	a_0
Spider hair	16	8	64	-	0.98
Cactus needle	16	8	64	-	0.98
Tooth	16	8	64	-	0.96
Magnesium-based wire	4	8	32	-	1.1

Table 4.1: Sample dependent parameters. Values of σ in τ given as full width at half magnitude (FWHM) in pixels. σ can be derived by calculating $\sigma = FWHM/2.35$. Value a_0 for fading, padding and Ω_P.

Panel	Iterations	U Down-sampling	η Update Rate	γ Momentum	β L_2 Weight	Filter $\tilde{O}$
Alg. 2	2000	-	1.1	0.99	-	2.0 / 8.0
Alg. 3	1500	-	1.1	0.99	10.0	2.0 / 8.0
	500	-	1.1	0.99	-	2.0 / 8.0
Alg. 4	700	16×	1.1	1.0	-	2.0 / 0.0
	300	4×	1.1	1.0	-	2.0 / 8.0
	500	2×	1.1	1.0	-	2.0 / 8.0
	500	-	1.1	1.0	-	2.0 / 8.0
Alg. 5	700	16×	1.1	1.0	10.0	2.0 / 0.0
	300	4×	1.1	1.0	1.0	2.0 / 8.0
	500	2×	1.1	1.0	0.1	2.0 / 8.0
	500	-	1.1	1.0	-	2.0 / 8.0

Table 4.2: Setup and sample independent reconstruction parameters for algorithms 2 to 5 that were used to generate results in Figs. 4.14 to 4.17. The filter $\tilde{O}$ values are given in Full Width at Half Magnitude (FWHM) for real and imaginary parts in form of $\mathrm{FWHM}_{\mathrm{real}}/\mathrm{FWHM}_{\mathrm{imag}}$.

Sample	Alg. 2			Alg. 3			Alg. 4			Alg. 5		
	LF	OE	WR	LF	OE	WR	LF	OE	WR	LF	OE	WR
Spider hair	X	X	↓	X	↓	↓	X	↓	↓	↓	↓	↓
Cactus needle	X	↓	X	X	↓	X	X	↓	↓	↓	↓	↓
Tooth	X	↓	X	X	↓	X	↓	↓	X	↓	↓	↓
Magnesium-based wire	X	X	X	X	X	X	↓	↓	X	↓	↓	↓

Table 4.3: Reconstruction artifacts that are present in the respective result panels of Figs. 4.14 to 4.17. The TR artifacts issue was already resolved by preprocessing and is left out in this table. The abbreviations under the algorithm numbers correspond to the respective artifact types. An arrow downwards ↓ indicates a significant suppression of the artifact, an X indicates that the artifact is visibly present.

4.6.5 Results

The resulting figures are shown in Figs. 4.14 to 4.18 and have all the same structure. Each of the figures shows the reconstruction results of the phase shift of the four algorithm variants as stated in the corresponding panel. In addition, a one-dimensional plot of a horizontal cross-section per result is shown in the bottom panel. The position of the cross-section is marked as a dashed line in the panel of the standard reconstruction.

For all samples and every algorithm variant, TR artifacts are significantly less visible in the reconstruction results. The remaining artifacts are, depending on the algorithm variants, LF, OE and WR that we summarized into Tab. 4.3, where we compared the different samples for the algorithm variants and occurring artifacts.

The proposed algorithm variants perform as follows:

Algorithm 2, the basic algorithm, yields the worst results in all cases. It failed to reconstruct the object's interior of the cactus needle, the tooth and the magnesium-based wire. The results of the spider hair and the magnesium-based wire possess clearly visible OE artifacts. Also, LF artifacts are very prominent.

Algorithm 3 reduced the OE artifacts of Alg. 2 that were visible in the spider hair and magnesium-based wire results. The algorithm still failed to completely reconstruct the object's interior of the cactus needle, the tooth and the magnesium-based wire. The results also suffer from LF artifacts, either in form of a static offset for the spider hair or background variations for the cactus needle, tooth and magnesium-based wire.

Algorithm 4 significantly suppressed all OE artifacts of Alg. 2. Compared to Alg. 3, the algorithm also improved the background variations as well as the reconstruction of the object's interior. For the cactus needle, the algorithm succeeded to suppress artifacts in the reconstructed phase image and almost reconstructed the object's interior of the tooth.

Algorithm 5 offers the best reconstruction quality if compared to the other approaches. The combination of both approaches significantly reduced LF and OE artifacts. The

		Computation Time / s			
Sample	Array Size / px	Alg. 2	Alg. 3	Alg. 4	Alg. 5
Spider hair	14336 × 14336	465	528	158	160
Cactus needle	14336 × 14336				
Tooth	8192 × 8192	136	142	47	43
Magnesium-based wire	8192 × 8192				

Table 4.4: The total computation time depends on the required sampling rate for the Fresnel propagation kernel and the grid sizes of the multigrid approach. The array size for the reconstruction and the computation time is shown in this table. The computation time was determined by an average of 20 reconstructions without initialization overhead and intermediate plots.

algorithm also succeeded in the reconstruction of the object's interior for all tested objects.

The magnesium-based wire is the only sample with considerable absorption. The reconstruction result of the absorption is shown in Fig. 4.18. Similar to the phase reconstruction, the presence of the OE artifacts decreased gradually in the order Alg. 2, Alg. 3 and Alg. 4. While the artifact suppression effect is already visible in Alg. 3 the strongest artifact suppression effect had the multigrid approach Alg. 4 and the combination with Alg. 3 leads to no improvement in the absorption (Alg. 5).

The computation times for each algorithm variant are shown in Tab. 4.4 and are an average of 20 reconstructions, performed on a GPU as described in Sec. 4.6.1.

Due to the different Fresnel numbers of the forward model, the required sampling rate and therefore array size were object dependent. The maximum computation time for the largest array size was 8 min 48 sec (spider hair, cactus needle) with Alg. 3. The fastest reconstruction was performed in 43 sec with Alg. 5 (tooth sample). Independent of the array size, the computation time could be reduced to 1/3 by the multigrid approach of algorithm variants Alg. 4 and the ASRM method Alg. 5.

Further information of the behaviour of the algorithm variants can be extracted from the evolution of the mean squared error (MSE) in Fig. 4.19 and Fig. 4.20. Here also the variant of Alg. 2 without a Nesterov is shown for comparison. The MSE is only calculated inside of the ROI and the hologram extension ignored. The MSE describes how well the reconstructed solution explains the input data. The algorithm variant Alg. 2 yielded the worst result in all cases. It can be seen that each approach improved the reconstruction with respect to the MSE. The multigrid approach of algorithm variants Alg. 4 and the ASRM method Alg. 5 both improved the MSE by multiple orders of magnitude. The combination of all approaches into the ASRM method yielded the best results for the spider hair, the cactus needle and the tooth sample. For the magnesium-based wire sample, the MSE result of the ASRM method was comparible to Alg. 4.

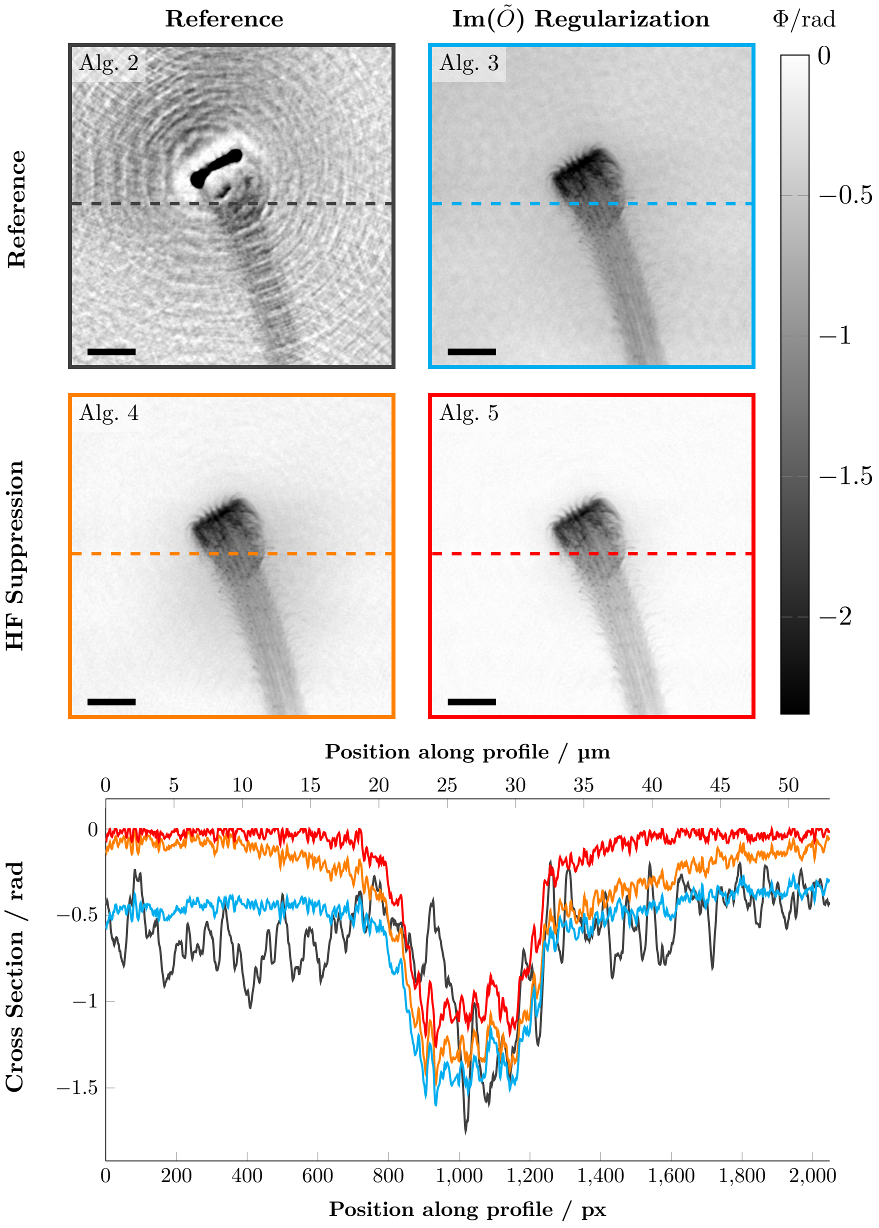

Figure 4.14: Spider hair. The result of Alg. 2 shows a clearly visible OE artifact in the dense area in the middle that emits fringes into the background. The object itself is optically well reconstructed in panels of Alg. 3 and Alg. 4. However, both approaches still show LF artifacts across the whole phase image. The panel of Alg. 5 shows the best reconstruction. The dashed line indicates the position of the cross section. The scale bar indicates 8 µm.

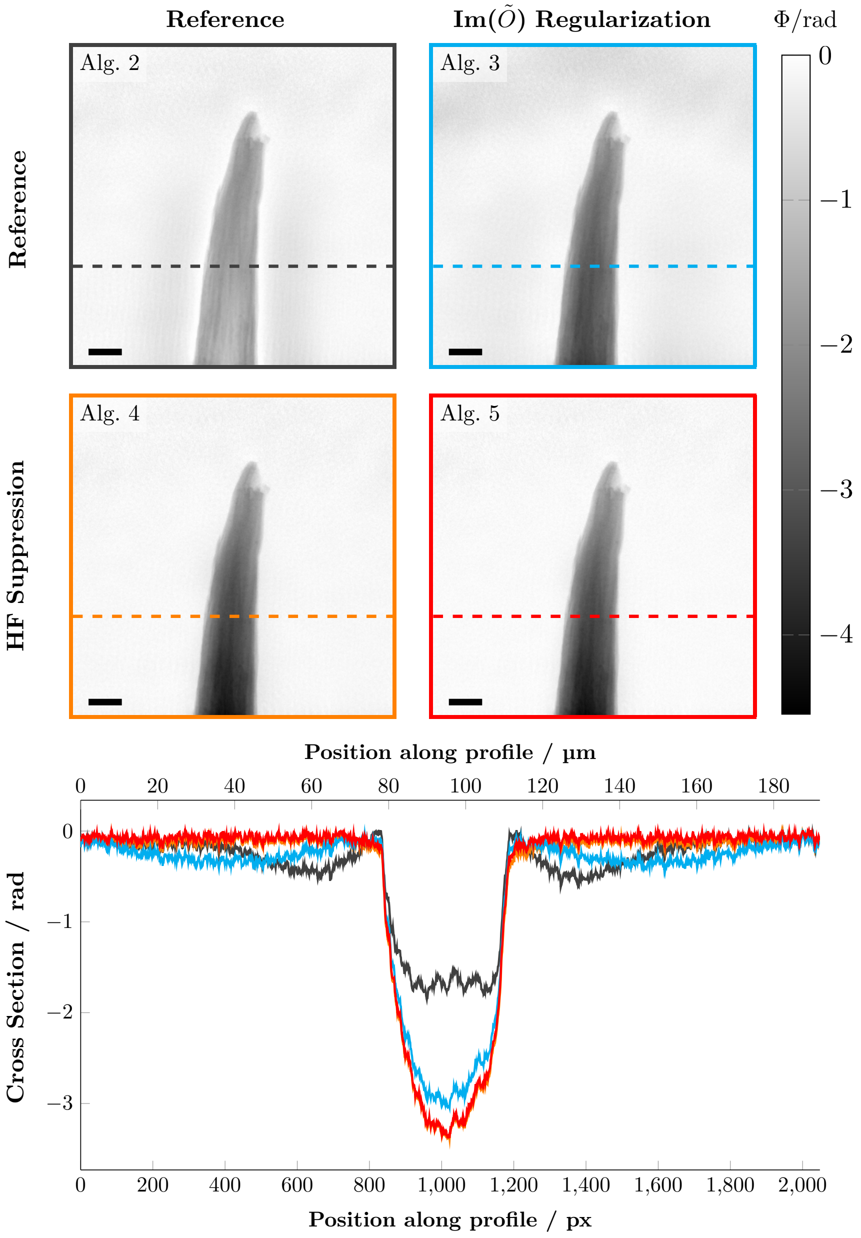

Figure 4.15: Cactus needle. The algorithm Alg. 2 has not completely reconstructed the object's interior. In the background around the object are some LF variations visible. The panel of Alg. 3 offers a better phase reconstruction but suffers from LF artifacts in the top area and LF variations in the background. The panel of Alg. 4 and Alg. 5 reconstructed the object almost identical, with significantly reduced LF variations. The dashed line indicates the position of the cross section. The scale bar indicates 20 µm.

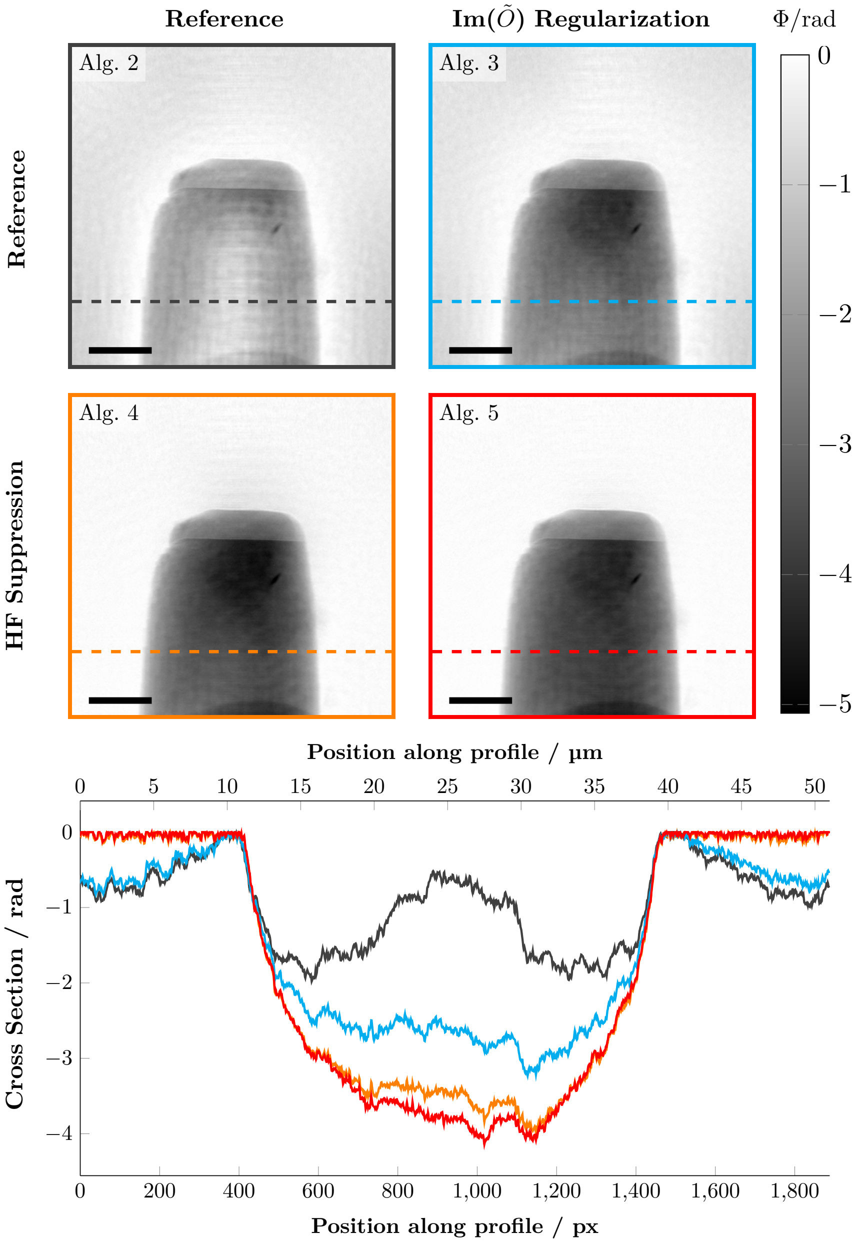

Figure 4.16: Tooth. The algorithms Alg. 2 and Alg. 3 have not completely reconstructed the object's interior. In the background are some LF variations visible. In the cross section, the error increases towards the image border. Alg. 4 and Alg. 5 significantly reduce the LF variation in the cross section. Alg. 5 posses the highest rate of maximum reconstructed phase shift to noise in the object free area. The dashed line indicates the position of the cross section. The visible dense structure at the bottom of the image belongs to the sample and is Gallium from a focused ion beam. The scale bar indicates 10 µm.

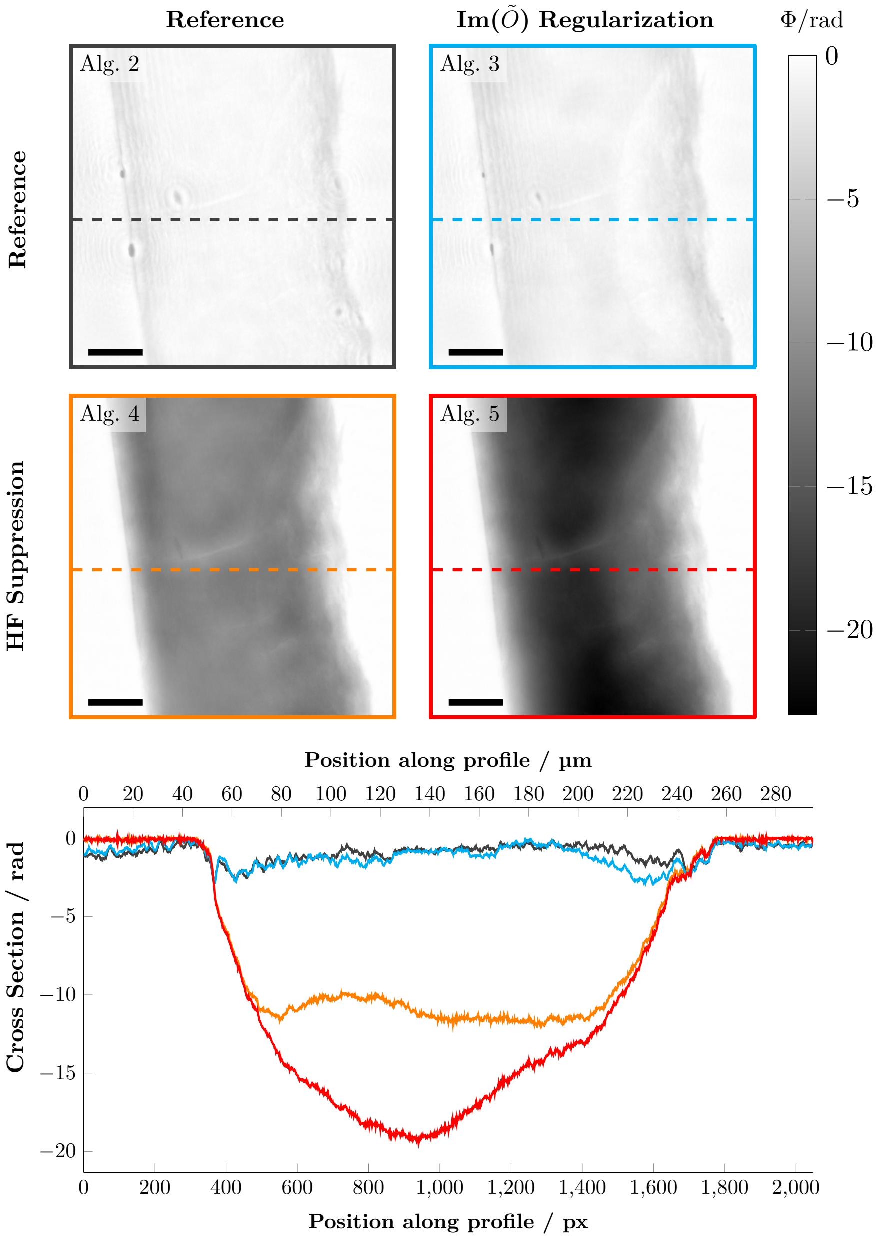

Figure 4.17: Magnesium-based wire. Here, the effects of the regularization techniques are particularly visible. The quality of reconstructed phase values increases gradually in the panel order Alg. 2, Alg. 3, Alg. 4, Alg. 5. Alg. 3 reduced the OE artifacts of Alg. 2, especially in the right area of the object but was unable to reconstruct the object's interior. The result of Alg. 4 is free of OE artifacts but the object's interior is still not completely reconstructed. Only the combination of all approaches, Alg. 5, yields a well reconstructed phase image with the completely reconstructed object's interior and significantly reduced artifacts. The dashed line indicates the position of the cross section. The scale bar indicates 50 µm.

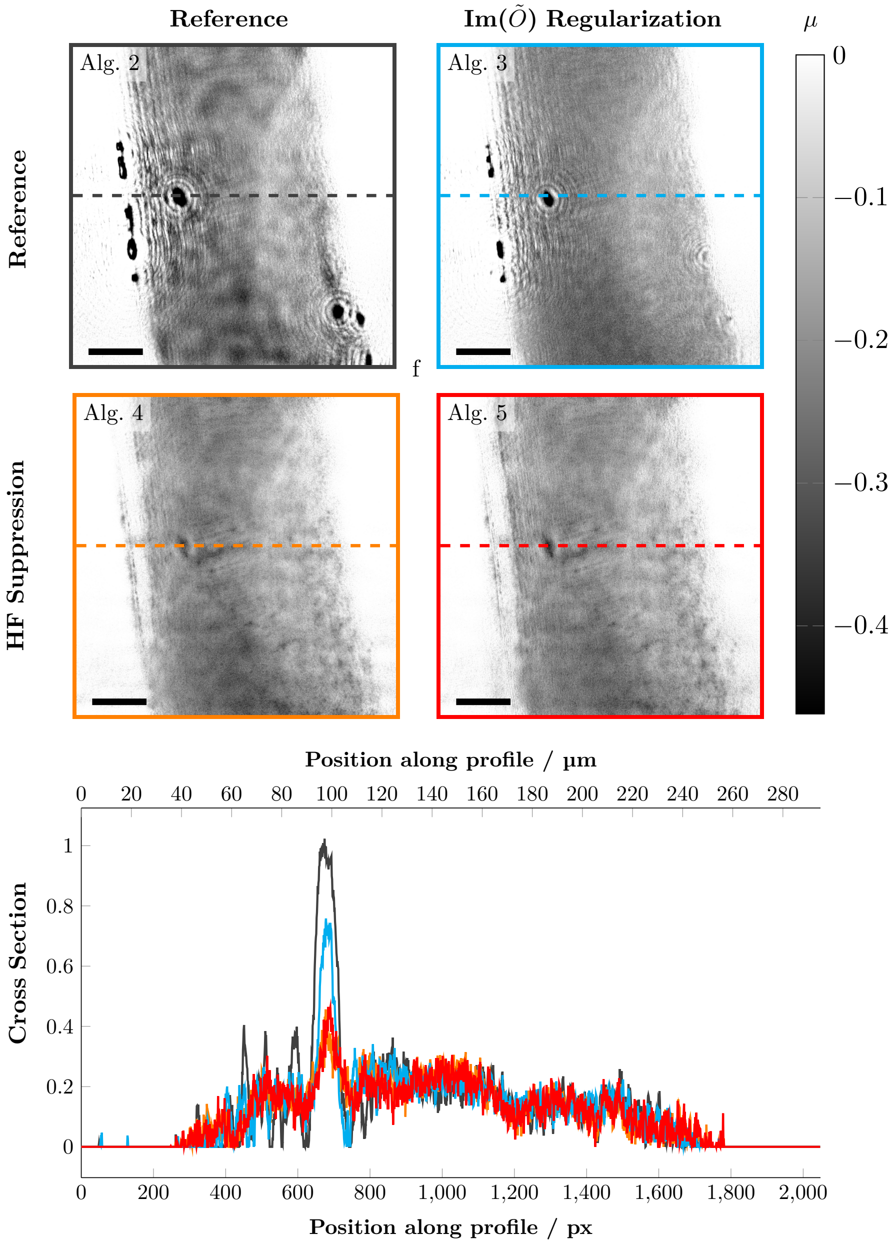

Figure 4.18: Reconstructed absorption for the magnesium-based wire. The dashed line indicates the position of the cross section and was positioned at the most prominent OE artifact. The presence of the OE artifact decreases gradually in the panel order Alg. 2, Alg. 3 and Alg. 4. Left and right from the artifact, fringes in Alg. 2 and Alg. 3 appear where the absorption is partly reconstructed as zero. The fringes and the overestimation in the absorption disappear with Alg. 4. In the combined variant Alg. 5, the cross section is almost equal to the cross section of Alg. 4. The scale bar indicates 50 µm.

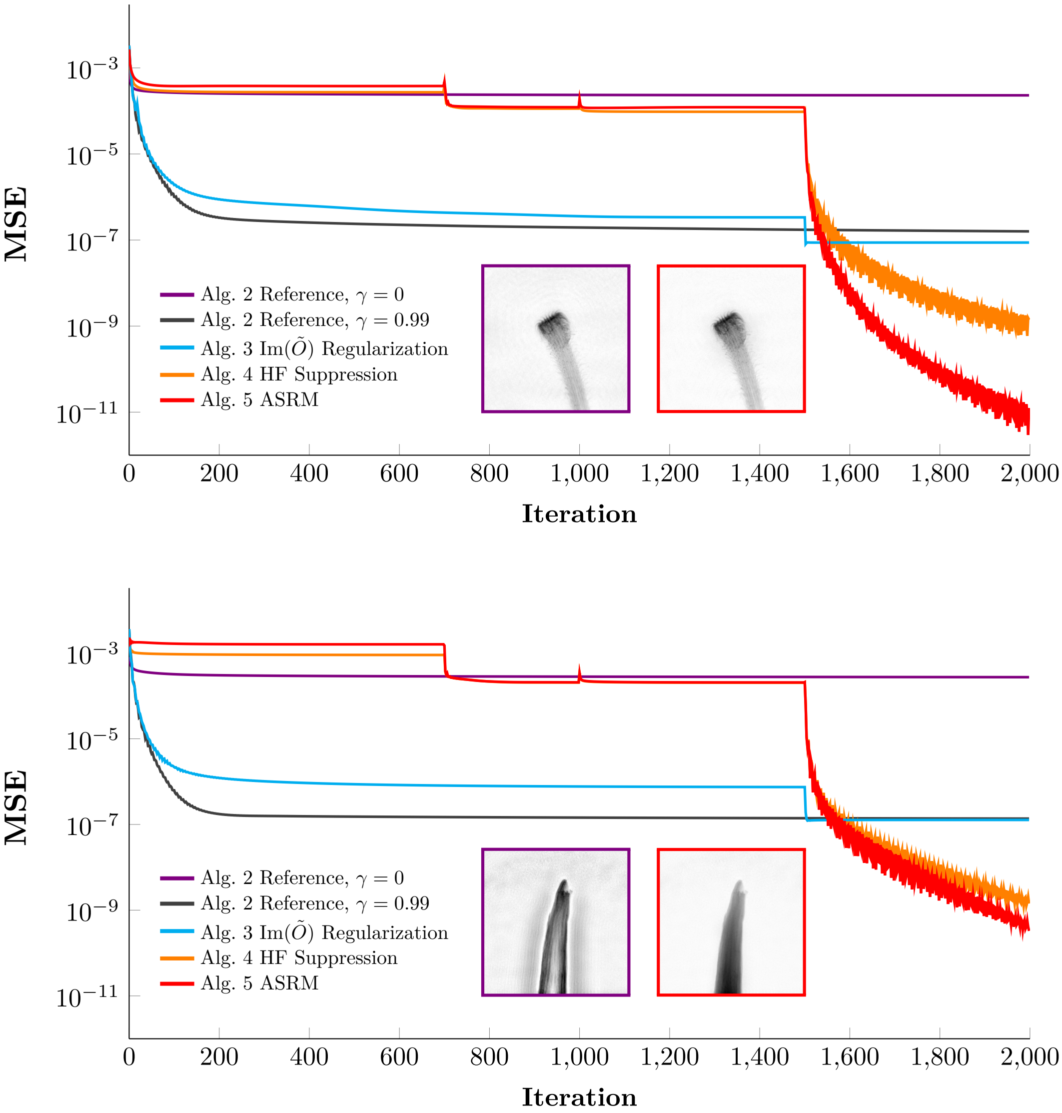

Figure 4.19: Progress of the target function for the spider hair and the cactus needle samples. The graphs show the mean squared error (MSE) of the data fidelity, i.e $1/N \cdot \| |\mathcal{D}_{\mathrm{Fr}}(\tilde{O})| - \sqrt{\mathcal{I}_{\mathrm{det}}} \|_2$, for each algorithm as a mean value over all pixel inside the ROI, plotted against the number of iterations.

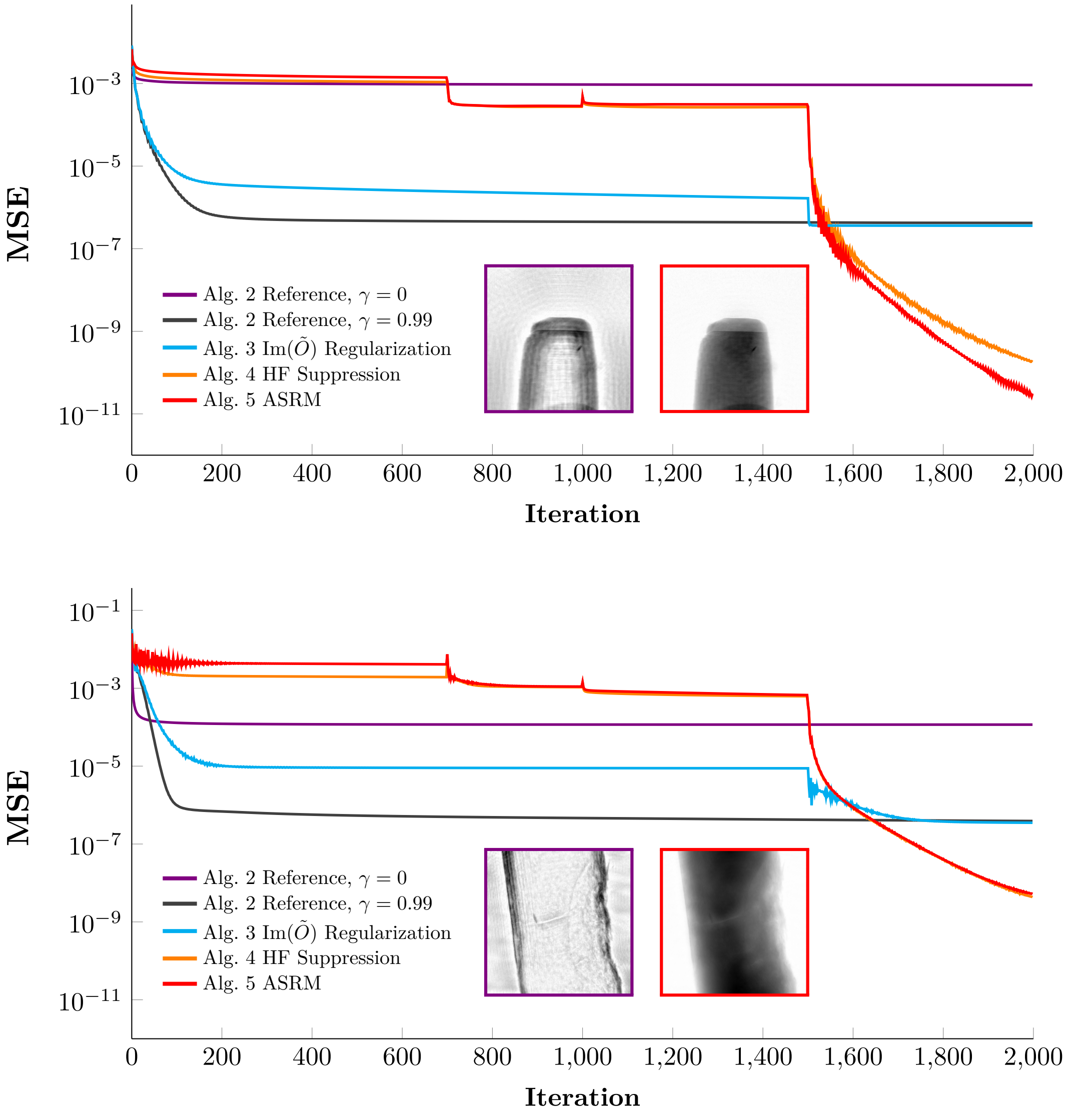

Figure 4.20: Progress of the target function for the tooth and magnesium-based wire samples. The graphs show the mean squared error (MSE) of the data fidelity, i.e $1/N \cdot \|\left|\mathcal{D}_{\mathrm{Fr}}(\tilde{O})\right| - \sqrt{\mathcal{I}_{\mathrm{det}}}\|_2$, for each algorithm as a mean value over all pixel inside the ROI, plotted against the number of iterations.

4.7 Discussion and Outlook

In this chapter, we investigated reconstruction artifacts that occur for reconstructions with the PGD-based reconstruction algorithm of Sec. 3.2.2, if common used measurement and regularization techniques are abandoned. This includes measurements in multiple distances, employing a spatial support constraint, constraints based on the δ/β relationship and computationally intensive regularization such as total variation.
In Sec. 4.6, we tested our approaches with experimental data that was measured at the beamline P05 at PETRA III, located at DESY in Hamburg. The objects covered interaction strengths from weakly interacting samples which do not exceed phase shifts of π rad to multi material samples that have a phase range beyond 6π rad. The problem of appearing phase-wraps that many algorithms have was not an issue for neither of the algorithm variants. In general, each of the approaches show quality improvements when compared to the PGD algorithm of Sec. 3.2.2:

- (i) The preprocessing scheme successfully suppressed TR artifacts.
- (ii) The correction of the offset of the FFC in Sec. 4.2 removed LF artifacts.
- (iii) The L_2 regularization of the absorption values in Sec. 4.3 reduced significantly OE artifacts and offered an improved reconstruction of the object envelope for three of four objects.
- (iv) The HF suppression method in Sec. 4.4 resulted in strong improvements with respect to OE and WR artifacts.

In comparison, the HF suppression method (iv) resulted in the best improvements of the reconstruction quality, in all examples. No OE artifacts were visible as well as previously weakly reconstructed areas, i.e. WR artifacts, improved. For two of four objects only applying (iv) was still not successful to reconstruct the complete object envelope. Only the combination of all approaches, successfully suppressed artifacts in all cases with a good reconstructed object envelope. This resulted in the ASRM algorithm.
With a multigrid reconstruction approach, we were able to decrease the computation time. In particular by 1/3 for 2000 iterations and the tested data. The evolution of the MSE values for each algorithm variant showed that the reconstructed results were not only visually improved in terms of visible artifacts, but also represent objects that better explain the measured holograms. Especially the issue of the forward model reconstruction bias could be well observed in the MSE curves of the magnesium-based wire. Although significantly different in the horizontal profile, the results of (iv) and ASRM converged to almost identical MSE values. The difference between the two reconstructed results is the reconstructed object envelope, which consists mostly of low spatial frequencies and indicates their weak contribution to the cost function.
The developed ASRM algorithm should be further improved in future work. Two object dependent parameters, σ for the NAG weights and the constant value a_0 of the preprocessing and modified non-negative electron density constraint had to be tuned manually. It should be investigated in the future how both parameters could be optimized

automatically. It is still unclear what features in the measured hologram influence the σ value. Also, a Gaussian function for τ of the NAG may not be optimal. The optimization problem of the a_0 value is similar to the problem of the Fresnel number optimization, which is discussed in the next chapter and could be adapted. One important issue here is to find good metric for the optimization. In Sec. 4.2.2, it is suggested that the MSE of the cost function could be used but it is still not sufficiently examined. The ASRM should also be tested under different scenarios, beamline and optics. Especially the reconstruction of objects that exceed the detectors FOV at all borders are relevant for many experiments. For those type of objects, the global phaseshift problem needs to be solved. Other beamlines use different optics, which should be tested. Waveguides-based experiments at the P10 GINIX endstation at DESY in Hamburg and CRL-based experiments with a phase-plate at the free-electron laser XFEL in Hamburg Schenefeld were already performed and seemed promising.

5

A Solution to the Autofocus Problem

In this chapter, an algorithm to autofocus (AF) the reconstructed images in NFH is developed. The chapter is based on the publication [39]. The problem of focusing images is commonly known from photography where an analog or a digital camera automatically adjusts the imaging geometry of the lens system such that a sharp image is recorded. The AF in a camera can be performed with the help of additional hardware, for example by adding extra sensors that measure the distance between objective and captured object. However, additional hardware is not always desired or available. In such cases, the AF must be performed numerically, using an approach that makes adjustments based solely on a captured image. For the reconstruction of holographic data, the numerical focus is part of the applied forward model and needs to be known very precisely. This problem has already been studied in the literature, especially in the field of optical microscopy with coherent light probes [96–100]. In NFH, the Fresnel number of the forward model, which was introduced in Sec. 2.3, is required for the reconstruction. The Fresnel number summarizes the most important parameters of the measurement setup into a scalar, including the wavelength of the X-ray beam, the pixel size of the detector and the distances between the focus, sample and detector. For the reconstruction of sharp images of the measured objects, the parameters of the measurement setup must be known very precisely. If these parameters are inaccurately embedded in the forward model of the reconstruction algorithm, it will generate artifacts or result in blurred reconstructed images. In practice, it is often difficult to determine the Fresnel number accurately for a good reconstruction. The reasons for this can be inaccurate hardware components as well as inaccurate or missing measurements to determine the geometry of the measurement setup. In such cases, the fine-tuning of the Fresnel number has to be done in a complex post-processing step, e.g. by reconstructing an image series, a manual method where the correct Fresnel number is determined according to optical, subjective criteria. However, due to the increasing memory demand for measured data, it is becoming increasingly difficult to maintain a sufficient throughput of reconstruction data, manual processing steps have to be gradually reduced. The demand for fast reconstruction algorithms increases, making AF a necessity. This is especially true for *in-situ/operando* studies. However, the available AF studies have been carried out under constraints, either for the object or for the reconstruction algorithms. In particular, the dependence of available focus criteria on optically good reconstructions that are mutually consistent over variations of the numerical focus is a difficult requirement. The reconstruction of objects from the near-field holographic data is in itself very challenging and images can be distorted by artifacts or noise as shown in Ch. 4. It is therefore desirable to develop a criterion that does not require optical analysis of the reconstructed images. Furthermore, a fully automated algorithm suitable for *in-situ* experiments is needed to minimize manual intervention in the optimization of reconstruction parameters and thus save time.

In this chapter, we study the combination of different focus criteria in the context of reconstructions with a projected gradient descent based algorithm as described in Sec. 3.2.2, extended by the approaches of Ch. 4. We further develop a novel focus criterion for NFH, which is able to identify the correct position of the numerical focus in the reconstruction. Finally, the focus criterion is embedded into a common AF framework and robust reconstruction parameters are determined. We evaluate the algorithm and our criterion against criteria from the currently available literature. The chapter concludes with a study of simulated and experimental data.

5.1 Defocus Blurring

We now assume a measurement setup according to Fig. 2.3 of Ch. 3 with focusing optics such that the measured object is illuminated with a cone beam. Part of the calculation of the Fresnel number are the respective distances from the focal point of the optic to the object (z_{01}) and to the detector (z_{02}). These two distances are required to convert the cone beam into an equivalent parallel beam, which then has the effective propagation distance z_{eff}. This distance is calculated by the Fresnel scaling theorem [42] with

$$z_{\text{eff}} = \frac{z_{02}}{z_{01}}(z_{02} - z_{01}). \tag{5.1}$$

In the following, we investigate the error propagation of a small deviation of the respective parameters and introduce a deviation Δ_{01} for the value z_{01} and a deviation Δ_{02} for the value z_{02}. We get a new effective distance $\hat{z}_{\text{eff}}$ which is z_{eff}, perturbed by Δ_{eff}^{0x} and for both perturbations respectively

$$\hat{z}_{\text{eff}} = z_{\text{eff}} + \Delta_{\text{eff}}^{01} + \Delta_{\text{eff}}^{02} = \frac{z_{02} + \Delta_{02}}{z_{01} + \Delta_{01}}(z_{02} - z_{01} + \Delta_{02} - \Delta_{01}) \tag{5.2}$$

$$\tag{5.3}$$

For the error analysis of the effective propagation distance, we assume that both distances can be measured up to an uncertainty of ±5 mm. The correct distances are 10 cm for the focus-object distance z_{01} and 20 m for the focus-detector distance z_{02}. To compare how such an inaccuracy affects the effective propagation distance in this setup, we define the normalized error function f as

$$f := \left| \frac{\hat{z}_{\text{eff}}}{z_{\text{eff}}} - 1 \right|, \tag{5.4}$$

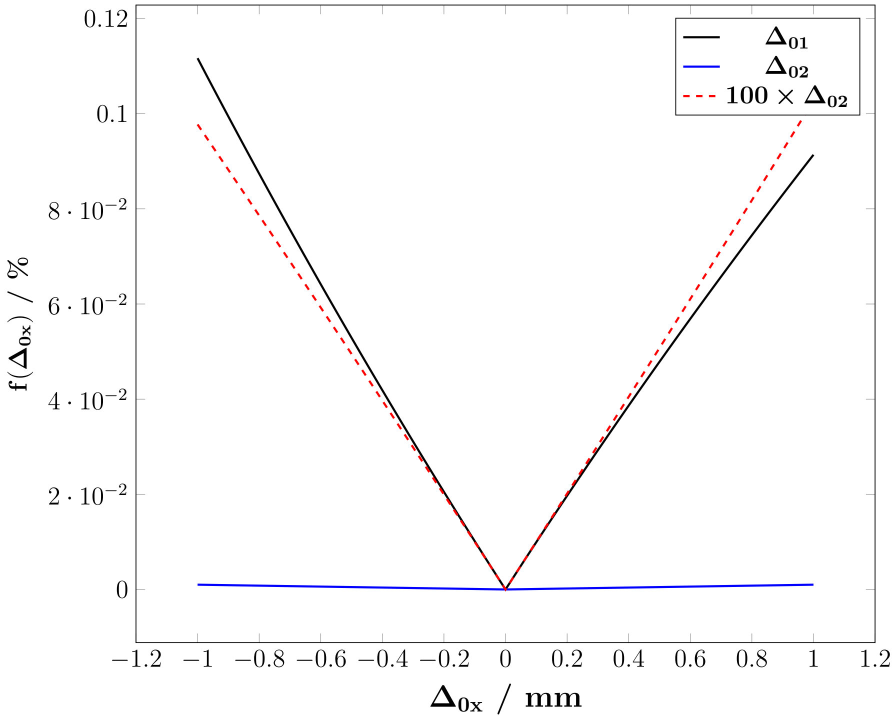

Figure 5.1: This plot shows the impact of inaccurate measurements on the effective propagation distance when the equivalent parallel beam of the cone beam setup is calculated by the Fresnel scaling theorem. The x-axis shows the measurement aberration from the real value in millimeters. The y-axis shows the aberration of the effective distance that has been normalized by the correct value. The calculation was done with an assumed measurement setup of $z_{01} = 10\,\mathrm{cm}$ and $z_{02} = 20\,\mathrm{m}$. It can be observed, that the impact of inaccurate measurements of the z_{01} value (black curve) is by some orders higher then the same inaccuracy in the z_{02} values (blue curve). They differ by a factor of 100. For comparison a 100 times larger inaccuracy is shown in the dashed red curve.

which expresses the deviation in percentage. We then create two plots, parameterized with $f(\Delta_{\mathrm{eff}}^{01})$ and $f(\Delta_{\mathrm{eff}}^{02})$. The deviations obtained for the effective propagation distance over the measurement uncertainty in percentage are plotted in Fig. 5.1.

This emphasizes the robustness of the larger distance z_{02} to small variations while the smaller distance z_{01} is very sensitive. A small error in the estimation of z_{01} has a much greater effect on the effective distance than the same deviation in z_{01}. For comparison, the measurement inaccuracy of z_{02} in this example has to be 100 times greater than z_{01} to achieve the same deviation of z_{eff}.

High accuracy of the estimation is necessary to reconstruct sharp phase or absorption images of the reconstructed object. Fig. 5.2 demonstrates the impact on the reconstruction result with respect to the assumed measurement uncertainty. Here, the phase shifting part of the reconstructed refractive object is shown. An uncertainty in the range of

±5 mm results in a blurry reconstruction and produces fringes in the image. The fringes result from an inaccurate back-propagation of the hologram with known phases by the Fresnel propagator which still leaves a residual hologram in the reconstruction result.

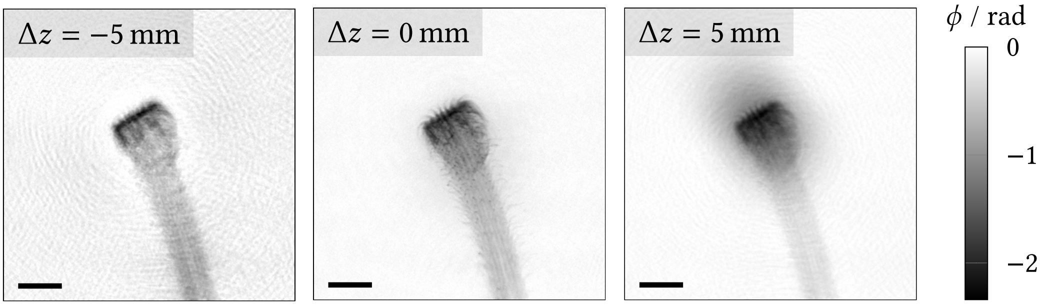

Figure 5.2: Reconstructed phase images of a spider attachment hair for distortions of the focus-object distance z_{01} of the forward model (Fig. 2.3): deviation of −5 mm (left) correct distance (middle) deviation of +5 mm (right). The scale bars indicate 8 µm. An inaccurate measurement of the z_{01} distance results in blurring and in the appearance of Fresnel fringes in the reconstruction result. The reconstruction can also become unstable or produces artifacts like the low-frequency nebular artifact in the center of (right).

To prevent blurring and the occurrence of fringes in the reconstruction result, a strategy is necessary to refine the focus-object distance from only a single hologram.

One possibility to determine a more accurate value is by applying several different focus-sample distances to the reconstruction and to pick the result which is the visually the most appealing. Visually appealing in the sense of sharpness where a human eye selects the sharpest image from a bunch of multiple hundreds of reconstructions. However, this approach requires a large time investment of a scientist and a high demand of computational resources, which renders this method unpractical for certain applications. In case of *in-situ* and *operando* measurements for example, the available timeframe where calculations can be performed is limited. We therefore seek a method that is capable of automatically finding the focus-sample distance z_{01} for all kinds of measured objects under *in-situ* conditions.

To develop an automatic algorithm for focusing, we use the following approach. We split the AF problem into three parts. First, the creation of an inverse problem which contains a loss metric to be optimized. Second, the reconstruction of the complex refractive object under a specified z_{01} as an input for the respective loss metric. Third, the implementation of a solver for the combined inverse problem.

5.2 Model Fit Error (MFE) Criterion

For the creation of a loss metric, a method has to be found to quantify the defocus error. The goal is to find a mathematical function that maps the reconstructed complex refractive indices to the distance from the correct numerical focus, a so-called focus criterion. A focus criterion should fulfill the following conditions:

- (i) The focus criterion should be a function $f : \mathbb{C}^N \mapsto \mathbb{R}$, which maps a reconstruction result, i.e. a complex-valued input image, to a scalar. The input image is a reconstruction that was parameterized with z_{01}.
- (ii) The function should have an extremum, at the correct z_{01}
- (iii) The function extremum direction, maximum or minimum, should be consistently the same for every possible object and measurement setup.
- (iv) The curve generated by the function f with a variation of z_{01} should approach the extrema as uniformly as possible in the range of the measurement uncertainty. It should have no local extrema or jumps.

The most challenging task is to find a criterion that reliably fulfills the above-mentioned conditions over a wide range of different measurement setups and types of measured objects. In the following, a new focus criterion is proposed that takes the measurement system into account from which the reconstruction results were obtained. The system includes the reconstruction model, the forward problem and the recorded hologram. The core idea here is to combine Fresnel free-space propagation with the non-negativity constraint, just as in the reconstruction algorithm for refractive reconstruction, and works as follows:

The non-negativity constraint defines a solution set Ω_P for physically valid refractive indices. We consider an object that is located in the correct focal plane at position z_{01}. If the exit wave of the object is propagated out of the focal plane with the Fresnel propagator, fringes appear in the phase and absorption images. These fringes contain nonphysical values in the sense of Ω_P. These are positive phase shifts or negative absorption values. By a projection with the operator P_{Ω_P} onto this set, the nonphysical values are removed from the propagated wave-field. This erases information from the wave-field and makes the data inconsistent. The quantity of the inconsistency increases with the propagation distance from the correct focal plane. The inconsistency can be quantified by calculating the MSE between the propagated and projected wave-field and the measurement data. If we summarize the associated operations, we obtain an error metric as a function, which minimum is at the location of the correct distance z_{01}. The metric is derived in the following: We start with a simulation under ideal conditions and assume that all values are known as ground truth. This includes

- Distance between the focus of the optics and the measured object z_{01}.
- Distance between measured object and detector z_{12}.
- The exit wave-field ψ_{exit} behind the measured object.
- The noise-free measured hologram at the detector $\mathcal{I}_{\text{det}}$.

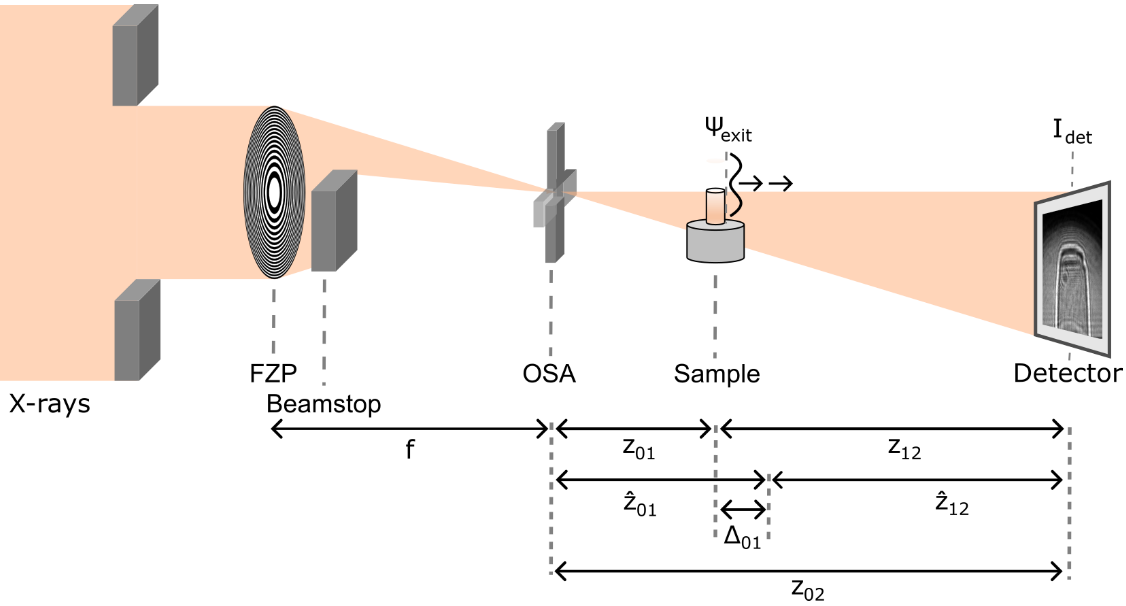

Figure 5.3: Visualization of the setup of sketch Fig. 2.3 with disturbance in the distance z_{01}. The image has been adapted from [46]. The distances are measured from the focal point of the optics. The distance of the detector z_{02} is assumed to be known. A hologram $\mathcal{I}_{\mathrm{det}}$ in this setup is the squared magnitude of the propagated exit wave-field ψ_{exit} by a distance z_{12} to the detector. A disturbance Δ_{01} in z_{01}yields new values for the distances, $\hat{z}_{01}$ and $\hat{z}_{12}$. It changes the cone-geometry of the forward-model and the effective propagation distance in the equivalent parallel beam.

The parameters are visualized in Fig. 5.3. In this setup, we assume that a refractive object was examined. The object was illuminated with a coherent, monochromatic wave-field of amplitude one and a hologram was acquired, which is described by the forward-model Eq. 2.55.

The forward model is now disturbed in the value z_{01} by an imperfect measurement and the real distance between the focus of the optics and the examined object z_{01} is therefore unknown. The disturbance can be expressed in such a way that we have measured an estimate $\hat{z}_{01}$ instead of the correct distance. This results from the actual distance z_{01} and a further defocus distance Δ_{01}, which are added together. This gives us the measured estimate for the distance between focal point and object

$$\hat{z}_{01} = z_{01} + \Delta_{01} \tag{5.5}$$

and for the distance from the object to the detector

$$\hat{z}_{12} = z_{12} - \Delta_{01}. \tag{5.6}$$

Due to the deviation Δ_{01}, the known wave-field is also defocused, which we express by propagating the exit wave-field by the distance Δ_{01}. To do this, we use a propagation operator, $\mathcal{D}_{\mathrm{Fr}}(\psi)$, which has a wave-field ψ as an argument instead of the refractive object $\tilde{O}$. The conversion is trivial with $\psi = \exp(\mathrm{i}\tilde{O})$ and we use both operators synonymously in the following. We obtain a propagated wave-field $\hat{\psi}$ to the distance Δ_{01} with:

$$\hat{\psi} = \mathcal{D}_{\mathrm{Fr}}^{\Delta_{01}}(\psi_{\mathrm{exit}}). \tag{5.7}$$

We assume that instead of z_{01} and z_{12} and ψ_{exit}, only the deviating values $\hat{z}_{01}$, $\hat{z}_{12}$ and $\hat{\psi}$ are known. We now want to use a measured hologram $\mathcal{I}_{\mathrm{det}}$ to quantify the deviation Δ_{01} and thereby determine the correct focus-object distance z_{01}. To do this, we take the approach described above and first project the known wave-field onto the solution set P_{Ω_P} defined by the non-negative electron constraint Ω_P. We thus obtain a projected wave-field $\hat{\psi}_P$ by

$$\hat{\psi}_P = \mathcal{P}_{\Omega_P}\hat{\psi}, \tag{5.8}$$

with the non-negative electron density constraint Ω_P for this variant:

$$\Omega_P = \ \{\forall\, x \in \psi : \arg(x) \in [-\infty, 0],\ |x| \in [0,1]\}\,. \tag{5.9}$$

To quantify the defocus error Δ_{01}, the projected wave-field is propagated into the detector plane and the average error square of the amplitudes to the measured hologram is calculated. We call the newly generated focus criterion for a wave-field model fit error (MFE$_w$), which is calculated by

$$\mathrm{MFE}_w = \left\| |\mathcal{D}_{\mathrm{Fr}}^{\hat{z}_{12}}(\hat{\psi}_P)| - \sqrt{\mathcal{I}_{\mathrm{det}}} \right\|_2^2. \tag{5.10}$$

Under the conditions $\hat{z}_{12} = z_{12}$ and $\hat{\psi}_P = \hat{\psi} = \psi_{\mathrm{exit}}$, we know that $\Delta_{01} = 0$ and Eq. 5.10 becomes identical to the data consistency term in the inverse problem Eq. 3.18. If we use Eqs. 5.5 to 5.8 in Eq. 5.10, we obtain the MFE$_w$ criterion, parameterized with the measurement error Δ_{01}:

$$\mathrm{MFE}_w = \left\| \left|\mathcal{D}_{\mathrm{Fr}}^{-\Delta_{01}}(\mathcal{D}_{\mathrm{Fr}}^{z_{12}}(P_{\Omega_P}\mathcal{D}_{\mathrm{Fr}}^{\Delta_{01}}(\psi_{\mathrm{exit}})))\right| - \sqrt{\mathcal{I}_{\mathrm{det}}} \right\|_2^2. \tag{5.11}$$

Instead of analyzing an image or a wave-field for optical criteria, the MFE criterion measures the fitting of the forward model with respect to the measured hologram. The value of the data consistency term decreases with decreasing Δ_{01} and reaches its minimum for $\Delta_{01} = 0$. It can also be seen here that the defocused and projected wave-field $\hat{\psi}_P$ generated in the refractive representation is related to the inverse problem by the non-negativity constraint used in Eq. 3.18. We assume therefore the following relationship:

$$\hat{\psi}_P = \mathcal{P}_{\Omega_P}\mathcal{D}_{\mathrm{Fr}}^{\Delta_{01}}(\psi_{\mathrm{exit}}) \mapsto \tilde{O}^{*} = -\mathrm{i}\log\left[\mathcal{P}_{\Omega_P}\mathcal{D}_{\mathrm{Fr}}^{\Delta_{01}}(\tilde{O})\right], \tag{5.12}$$

and replace the wave-field of Eq. 5.10 by the reconstructed complex refractive index $\tilde{O}$. We thus obtain a MFE$_r$ focus criterion for reconstruction results of the refractive object

$$\mathrm{MFE}_r\left(\tilde{O}^*\right) = \left\| |\mathcal{D}_{\mathrm{Fr}}^{\hat{z}_{12}}(\tilde{O}^*)| - \sqrt{\mathcal{I}_{\mathrm{det}}} \right\|_2^2, \tag{5.13}$$

which we can use to derive a combined optimization problem in the next section.

5.3 Optimizing z_{01}

In this section, we will now derive the complete algorithm to optimize the distance z_{01} between the focus of the optics and the measured object in the forward model of the reconstruction. The algorithm is divided into three parts, inverse problem, focus criterion and the solver.

First, the formulation of the inverse problem is required. To do this, we create an objective function that is to be minimized using the z_{01} parameter and whose solution is an approximation z_{01}^* of the correct distance and is within a measurement uncertainty interval. The minimization problem thus has the structure

$$z_{01}^* = \underset{z_{01}\in\mathbb{R}}{\operatorname{argmin}}\ f(z_{01}) + \mathcal{X}_{\Omega_z}(z_{01}) \tag{5.14}$$

with a constraint on possible z_{01} values due to the measurement uncertainty Δ_{01}. The constraint set Ω_z is defined as

$$\Omega_z = [z_{01}^{\mathrm{est}} - \Delta_{01}, z_{01}^{\mathrm{est}} + \Delta_{01}] \subset \mathbb{R}. \tag{5.15}$$

Within the function $f(z_{01})$, a focus criterion $g(\tilde{O}^*(z_{01}))$ should be applied, which quantifies the z_{01} distance based on reconstructed refractive objects $\tilde{O}$. For this purpose, we must first generate a reconstruction result depending on z_{01}, which in turn is processed by a focus criterion. Therefore, we define the error function $f(z_{01})$ for g with a maximum or a minimum as

$$f(z_{01}) = g(\tilde{O}^*(z_{01})), \tag{5.16}$$

and parameterize the reconstruction result $\tilde{O}^*$ with the distance z_{01}. We thus obtain two variants of an constraint inverse problem for the z_{01} distance, depending on the direction of the extremum of function g in the constraint interval:

$$z_{01}^* = \underset{z_{01}\in\mathbb{R}}{\operatorname{argmin}}\ \pm g(\tilde{O}^*(z_{01})) + \mathcal{X}_{\Omega_z}(z_{01}). \tag{5.17}$$

The above can be split into a two-stage inverse problem. First, a solution $\tilde{O}^*$ is reconstructed based on a given z_{01} and in a second step the approximation z_{01}^* is optimized. An iterative algorithm can then be used to alternate between the two problems.

Since we do not have direct access to the gradient $\frac{\delta}{\delta z_{01}} f(\tilde{O}^*(z_{01}))$ with this two-stage method, we need a gradient-free method to solve the higher-level minimization problem Eq. 5.14. A method that is robust against noise is the so-called downhill simplex

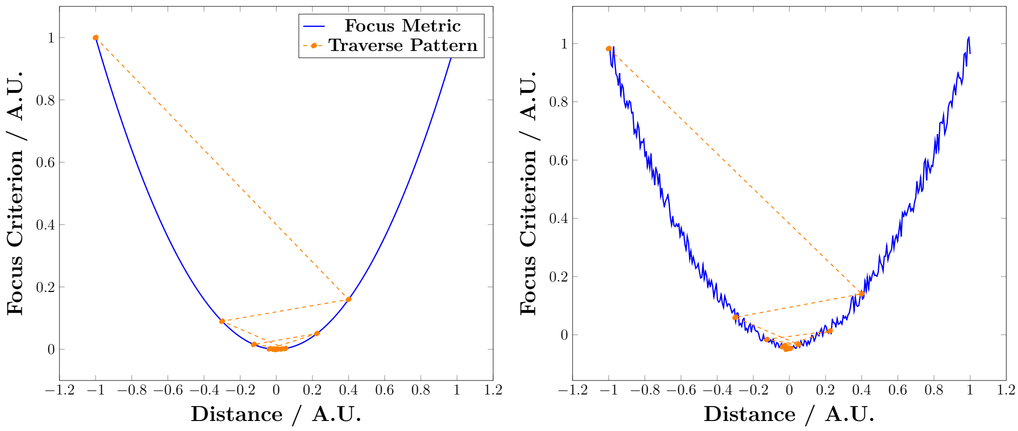

Figure 5.4: The NM method applied to an ideal and noisy parabolic function. (left) Demonstration of the underlying principle. The method traverses a function by probing single points. The first two connected points create a simplex that shrinks over time. After some iterations, the method reaches a minimum. The algorithm terminates when a certain predefined simplex length is reached. (right) Demonstration of robustness against noise. It can be seen that although the function is corrupted by noise, the NM method traverses a similar path towards the minimum.

method, which is also known as the Nelder-Mead (NM) method. This is a numerical method for optimizing multivariate objective functions, which can also be non-convex and non-linear [101, 102]. It is an iterative method that optimizes an objective function without requiring a calculation of derivatives in each iteration. Instead, the objective function is probed by corner points of a multidimensional simplex, which shrinks iteratively towards a minimum. The iterative algorithm stops when the size of the simplex falls below a predefined threshold. This numerical method can also be used as a tool to optimize scalar functions where analytical gradients are not available and is very robust to HF noise. The algorithm is also qualified to find a global minimum, if it falls inside of a certain tolerance window. Figure 5.4 visualizes how the simplex algorithm traverses a clean and a noisy function with only one scalar to optimize. For illustration, we chose a simple parabolic function.

5.4 Reconstruction of $\tilde{O}$

The argument of the MFE focus criterion are the reconstructed projected refractive indices $\tilde{O}^*$ at a sample point $\hat{z}_{01}$. Explicitly designing a reconstruction of $\tilde{O}$ for AF is a particularly critical point that receives little or no attention in the AF literature [96–100]. Typically, the AF problem is approached from the perspective of the criterion, not regarding image quality or properties of the reconstruction algorithm for $\tilde{O}$. However, it would be more accurate to say that the criterion and the reconstruction are interdependent. If a specific focus criterion depends on certain features to quantify the defocus error, the algorithm must be able to generate those features. Conversely, an image feature may be a particular property of the algorithm, e.g. image artifacts. Additionally, in the setting of NFH, due to the non-convexity and non-linearity of the data fidelity term in the inverse problem, a deterministic reconstruction result is in principle not guaranteed and may converge to different images for different initial values. The reconstruction result will also always contain some level of noise which challenges the robustness of focus criteria. Thus, to generate a focus curve with good properties there is a combined problem to solve, and the criterion and the reconstruction algorithm should always be analyzed as a unit. In general, the following requirements must be met by the reconstruction algorithm

- (i) The reconstruction must produce mutually consistent results with respect to the variation of the z_{01} distance. In AF, it is not enough to achieve a good result in a single reconstruction. The features analyzed by the focus criterion must change consistently and uniformly as z_{01} varies.
- (ii) For the analysis of the reconstruction result, the reconstructed image must therefore be as free from artifacts and noise as possible. This is especially true for artifacts with high spatial frequencies, since many criteria use the image gradients as a basis for quantifying the defocus position.
- (iii) Since a new reconstruction result must be generated for each variation of z_{01}, more iterations are required to solve the global AF problem than for the reconstruction of a single z_{01}. The reconstruction might have to be run from the beginning for each new z_{01} in some cases. The reconstruction algorithm should therefore be able to produce individual results in a reasonable time.

The reconstruction problem $\tilde{O}^*(z_{01})$ is already known from Ch. 4. We only need to slightly modify the inverse problem and parameterize it with z_{01}. To do this, we parameterize the Fresnel number in the forward model, which then adapts as z_{01} changes. With the methods for artifact reduction presented in Ch. 4, we obtain for the solution

$$\tilde{O}^*(z_{01}) = \operatorname*{argmin}_{\tilde{O}} \frac{1}{2} \left\| \left|\mathcal{D}_{\mathrm{Fr}}(z_{01},\tilde{O})\right| - \sqrt{S_{\downarrow}\mathcal{I}_{\mathrm{det}}} \right\|_2^2 + \mathcal{X}_{\Omega_P}(\tilde{O})\|_2 \tag{5.18}$$

under the constraint set

$$\Omega_P = \left\{\forall\, x \in \tilde{O} : \mathrm{Re}(x) \in [-\infty, 0],\ \mathrm{Im}(x) \in [-\log\left(\sqrt{a_0}\right), \infty]\right\}. \tag{5.19}$$

The application to experimental data showed that reducing the resolution of reconstruction results is a good de-noising method and provided more stable and smoother curves for the focus criterion. We therefore add a downsampling operation $S_{\downarrow}$ of the measurement data. Furthermore, $\mathcal{D}_{\mathrm{Fr}}(z_{01},\tilde{O})$ is the parameterized Fresnel propagation kernel with

$$\mathcal{D}_{\mathrm{Fr}}(z_{01},\tilde{O}) = \mathcal{F}^{-1} \circ \exp\left(-i \cdot \pi \frac{(k_x^2 + k_y^2)}{\mathrm{Fr}(z_{01})}\right) \circ \mathcal{F} \circ \psi_{\mathrm{exit}}(\tilde{O}) \tag{5.20}$$

and the parameterized Fresnel number $\mathrm{Fr}(z_{01})$. Depending on the known distances, either z_{12} or z_{02}, the Fresnel number derived from the Fresnel scaling theorem is

$$\mathrm{Fr}(z_{01}) = \frac{\Delta x^2}{\lambda \frac{z_{01}+z_{12}}{z_{01}} z_{12}} = \frac{\Delta x^2}{\lambda \frac{z_{02}}{z_{01}} (z_{02} - z_{01})}. \tag{5.21}$$

We now have a complete reconstruction framework and can apply it to simulated and experimental data in the next step.

5.5 Performance Evaluation

5.5.1 Criteria for Comparison

The criteria in literature [96, 98–100] usually refer to the optical sharpness that a human would use as a criterion for manual analysis and attempt to quantify this sharpness and derive a single scalar. The quantification can be carried out using different image processing algorithms, which are combined with statistical methods.

There are multiple factors that influence whether an image is perceived as sharp by a human. One is the presence of steep edges. This is also used in image processing algorithms that artificially sharpen the image for the viewer, e.g. by adding an overshoot of the edges using the convolution of the image with an unsharp mask. The mask adds the result of a weighted Laplacian to the current image and the result then appears sharper.

Mathematically, the image sharpness can be quantified by extracting the image gradients and applying a statistical analysis. There are several variants in the literature for quantifying image sharpness with a simple, discrete differentiation. The gradient (GRA) criterion [99] applies a difference operator to the image and sums up the result. This can be expressed as

$$\mathrm{GRA}(h) = \sum_x \sum_y \nabla h_{x,y} \tag{5.22}$$

where h is the input image and (x, y) denotes the image pixel coordinates. The discrete derivative operator is defined as

$$\nabla h_{x,y} = \sqrt{|h_{x,y} - h_{x,y-1}|^2 + |h_{i,j} - h_{i-1,j}|^2}. \tag{5.23}$$

A second variant, the laplacian (LAP) criterion [99], does not use the first but the second derivative to quantify the image sharpness. Here, the image is convolved with a discrete Laplace operator and the result is summed up again. The LAP criterion is

$$\mathrm{LAP}(h) = \sum_x \sum_y \nabla^2 h_{x,y}, \tag{5.24}$$

with the following discrete Laplace operator

$$\nabla^2 h_{x,y} = \left(h_{x+1,y} + h_{x-1,y} + h_{x,y+1} + h_{x,y-1} - 4h_{x,y}\right)^2 . \tag{5.25}$$

Two other focus criteria complement the gradient approach to determine the image sharpness and additionally analyze the sparsity of the image gradient. In the corresponding literature [100], two approaches were compared for analyzing the sparsity. One approach uses the Tamura coefficient (TC) [98], which makes use of the statistical tools of variance $\sigma(h)$ and mean $\overline{h}$ of the input. It results from

$$\mathrm{TC}(h) = \sqrt{\frac{\sigma(h)}{\overline{h}}}. \tag{5.26}$$

Another approach is based on the Gini index (GI) [103], which performs a more complex calculation, with

$$\mathrm{GI}(h) = 1 - 2\sum_{k=1}^{N} \frac{a_k}{\sum_i h_i} \left(\frac{N - k + 0.5}{N}\right). \tag{5.27}$$

Here, the input image h is sorted by size in descending order. The variable a_k is then the k-th entry of the sorted vector.

Two focus criteria Tamura coefficient of the gradient (ToG) and Gini index of the gradient (GoG) [100] are then derived from the two sparsity measures TC and GI by taking the magnitude of the real-valued image gradient as the input value g in each case. We obtain with Eq. 5.23

$$\mathrm{ToG}(h) = \mathrm{TC}(\nabla h), \tag{5.28}$$

$$\mathrm{GoG}(h) = \mathrm{GI}(\nabla h). \tag{5.29}$$

The spectrum (SPEC) criterion [99] quantifies the image sharpness using the frequency domain. As mentioned at the beginning, steep edges correspond to the HF components of the image. The focus criterion picks up on this property and weights the frequency components. The weight results from the natural logarithm, whereby the weight increases with increasing frequency. The SPEC criterion is calculated with

$$\mathrm{SPEC}(h) = \sum_{k_x}\sum_{k_y} \log\left(1 + |(B \circ \mathcal{F}(h))(k_x, k_y)|\right). \tag{5.30}$$

The image h is first filtered with a bandpass consisting of the convolution kernel B to exclude the constant at the zero frequency in particular and to increase robustness.

A final focus criterion follows a different approach. In contrast to analyzing the edge strength in the image, the variance (VAR) criterion [99] determines the contrast of the

Parameter	Symbol	Value
Illumination Wavelength	λ	0.112 nm
Detector Pixel Size	Δx	6.5 µm
Focus Object Distance	z_{01}	10 cm
Focus Detector Distance	z_{02}	20 m
Measurement Uncertainty	Δ_{01}	5 mm

Table 5.1: Model parameters that were used for the simulation of the input hologram for the MFE criterion.

input image. One method for this is to calculate the variance of the gray value distribution over the entire image with

$$\mathrm{VAR}(h) = \sum_x \sum_y \frac{|h(x,y) - \overline{h}|^2}{N_x N_y}. \tag{5.31}$$

It should be noted that the criteria above were analyzed with certain restrictions in their respective literature, which are discussed in Sec. 5.6. Since it is not known whether the restrictions made in the literature can be lifted with a different reconstruction algorithm, these restrictions will be omitted for comparison. We perform a reevaluation using only the reconstruction results of Ch. 4 without further constraints.

5.5.2 Simulated Data

In the following, an initial comparison of the MFE criterion presented in Sec. 5.2 with the criteria of Sec. 5.5.1 is performed on simulated data. The forward model and the phantoms are used according to Ch. 3 and the holograms are calculated respectively. For testing, the cell, triangle and ball phantoms from Fig. 3.3b of Sec. 3.4 are chosen.
The parameter for the simulation with a setup according to Fig. 2.3) are listed in Tab. 5.1. The illuminating beam is assumed to be a monochromatic, coherent beam with an intensity of one, i.e. is assumed to be a planar wave. With these setup parameters, we generate a MFE focus curve with Eq. 5.13 for each of the phantoms. The curves are created as follows: The parameter $\mathcal{I}_{\mathrm{det}}$ is deviation independent and is a simulated hologram from the applied parameters of Tab. 5.1 to the forward model of Sec. 2.3. The Fresnel propagation kernel $\mathcal{D}_{\mathrm{Fr}}^{\hat{z}_{12}}(\cdot)$ and the argument $\tilde{O}^*$ are both deviation dependent and have to be adapted for each distance $\hat{z}_{01}^{j}$.
For the simulation, the focus curves should be generated in a reasonable interval. This interval is the complete range that the proposed NM based approach of Sec. 5.3 would cover. The NM method is a gradient-free method and therefore the search direction is unknown. Under the condition that it has been initialized with an estimated value z_{01}^{est} (Eq. 5.15), it will scan the focus curve in positive and negative direction with a maximum

distance of Δ_{01}. However, z_{01}^{est} itself may deviate from the correct distance by Δ_{01}. It is therefore reasonable to create a focus curve in an interval of twice the measurement uncertainty around the correct distance such that the values $\hat{z}_{01}^{j}$ for the propagation kernel are chosen from the interval

$$\hat{z}_{01}^{j} \in [z_{01} - 2\Delta_{01}, z_{01} + 2\Delta_{01}] . \tag{5.32}$$

The chosen distance $\hat{z}_{01}^{j}$ is used for propagation by using the Fresnel propagation kernel of Eq. 5.20, i.e.

$$\mathcal{D}_{\text{Fr}}^{\hat{z}_{12}}(\cdot) \rightarrow \mathcal{D}_{\text{Fr}}(\hat{z}_{01}, \tilde{O}^{*}), \tag{5.33}$$

which is parameterized by the distance with deviation $\hat{z}_{01}$. For each chosen $\hat{z}_{01}^{j}$, the related deviation Δ_{01}^{j}, which is needed for the calculation of $\tilde{O}^{*}$, is then implicitly given by

$$\Delta_{01}^{j} = \hat{z}_{01}^{j} - z_{01}. \tag{5.34}$$

The argument $\tilde{O}^{*}$ above is given by assuming the relationship Eq. 5.12 and is calculated by

$$\tilde{O}^{*} = -\mathrm{i} \log \left(\mathcal{P}_{\Omega_P} \mathcal{D}_{\text{Fr}}(\Delta_{01}^{j}, \tilde{O}) \right), \tag{5.35}$$

where the phantom $\tilde{O} \in \{\text{cell,triangle,ball}\}$ is propagated to the distance Δ_{01}^{j} and then projected onto the non-negative electron density constraint Ω_P. It should be noted that the simulation of a reconstruction with this simple function is only valid as long as no phase wraps occur. The values for the refractive object $\tilde{O}$ must be selected accordingly or a phase unwrapping must be performed. The results of the simulation are shown in Figs. 5.5 to 5.8, where 201 points were sampled for each curve.

5.5.3 Experimental Data

The MFE criterion and the focus criteria from Sec. 5.5.1 are also compared with respect to experimental data. As test objects, the four experimental samples from Fig. 3.3a of Sec. 3.4 are used under identical measurement conditions as in Sec 4.6.4. Additionally, a magnesium-based wire was placed into an *in-situ* flow-cell, which was filled with ethanol [22]. In Sec. 4.6, the z_{01} distances of the forward models for the reconstructions were manually optimized using a reconstructed image series and by visually analyzing the results. Before manual focusing, the distance value z_{01}, as described in Sec. 5.1, was roughly estimated with an accuracy of ±5 mm using a ruler at the measurement station. For a visual analysis of the image series, the reconstructed phase images were displayed as gray-scale images and then the sharpest image from the series was selected. For validation, a one-dimensional plot of the values orthogonal to an edge of the measured object was also considered and the edge steepness was analyzed. We use the values for z_{01} determined in this way as a reference for centering the focus curves.

Iterations		700	300	500
Downsampling	U	16×	4×	4×
Udate Rate	η	0.9	1.1	1.1
Momentum Weight	γ	1.0	1.0	1.0
Momentum Variance	σ	8	16	16
L_2 Weight	β	10.0	10.0	1.0
Filter $\tilde{O}$		2.0/8.0	2.0/8.0	2.0/8.0

Table 5.2: Reconstruction parameters for the solver of the minimization problem Eq. 5.18, which was used to reconstruct $\tilde{O}(z_{0x})$. Applied stepwise from left to right. The filter $\tilde{O}$ values are given in Full Width at Half Magnitude (FWHM) for real and imaginary parts in form of $\text{FWHM}_{\text{real}}/\text{FWHM}_{\text{imag}}$. The momentum variance is given as FWHM in pixels where $\sigma = FWHM/2.35$.

The focus curves should be generated in a reasonable interval for the objects and the focus criteria. The interval corresponds to twice the measurement uncertainty around the previously manually determined distance value, which was described in Sec. 5.5.2. In this interval, we sample 201 values for z_{01} at equidistant steps and perform at each point a single reconstruction. To do this, we solve the minimization problem Eq. 5.18, which includes the Fresnel propagator Eq. 5.20 parameterized for z_{01}. As an additional denoising method and to reduce computation time, we use an operator $S_{\downarrow}$ for the data with a 4× downsampling factor for the final stage. This ensures that for *in-situ* experiments the NM algorithm finds an existing extremum in a reasonable time. The reconstruction parameters are summarized in Tab. 5.2. The reconstructed refractive indices are then evaluated individually for each focus criterion. The results are shown in Figs. 5.5 to 5.8.

5.5.4 Results

The generated focus curves are shown in Figs. 5.5 to 5.8. Each plot has the same structure. On the x-axis is the deviation Δ_{01} from the reference z_{01} value in mm. On the y-axis is the evaluated value of the respective focus criterion in the representation Eq. 5.16 of Sec. 5.3. Values between the sampling points were linearly interpolated. For better comparability, the value range of the y-axis was normalized to an interval of $[0, 1]$. The following analysis evaluates the different focus criteria. A good focus criterion should fulfill the requirements from Sec. 5.2 to be compatible with a NM approach.

The properties of the focus criteria, applied to the simulated objects, differ significantly from each other:
Five of seven criteria produced clear extrema in the generated curves that also point into

the same directions: MFE (Fig. 5.5a), GRA (Fig. 5.6a), LAP (Fig. 5.6b), GoG (Fig. 5.7a) and ToG (Fig. 5.7b).

Two criteria, the VAR (Fig. 5.8a) and SPEC (Fig. 5.8b) criteria failed to produce distinct peaks. The VAR criterion shows no consistent clear extrema for all objects and the directions of the peaks of the SPEC criterion switched between the tested objects.

Four criteria produced curves that are continuously falling and rising to the extrema. These criteria were the MFE, GRA, GoG and the ToG criteria.

The noise in the curves of one criterion, ToG, has partly a magnitude in the order of the slope of the curves.

An application of the focus criteria to the data measured at the beamline show that each curve appear to be heavily influenced by the kind of object that was measured. Smooth objects like the cactus needle and the two magnesium-based wires produced more smooth curves than objects that contain more structure in the projection images, like the spider hair with many fine details and the tooth, which has step-like structures induced by the focused ion beam. The spider hair and the tooth produced in most of the criteria distinct peaks at the center. Although the peaks are not all aligned in the center, they are still in a plausible range, where the visual analysis does not yield a clear result for the sharpest position. In the range of the overall measurement uncertainty of z_{01}, many of the curves contain very distinct side peaks that are clearly not at the sharpest position. Specifically, the criteria are LAP, ToG and GoG, GRA and SPEC. The VAR criterion behaves similar to the simulation, where the sharpest position only induces a significant gradient in the curve without producing a peak. At the positions, were the objects produced side peaks in all other criteria, the impact on the MFE criterion is more subtle. The MFE criterion appears to be more robust since these positions produced only minor saddle points in the focus curve.

Eventually, the AF algorithm from Sec. 5.3 was applied to the experimental data. As the objective function for optimizing z_{01}, Eq. 5.17 was used together with the MFE criterion. Based on the z_{01}^{est} value of Eq. 5.15, estimated at the beamline, an initial simplex was created for each object. The initial simplex consists of two points, which are located in the same interval as the plots of the focus curves. The optimization algorithm stops as soon as the remaining simplex reaches a size of 100 µm. The initial simplex, the reconstructed distance and the required number of sample reconstructions are shown in Tab. 5.3. The Nelder-Mead approach required between 9 and 13 probing points on the MFE curve, each consisting of a single reconstruction of $\tilde{O}$. Depending on the array size, a single reconstruction with the parameters of Tab. 5.2 needed between 6 s and 16 s. In total, the optimization of z_{01}therefore took between 66 sec for the smallest array and 208 sec for the largest array. The full reconstructions at the positions found by the Nelder-Mead approach are shown in Fig. 5.9

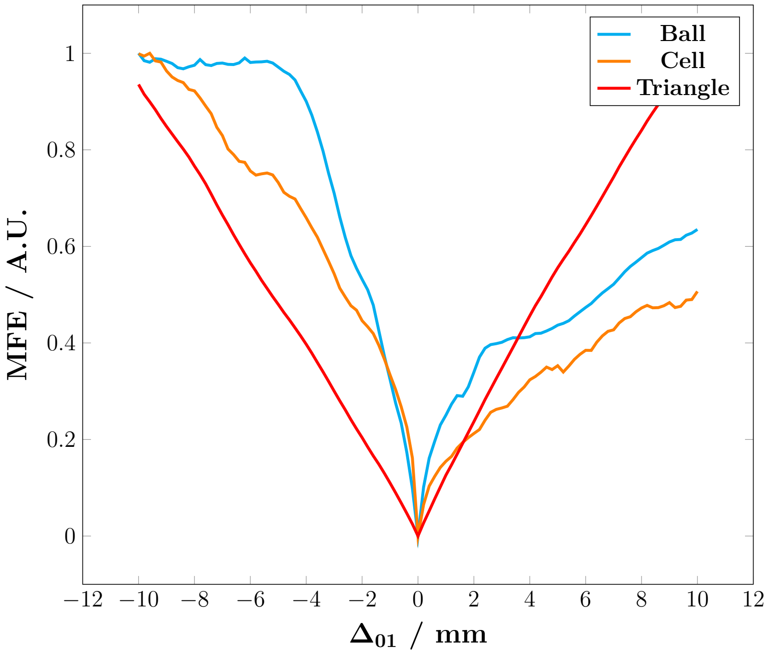

(a) MFE Simulated Objects

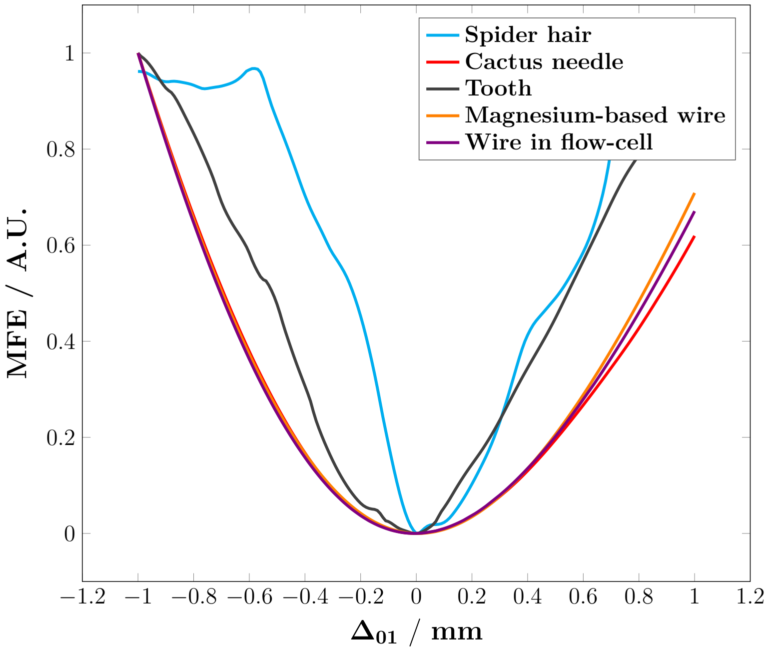

(b) MFE Experimental Data

Figure 5.5: Focus curves of the developed MFE criterion for measurement deviations of the z_{01} distance of ±10 mm. The center was manually aligned according to an optical focus impression. All curves show a pronounced minimum in the center and smooth curves with high SNR. Local minima are only weakly pronounced.

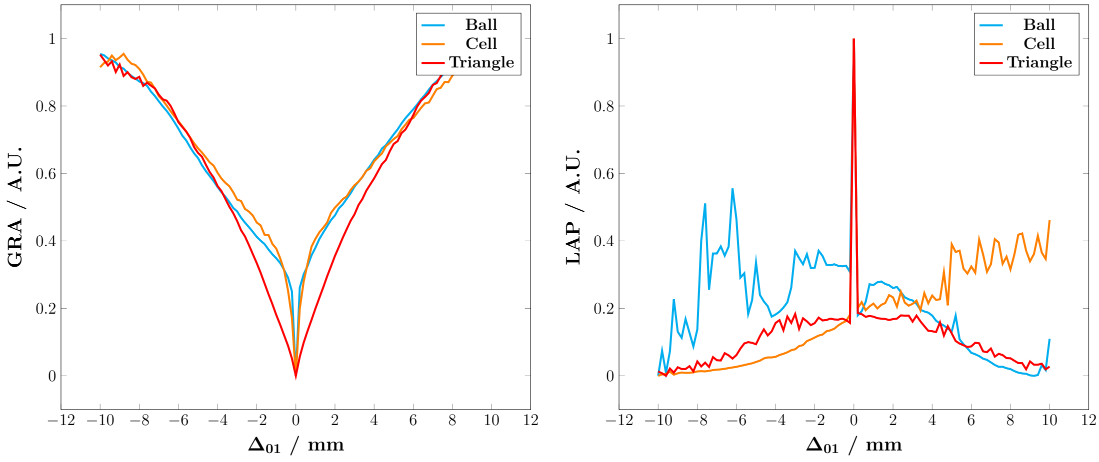

(a) GRA Simulated Objects

(b) LAP Simulated Objects

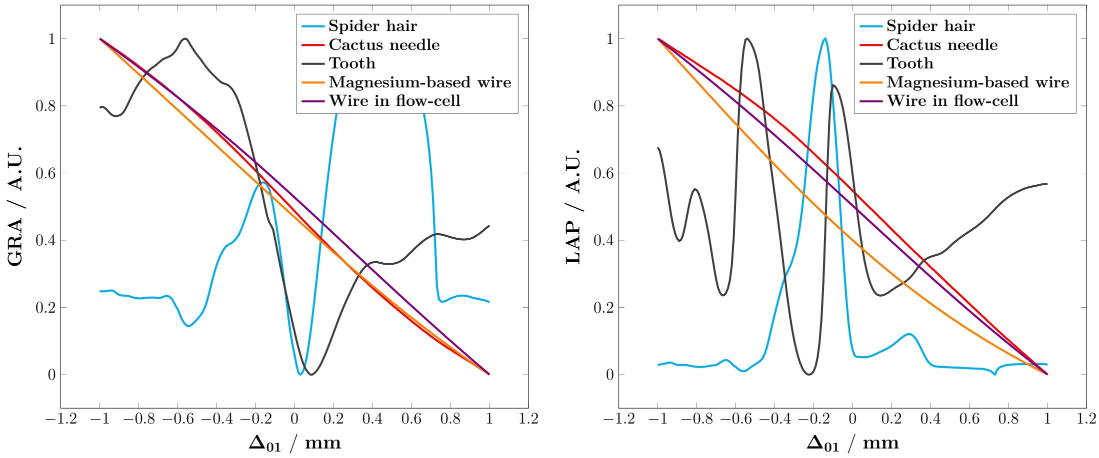

(c) GRA Experimental Data

(d) LAP Experimental Data

Figure 5.6: Focus curves of the GRA and LAP criteria for measurement deviations of the z_{01} distance of ±10 mm. The center was manually aligned according to an optical impression of sharpness. Both criteria are based on the analysis of image gradients. The GRA criterion calculates the first discrete derivative and generated a minimum at the center for all objects in the simulation. Experimental data could reproduce the curve shape of the simulation only for two datasets and only in the vicinity of the center. The LAP criterion produced very noisy curves in the simulation with clear maxima in the center. In experimental data, the criteria only produced a local peaks for two datasets in the vicinity of the center and side peaks that are clearly not at the sharpest position.

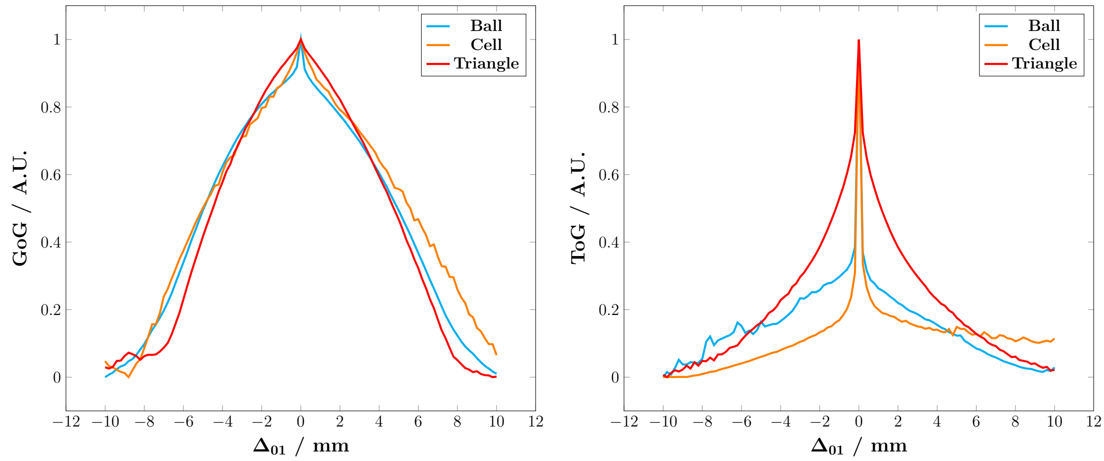

(a) GoG Simulated Objects

(b) ToG Simulated Objects

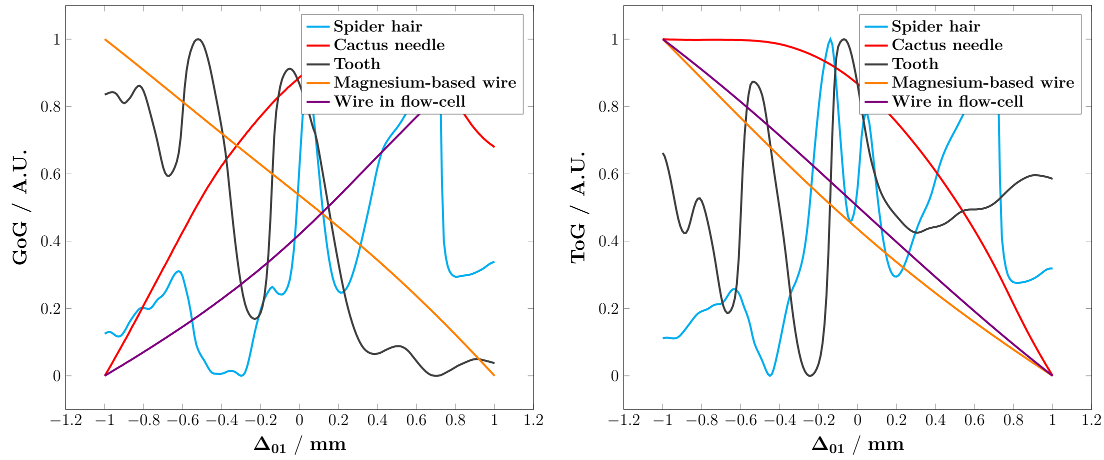

(c) GoG Experimental Data

(d) ToG Experimental Data

Figure 5.7: Focus curves of the GoG and ToG criteria for measurement deviations of the z_{01} distance of ±10 mm. The center was manually aligned according to an optical impression of sharpness. Both criteria are based on the statistical analysis of the first-order image gradient. In the simulation, all curves have a clear maximum in the center. The ToG criterion generates relatively flat curves and has noise that is in the order of magnitude of the curve gradient. The ToG curves become steep only in the center. In the experimental data, the curves show similar patterns only for two objects and only near the center but are oscillating curves otherwise. The side peaks of the oscillation that are clearly not at the sharpest position.

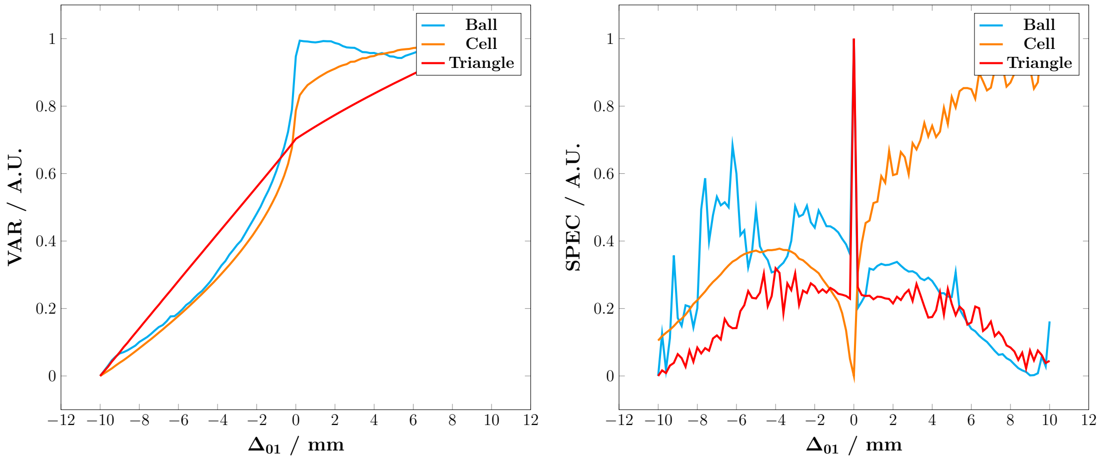

(a) VAR Simulated Objects

(b) SPEC Simulated Objects

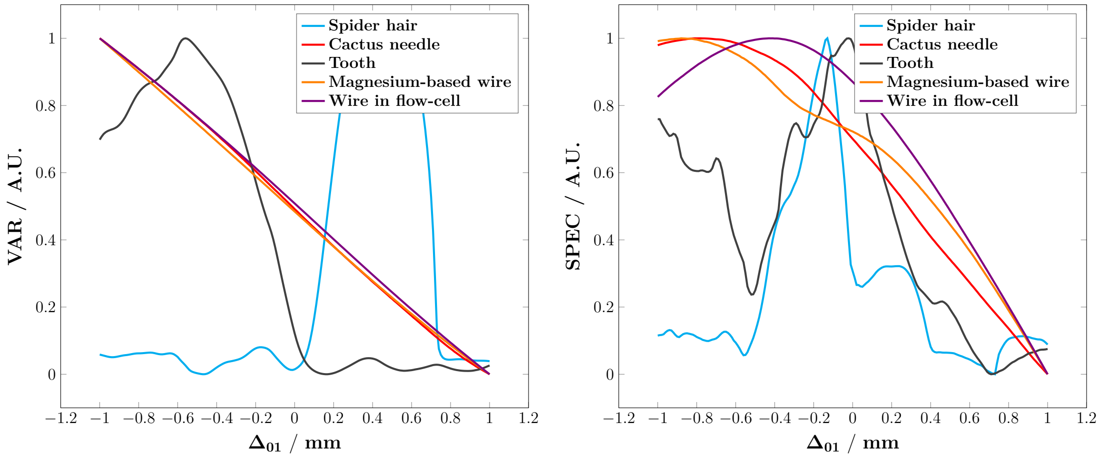

(c) VAR Experimental Data

(d) SPEC Experimental Data

Figure 5.8: Focus curves of the VAR and SPEC criteria for measurement deviations of the z_{01} distance of ±10 mm. The center was manually aligned according to an optical impression of sharpness. The VAR quantifies the image contrast via the variance of the gray values. The SPEC criterion calculates a sum of weighted image frequencies. The curves of the VAR criterion do not form extremes in the simulation, but tend to form a maximum in the center. The focus curves of the SPEC criterion form a maximum or a minimum depending on the object. In the experimental data, the VAR criterion behaves for two objects similar to the simulation where the sharpest position introduces a gradient in the curve . The SPEC criterion forms maxima in the vicinity of the center for two objects and maxima in defocus for the other objects.

	Type	Full Grid Size / px	Down-sampled Grid Size / px	Time / $\frac{\text{s}}{\text{Sample}}$
	(1)	14336×14336	3584×3584	16
	(2)	8192×8192	2084×2084	6

Object	Type	Initial Simplex	NM Result	Visually Determined	Required Samples
i	(1)	74.8 mm / 84.8 mm	79.4 mm	79.4 mm	13
ii	(2)	77.9 mm / 87.9 mm	80.9 mm	81.0 mm	11
iii	(2)	281.1 mm / 291.1 mm	284.2 mm	284.2 mm	12
iv	(1)	467.4 mm / 477.4 mm	470.8 mm	470.7 mm	9
v	(1)	324.2 mm/334.2 mm	329.3 mm	329.3 mm	13

Table 5.3: Results of z_{01} optimizations with the developed AF algorithm of Sec. 5.3. A downhill simplex method was used to find the minimum of a target function which is the MFE criterion from Sec. 5.2. The algorithm starts with an initial simplex consisting of two points. The simplexes have a total length of 1 cm, which are derived from the measurement uncertainty $z_{01}^{\text{est}} \pm 5\,\text{mm}$. Upper Table: The measurements are sorted into two types: Depending on the Fresnel number, the measurements needed to be padded to two different array sizes [21]. The probing reconstructions of the Nelder-Mead approach were performed on a 4× downsampled grid. Bottom Table: We tested the optimization of $z_{01}$for the samples (i) spider hair, (ii) tooth, (iii) cactus needle, (iv) magnesium-based wire, (v) magnesium-based wire in flow-cell. In 9 to 13 steps, each simplex reached a predefined length of 100 µm and the algorithm found the minimum. The minimums match the point of optical sharpness which was visually validated. At each step, a reconstruction was performed with parameters that are shown in Tab. 5.2.

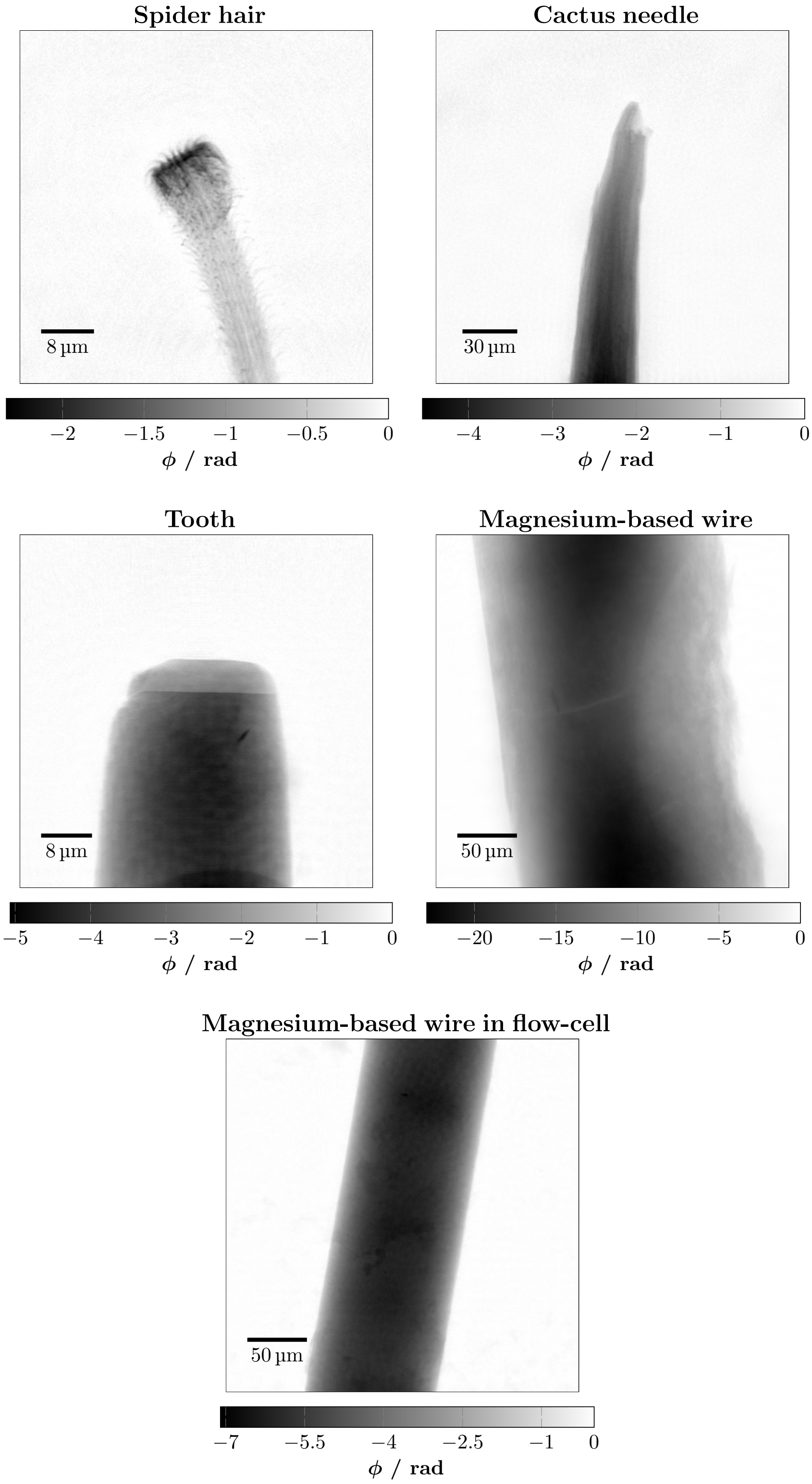

Figure 5.9: Reconstructions of the test objects with the z_{01}model parameters as determined by Nelder-Mead results of Tab. 5.3. The images here show phase images reconstructed in full resolution from single-shot near-field holograms. The phase shifting strength (ϕ) is described by the color bars.

5.6 Discussion and Outlook

In this chapter, we investigated the AF problem of NFH data, where the numerical focus z_{01} of the forward model in Sec. 2.3 needs to be optimized to be able to reconstruct sharp images. In this course, the ASRM algorithm of Ch. 4 was modified to provide an input for the optimization problem of Sec. 5.3 under an estimated. The requirements were determined and the Fresnel propagation kernel parametrized by an estimation for z_{01}. In Sec. 5.5 the performance of the proposed MFE criterion was compared against existing criteria found in literature with respect to simulated and experimental data. For the simulated data, the GRA, GoG, ToG and MFE criteria created all curves of sufficient quality for an application with a NM optimization approach. Applied on the experimental data, the MFE approach outperformed the compared criteria and was the only one that exhibits sufficient robustness such that the minimum of the optimization problem lies at the position of the correct numerical focus.

Overall, it is difficult to determine whether the focus criterion is not robust enough if the conditions are not met or whether the reconstruction algorithm for the input image generates images that are too inconsistent. This problem was described in Sec. 5.4. We can however identify differences between the studies of this work and of the compared criteria from literature that may explain the performance results. The probably most important difference is that the compared criteria perform a quantification by an image analysis of the reconstructed projected refractive index without including the assumptions made for the reconstruction or the raw data. The MFE criterion on the other hand includes both and does not analyze the image but aims to find a good model for the reconstruction. The available studies in literature were also done under certain restrictions that limits the validity of the study results for the problem of this work. The studies of [99] were performed for a different measurement setup, the off-axis microscopy which enables advanced knowledge of the illumination. The reconstruction of the projected refractive index in this case becomes simpler by some order. The reference algorithm refAP and the developed ASRM algorithm of this thesis are new approaches that both prevent a phase wrapping problem. These were not available for the criteria tested in literature. The criteria of [99] were therefore only applied on a real valued input which was the amplitude distribution of the exit wave-field values, because of phase wrapping problems. Application on phase values was not sufficiently tested. The reconstructions of [100] for the ToG and GoG criteria were performed with a spatial support constraint, which implicitly introduces a ROI selection. Especially the GoG criterion was shown to require the manual selection of a ROI if the sample becomes too sparse. Furthermore, the study avoided statements about the interaction strength of the tested objects and the absolute phase-shift values are unknown for the reader. Since a simple back-propagation without any phase retrieval was also performed for quantification, it is very probable that the tested samples do not have a phase wrapping problem. A final issue results from the non-negative electron density constraint Ω_P used in ASRM. For defocused objects, it removes parts of the propagation fringes that appear. While this effect is exploited for the MFE criterion, it may cause problems for image analysis based criteria.

This chapter demonstrated that the proposed AF algorithm for NFH is able to focus a wide range of real objects and experimental setup conditions. The proposed model fit error based focus criterion MFE yields a superior robustness compared to the statistical analysis of reconstructed images. The AF problem and the results of this work are also not only relevant for this specific setup but also extends to other microscopy setups and reconstruction algorithms that use the Fresnel free-space propagation in the forward model. The proposed algorithm can be adapted for any parameter that is part of the Fresnel number in the forward model of an experimental setup, including propagation distance, energy, pixel size and others. This flexibility and the demonstrated robustness makes the method highly useful for *in situ* and *operando* studies.

For future work, the study should be extended and also include other types of objects. Especially objects that exceed the FOV of the detector in all directions were not tested. Since this requires also an available reconstruction result, the ASRM algorithm of Ch. 4 should previously be investigated for such objects. Alternatively, this reconstruction may be approximated by performing a ROI selection on the reconstructed object and the hologram. It would also be reasonable to explore the limitations of the focus criterion with respect to reconstruction time and resolution in combination with an experimental ground truth. Ground truth object for experiments at a synchrotron radiation light source are in general very difficult to produce. A good start may be a simple object of known dimension such as single polystyrene balls with a diameter of 5 µm to 10 µm.

Summary and Outlook 6

In this thesis, a new reconstruction algorithm for X-ray near-field holography was developed. The goal was to reconstruct the projected complex refractive indices of an object from a single hologram without a spatial support constraint. This unique combination of requirements was an open reconstruction problem that had to be solved to meet the long-term goal of this project to enable in situ/operando measurements at synchrotron radiation sources. The main challenges were to deal with reconstruction artifacts, to increase the reconstruction speed, and to reduce the number of parameters that had to be set manually.

In Ch. 2, the physical fundamentals necessary to describe the measured data were given. The projection approximation for the complex refractive index was derived as the target for the reconstruction. The reference setup for near-field holography in this work was described, which is a lensless microscopy setup for full-field imaging with hard X rays. The position of the detector was defined and the achievable resolution was calculated. Furthermore, the physical forward model required for the reconstruction was derived. A model for the present data noise was also build.

Chapter 3 dealt with the details of the reference reconstruction algorithm. The optimization problem was developed from a maximum likelihood approach and from prior knowledge of the measurement physics. A Poisson noise model was used and a non-negative electron density constraint was applied. The data were preprocessed by a flat-field correction approach to remove structure noise. To solve the optimization problem, the reference algorithm chosen was the projected gradient descent based algorithm refAP, where we removed the spatial support constraint. In the last section, the test data for the reconstruction were presented, which were (i) four experimental data sets from the P05 nano-endstation at PETRA III at DESY, Hamburg, operated by Helmholtz-Zentrum Hereon, and (ii) three simulation data sets based on the forward model.

Chapter 4 dealt with the reconstruction problem. The results of the reference algorithm suffered from various artifacts, which were divided into different categories. We found that the limited field of view of the detector leads to stripe- and ring-like truncation artifacts in the reconstruction. Furthermore, the algorithm overestimates the reconstructed values during the first few hundred iterations, caused by the Nesterov accelerated gradient, resulting in overestimation artifacts. It was also found that the algorithm has weak reconstruction capabilities for small image gradients due to a weak contribution of low spatial frequencies to the cost function, resulting in weak reconstruction artifacts. Low frequency artifacts occur when the non-negative electron density constraint does not match the reconstruction input. In sections 4.1.1 and 4.2 to 4.4, the identified categories and the methods to reduce the artifacts were proposed. To increase the reconstruction speed, a warm up scheme for the projected gradient descent based reconstruction was introduced. The final algorithm developed in this chapter was named artifact suppressing reconstruction method (ASRM) and employs several regularization techniques:

(i) To avoid truncation artifacts, the preprocessing of the measured holograms was improved. This included deriving a suitable padding scheme by mirroring the hologram in each direction and the application of a suitable window function. (ii) By adjusting the constant padding value a_0 and adapting the non-negative electron density constraint with a_0, a normalization offset in the flat-field correction was corrected, which reduced low frequency artifacts. (iii) To suppress the overestimation artifacts, the absorption values of the reconstructed refractive object were regularized with a weighted L_2 term. (iv) To increase the reconstruction capability of low spatial frequencies and thus reduce the weak reconstruction artifacts, a multigrid reconstruction was combined with a suppression of high frequencies in the Nesterov accelerated gradient.

The application to experimental data shows that the implemented algorithm is robust and fast with respect to a wide range of real objects that differ strongly in their interaction strength with the X-ray illumination. The combination of the L_2 regularization for the absorption values and the high frequency suppression provides a better reconstruction quality than either of the individual approaches. Two object-dependent parameters, σ for the Nesterov accelerated gradient weights and the constant value a_0 of the preprocessing and modified non-negative electron density constraint had to be tuned manually. The remaining parameters were object-independent and a common set of parameter values was found to be well suited and generalizable across the tested objects.

The topic of Ch. 5 was the autofocus problem. An inaccurate estimation of the Fresnel number of the forward model leads to blurred images as reconstruction results and carries the risk of reconstruction artifacts. Part of the Fresnel number is the distance of the numerical focus to the measured sample, which this chapter aimed to automatically optimize. A list of requirements was derived that needed to be met to solve the autofocus problem.

For this purpose, a novel focus criterion based on a model fitting approach was proposed, that was called the Model Fit Error (MFE). The criterion directly quantifies the fitting error of the forward model by exploiting the projection of the non-negative electron density constraint. The novel criterion was then embedded in an optimization problem, whose solution yields the correct numerical focus.

A gradient-less Nelder-Mead method as a solver was proposed for the optimization problem. The solver finds the optimum of a one-dimensional function in the presence of noise. The ASRM algorithm of Ch. 4 was modified to provide an input for a focus criterion under estimated model parameters. For this purpose, the Fresnel propagation kernel was parameterized with the value z_{01}. Furthermore, a common set of parameter

values was identified that proved to be well suited and generalizable across the tested objects.
The developed metric was then compared to six available metrics found in the literature with respect to simulation and experimental data. These metrics perform a statistical analysis of the reconstructed values rather than quantifying the model used. On simulated data, the MFE criterion and three of the compared criteria performed well under the previously established requirements. When applied to experimental data, only the curves of the developed MFE met all requirements. The minima are located at the correct numerical focus position, which was also verified optically and could be found automatically by the developed algorithm. In addition, the number of steps required by the Nelder-Mead-based algorithm was small enough to make autofocusing feasible for online reconstruction.

With the advent of fourth generation synchrotron radiation sources [4, 5, 104–106], coherent full-field imaging techniques are gaining more interest in new application areas, while for established scientific fields, the trend is towards dynamic studies of specimens, i.e. *in situ* and *operando* studies. The latter is followed by increasing demands on the measurement process in terms of acquisition parameters.Consequently, the requirements for the reconstruction process also increase. For supervising the experiment, a control software is available, for example, at the P05 endstation at PETRA III at DESY, Hamburg, operated by Helmholtz-Zentrum Hereon [8, 46, 64, 65]. The sample is usually placed on a rotation stage and many holograms have to be recorded from different angles to reconstruct a tomographic image. In the course of this work, the beamline control software was extended to include online reconstructions. The control interface was connected to a server application that performs the ASRM reconstruction on the Maxwell computing cluster at DESY. A new view offers the possibility to focus the image automatically and to navigate towards the desired region of interest of the sample, without relying only on holograms but with visually interpretable projection images.

With further performance improvements in the future, the results of this work could enable real-time reconstructions for *in situ*/*operando* experiments, to monitor and control the state of dynamic measurements. An immediately reconstructed 3D volume of the measured object could then give the operator direct feedback on the success of the experiment instead of relying only on the post-processing results after the beamtime. This requires further efforts to reduce the computation time for retrieving a projection image. The improved reconstruction algorithm should then be embedded in a fully automated pipeline, from hologram acquisition to refractive index projection image reconstruction to tomographic 3D volume reconstruction in the shortest possible time. It is also conceivable to reconstruct the volume directly from all holograms in a joint approach instead of acquiring the projection images separately and then calculating the tomogram. For this purpose, the target function has to be extended by a more sophisticated model, which should include the three-dimensional object and a motion model for the rotation and vibrations of the setup. In this setting, one could also exploit the overlapping information between the holograms of different angles and additionally retrieve the probe instead of performing a flat-field correction. Nevertheless, the results of the two core chapters of this thesis, the ASRM and the autofocus algorithm are already a step closer to the goal of a fully automated tomographic reconstruction pipeline. They offer simplified and automated processing of large amounts of holographic data sets in laboratories with synchrotron radiation sources.

Bibliography

[1] D. Gabor, "A New Microscopic Principle", *Nature*, vol. 161, no. 4098, pp. 777–778, May 1948. DOI: `10.1038/161777a0`.

[2] C. G. Schroer, H.-C. Wille, O. H. Seeck, K. Bagschik, H. Schulte-Schrepping, M. Tischer, H. Graafsma, W. Laasch, K. Baev, S. Klumpp, R. Bartolini, H. Reichert, W. Leemans, and E. Weckert, "The synchrotron radiation source PETRA III and its future ultra-low-emittance upgrade PETRA IV", *The European Physical Journal Plus*, vol. 137, no. 12, Dec. 2022, ISSN: 2190-5444. DOI: `10.1140/epjp/s13360-022-03517-6`.

[3] M. Altarelli, R. Brinkmann, and M. Chergui, "The European X-ray free-electron laser. Technical design report", Jul. 2007.

[4] P. Raimondi, "ESRF-EBS: The Extremely Brilliant Source Project", *Synchrotron Radiation News*, vol. 29, no. 6, pp. 8–15, 2016. DOI: `10.1080/08940886.2016.1244462`.

[5] P. F. Tavares, E. Al-Dmour, Å. Andersson, F. Cullinan, B. N. Jensen, D. Olsson, D. K. Olsson, M. Sjöström, H. Tarawneh, S. Thorin, and A. Vorozhtsov, "Commissioning and first-year operational results of the MAXIV 3GeV ring", *Journal of Synchrotron Radiation*, vol. 25, no. 5, pp. 1291–1316, Sep. 2018. DOI: `10.1107/S1600577518008111`.

[6] D. Einfeld, "ALBA synchrotron light source commissioning", *Proc. IPAC'11*, 2011.

[7] Snigirev, A. and Snigireva, I. and Kohn, V. and Kuznetsov, S. and Schelokov, I., "On the possibilities of x-ray phase contrast microimaging by coherent high-energy synchrotron radiation", *Review of Scientific Instruments*, vol. 66, no. 12, pp. 5486–5492, Dec. 1995, ISSN: 0034-6748. DOI: `10.1063/1.1146073`.

[8] M. Ogurreck, F. Wilde, J. Herzen, F. Beckmann, V. Nazmov, J. Mohr, A. Haibel, M. Müller, and A. Schreyer, "The nanotomography endstation at the PETRA III Imaging Beamline", *Journal of Physics: Conference Series*, vol. 425, no. 18, p. 182 002, Mar. 2013. DOI: `10.1088/1742-6596/425/18/182002`.

[9] J. R. Fienup, "Phase retrieval algorithms: a personal tour [Invited]", *Applied Optics*, vol. 52, no. 1, p. 45, Dec. 2012. DOI: `10.1364/ao.52.000045`.

[10] R. P. Millane, "Phase retrieval in crystallography and optics", *Journal of the Optical Society of America A*, vol. 7, no. 3, p. 394, Mar. 1990. DOI: `10.1364/josaa.7.000394`.

[11] D. R. Luke, J. V. Burke, and R. G. Lyon, “Optical Wavefront Reconstruction: Theory and Numerical Methods”, *SIAM Review*, vol. 44, no. 2, pp. 169–224, Jan. 2002. DOI: `10.1137/s003614450139075`.

[12] L. Taylor, “The phase retrieval problem”, *IEEE Transactions on Antennas and Propagation*, vol. 29, no. 2, pp. 386–391, Mar. 1981. DOI: `10.1109/tap.1981.1142559`.

[13] Y. Shechtman, Y. C. Eldar, O. Cohen, H. N. Chapman, J. Miao, and M. Segev, “Phase Retrieval with Application to Optical Imaging: A contemporary overview”, *IEEE Signal Processing Magazine*, vol. 32, no. 3, pp. 87–109, May 2015. DOI: `10.1109/msp.2014.2352673`.

[14] P. Cloetens, W. Ludwig, J. Baruchel, D. V. Dyck, J. V. Landuyt, J. P. Guigay, and M. Schlenker, “Holotomography: Quantitative phase tomography with micrometer resolution using hard synchrotron radiation x rays”, *Applied Physics Letters*, vol. 75, no. 19, pp. 2912–2914, Nov. 1999. DOI: `10.1063/1.125225`.

[15] R. W. Gerchberg, “A practical algorithm for the determination of plane from image and diffraction pictures”, *Optik*, vol. 35, no. 2, pp. 237–246, 1972.

[16] J. R. Fienup, “Reconstruction of an object from the modulus of its Fourier transform”, *Opt. Lett.*, vol. 3, no. 1, pp. 27–29, Jul. 1978. DOI: `10.1364/OL.3.000027`.

[17] J. R. Fienup, “Reconstruction of a complex-valued object from the modulus of its Fourier transform using a support constraint”, *J. Opt. Soc. Am. A*, vol. 4, no. 1, pp. 118–123, Jan. 1987. DOI: `10.1364/JOSAA.4.000118`.

[18] H. H. Bauschke, P. L. Combettes, and D. R. Luke, “Hybrid projection–reflection method for phase retrieval”, *J. Opt. Soc. Am. A*, vol. 20, no. 6, pp. 1025–1034, Jun. 2003. DOI: `10.1364/JOSAA.20.001025`.

[19] D. R. Luke, “Relaxed averaged alternating reflections for diffraction imaging”, *Inverse Problems*, vol. 21, no. 1, p. 37, Nov. 2004. DOI: `10.1088/0266-5611/21/1/004`.

[20] F. Wittwer, J. Hagemann, D. Brückner, S. Flenner, and C. G. Schroer, “Phase retrieval framework for direct reconstruction of the projected refractive index applied to ptychography and holography”, *Optica*, vol. 9, no. 3, pp. 295–302, Mar. 2022. DOI: `10.1364/OPTICA.447021`.

[21] J. Dora, M. Möddel, S. Flenner, C. Schroer, T. Knopp, and J. Hagemann, “Artifact-suppressing reconstruction of strongly interacting objects in X-ray near-field holography without a spatial support constraint”, *Optics Express*, Feb. 2024, ISSN: 1094-4087. DOI: `10.1364/oe.514641`.

[22] J. Reimers, H. Trinh, B. Wiese, S. Meyer, J. Brehling, S. Flenner, J. Hagemann, M. Kruth, L. Kibkalo, H. Cwieka, B. Hindenlang, M. Lipinska-Chwalek, J. Mayer, R. Willumeit-Roemer, I. Greving, and B. Zeller-Plumhoff, “Development of a Bioreactor-Coupled Flow-Cell Setup for 3D In Situ Nanotomography of Mg Alloy Biodegradation”, *ACS Applied Materials & Interfaces*, vol. 15, no. 29, Jul. 2023, ISSN: 1944-8252. DOI: `10.1021/acsami.3c04054`.

[23] S. Meyer, A. Wolf, D. Sanders, K. Iskhakova, H. Ćwieka, S. Bruns, S. Flenner, I. Greving, J. Hagemann, R. Willumeit-Römer, B. Wiese, and B. Zeller-Plumhoff, “Degradation Analysis of Thin Mg-xAg Wires Using X-ray Near-Field Holotomography”, *Metals*, vol. 11, no. 9, 2021, ISSN: 2075-4701. DOI: `10.3390/met11091422`.

[24] F. Sun, X. He, X. Jiang, M. Osenberg, J. Li, D. Zhou, K. Dong, A. Hilger, X. Zhu, R. Gao, X. Liu, K. Huang, D. Ning, H. Markötter, L. Zhang, F. Wilde, Y. Cao, M. Winter, and I. Manke, “Advancing knowledge of electrochemically generated lithium microstructure and performance decay of lithium ion battery by synchrotron X-ray tomography”, *Materials Today*, vol. 27, pp. 21–32, 2019, ISSN: 1369-7021. DOI: `10.1016/j.mattod.2018.11.003`.

[25] Z. Zhang, K. Dong, K. A. Mazzio, A. Hilger, H. Markötter, F. Wilde, T. Heinemann, I. Manke, and P. Adelhelm, “Phase Transformation and Microstructural Evolution of CuS Electrodes in Solid-State Batteries Probed by In Situ 3D X-Ray Tomography”, *Advanced Energy Materials*, vol. 13, no. 2, p. 2 203 143, Nov. 2022. DOI: `10.1002/aenm.202203143`.

[26] J. Dora, S. Flenner, and J. Hagemann, *A Python framework for the online reconstruction of X-ray near-field holography data*, version 1.0.0, Dec. 2023. DOI: `10.5281/zenodo.8349365`.

[27] P. Thibault, M. Dierolf, A. Menzel, O. Bunk, C. David, and F. Pfeiffer, “High-Resolution Scanning X-ray Diffraction Microscopy”, *Science*, vol. 321, no. 5887, pp. 379–382, Jul. 2008. DOI: `10.1126/science.1158573`.

[28] Y. Jiang, Z. Chen, Y. Han, P. Deb, H. Gao, S. Xie, P. Purohit, M. W. Tate, J. Park, S. M. Gruner, V. Elser, and D. A. Muller, “Electron ptychography of 2D materials to deep sub-ångström resolution”, *Nature*, vol. 559, no. 7714, pp. 343–349, Jul. 2018. DOI: `10.1038/s41586-018-0298-5`.

[29] M. Kahnt, L. Grote, D. Brückner, M. Seyrich, F. Wittwer, D. Koziej, and C. G. Schroer, “Multi-slice ptychography enables high-resolution measurements in extended chemical reactors”, *Scientific Reports*, vol. 11, no. 1, Jan. 2021. DOI: `10.1038/s41598-020-80926-6`.

[30] D. L. Misell, “An examination of an iterative method for the solution of the phase problem in optics and electron optics: I. Test calculations”, *Journal of Physics D: Applied Physics*, vol. 6, no. 18, pp. 2200–2216, Dec. 1973. DOI: `10.1088/0022-3727/6/18/305`.

[31] J. Hagemann, A.-L. Robisch, D. R. Luke, C. Homann, T. Hohage, P. Cloetens, H. Suhonen, and T. Salditt, "Reconstruction of wave front and object for in-line holography from a set of detection planes", *Opt. Express*, vol. 22, no. 10, pp. 11 552–11 569, May 2014. DOI: `10.1364/OE.22.011552`.

[32] J. R. Fienup, T. R. Crimmins, and W. Holsztynski, "Reconstruction of the support of an object from the support of its autocorrelation", *J. Opt. Soc. Am.*, vol. 72, no. 5, pp. 610–624, May 1982.

[33] J. R. Fienup, "Phase retrieval algorithms: a comparison", *Appl. Opt.*, vol. 21, no. 15, pp. 2758–2769, Aug. 1982. DOI: `10.1364/AO.21.002758`.

[34] S. Marchesini, H. He, H. N. Chapman, S. P. Hau-Riege, A. Noy, M. R. Howells, U. Weierstall, and J. C. H. Spence, "X-ray image reconstruction from a diffraction pattern alone", *Physical Review B*, vol. 68, no. 14, Oct. 2003, ISSN: 1095-3795. DOI: `10.1103/physrevb.68.140101`.

[35] D. Paganin, S. C. Mayo, T. E. Gureyev, P. R. Miller, and S. W. Wilkins, "Simultaneous phase and amplitude extraction from a single defocused image of a homogeneous object", *Journal of microscopy*, vol. 206, no. 1, pp. 33–40, 2002. DOI: `10.1046/j.1365-2818.2002.01010.x`.

[36] P. Cloetens, R. Barrett, J. Baruchel, J.-P. Guigay, and M. Schlenker, "Phase objects in synchrotron radiation hard x-ray imaging", *Journal of physics D: applied physics*, vol. 29, no. 1, p. 133, 1996. DOI: `10.1088/0022-3727/29/1/023`.

[37] T. Latychevskaia and H.-W. Fink, "Solution to the twin image problem in holography", *Physical review letters*, vol. 98, no. 23, p. 233 901, 2007. DOI: `10.1103/PhysRevLett.98.233901`.

[38] J. Hagemann, M. Töpperwien, and T. Salditt, "Phase retrieval for near-field X-ray imaging beyond linearisation or compact support", *Applied Physics Letters*, vol. 113, no. 4, 2018. DOI: `10.1063/1.5029927`.

[39] J. Dora, M. Möddel, S. Flenner, J. Reimers, B. Zeller-Plumhoff, C. G. Schroer, T. Knopp, and J. Hagemann, "Model-based autofocus for near-field phase retrieval", *Opt. Express*, vol. 33, no. 4, pp. 6641–6657, Feb. 2025. DOI: `10.1364/OE.544573`.

[40] J. Dora, S. Flenner, A. Lopes Marinho, and J. Hagemann, *A Python framework for the online reconstruction of X-ray near-field holography data*, version 1.3.0, Oct. 2024. DOI: `10.5281/zenodo.13928062`.

[41] J. Als-Nielsen and D. McMorrow, *Elements of Modern X-ray Physics.* Wiley, Mar. 2011, ISBN: 9781119998365. DOI: `10.1002/9781119998365`.

[42] D. Paganin, *Coherent X-Ray Optics.* Oxford University Press, Jan. 2006, ISBN: 9780198567288. DOI: `10.1093/acprof:oso/9780198567288.001.0001`.

[43] T. Schoonjans, A. Brunetti, B. Golosio, M. Sanchez del Rio, V. A. Solé, C. Ferrero, and L. Vincze, "The xraylib library for X-ray–matter interactions. Recent developments", *Spectrochimica Acta Part B: Atomic Spectroscopy*, vol. 66, no. 11, pp. 776–784, 2011, ISSN: 0584-8547. DOI: `10.1016/j.sab.2011.09.011`.

[44] A. Brunetti, M. Sanchez del Rio, B. Golosio, A. Simionovici, and A. Somogyi, "A library for X-ray–matter interaction cross sections for X-ray fluorescence applications", *Spectrochimica Acta Part B: Atomic Spectroscopy*, vol. 59, no. 10, pp. 1725–1731, 2004, 17th International Congress on X-Ray Optics and Microanalysis, ISSN: 0584-8547. DOI: `10.1016/j.sab.2004.03.014`.

[45] P. Cloetens, R. Barrett, J. Baruchel, J.-P. Guigay, and M. Schlenker, "Phase objects in synchrotron radiation hard X-ray imaging", *Journal of physics D: applied physics*, vol. 29, p. 133, Jan. 1996. DOI: `10.1088/0022-3727/29/1/023`.

[46] S. Flenner, A. Kubec, C. David, M. Storm, C. F. Schaber, F. Vollrath, M. Müller, I. Greving, and J. Hagemann, "Hard X-ray nano-holotomography with a Fresnel zone plate", *Opt. Express*, vol. 28, no. 25, pp. 37 514–37 525, Dec. 2020. DOI: `10.1364/OE.406074`.

[47] A. des sciences (France), *Mémoires de l'Académie des sciences de l'Institut de France*. Oxford University, 1826.

[48] J. Kirz, "Phase zone plates for x rays and the extreme uv", *Journal of the Optical Society of America*, vol. 64, no. 3, p. 301, Mar. 1974, ISSN: 0030-3941. DOI: `10.1364/josa.64.000301`.

[49] G. Schmahl, D. Rudolph, P. Guttmann, and O. Christ, "Zone Plates for X-Ray Microscopy", in *Springer Series in Optical Sciences*. Springer Berlin Heidelberg, 1984, pp. 63–74, ISBN: 9783540388333. DOI: `10.1007/978-3-540-38833-3_9`.

[50] L. Kipp, M. Skibowski, R. L. Johnson, R. Berndt, R. Adelung, S. Harm, and R. Seemann, "Sharper images by focusing soft X-rays with photon sieves", *Nature*, vol. 414, no. 6860, pp. 184–188, Nov. 2001, ISSN: 1476-4687. DOI: `10.1038/35102526`.

[51] C. Homann, T. Hohage, J. Hagemann, A.-L. Robisch, and T. Salditt, "Validity of the empty-beam correction in near-field imaging", *Phys. Rev. A*, vol. 91, p. 013 821, 1 Jan. 2015. DOI: `10.1103/PhysRevA.91.013821`.

[52] V. V. Nieuwenhove, J. D. Beenhouwer, F. D. Carlo, L. Mancini, F. Marone, and J. Sijbers, "Dynamic intensity normalization using eigen flat fields in X-ray imaging", *Opt. Express*, vol. 23, no. 21, pp. 27 975–27 989, Oct. 2015. DOI: `10.1364/oe.23.027975`.

[53] J. Hagemann, M. Vassholz, H. Hoeppe, M. Osterhoff, J. M. Rosselló, R. Mettin, F. Seiboth, A. Schropp, J. Möller, J. Hallmann, C. Kim, M. Scholz, U. Boesenberg, R. Schaffer, A. Zozulya, W. Lu, R. Shayduk, A. Madsen, C. G. Schroer, and T. Salditt, "Single-pulse phase-contrast imaging at free-electron lasers in the hard X-ray regime", *Journal of Synchrotron Radiation*, vol. 28, no. 1, pp. 52–63, Jan. 2021. DOI: `10.1107/s160057752001557x`.

[54] P. Thibault and M. Guizar-Sicairos, "Maximum-likelihood refinement for coherent diffractive imaging", *New Journal of Physics*, vol. 14, no. 6, p. 063 004, Jun. 2012. DOI: `10.1088/1367-2630/14/6/063004`.

[55] P. Godard, M. Allain, V. Chamard, and J. Rodenburg, "Noise models for low counting rate coherent diffraction imaging", *Opt. Express*, vol. 20, no. 23, pp. 25 914–25 934, Nov. 2012. DOI: `10.1364/OE.20.025914`.

[56] A. Levi and H. Stark, "Image restoration by the method of generalized projections with application to restoration from magnitude", *J. Opt. Soc. Am. A*, vol. 1, no. 9, pp. 932–943, Sep. 1984. DOI: `10.1364/JOSAA.1.000932`.

[57] J. R. Fienup and C. C. Wackerman, "Phase-retrieval stagnation problems and solutions", *J. Opt. Soc. Am. A*, vol. 3, no. 11, pp. 1897–1907, Nov. 1986. DOI: `10.1364/JOSAA.3.001897`.

[58] E. J. Candès, X. Li, and M. Soltanolkotabi, "Phase Retrieval via Wirtinger Flow: Theory and Algorithms", *IEEE Transactions on Information Theory*, vol. 61, no. 4, pp. 1985–2007, 2015. DOI: `10.1109/TIT.2015.2399924`.

[59] R. Xu, M. Soltanolkotabi, J. P. Haldar, W. Unglaub, J. Zusman, A. F. J. Levi, and R. M. Leahy, *Accelerated Wirtinger Flow: A fast algorithm for ptychography*, 2018. DOI: `10.48550/arXiv.1806.05546`. arXiv: `1806.05546 [eess.IV]`.

[60] S. Ruder, *An overview of gradient descent optimization algorithms*, 2016. DOI: `10.48550/ARXIV.1609.04747`.

[61] R. S. Sutton, "Two problems with backpropagation and other steepest-descent learning procedures for networks", in *Proc. of Eightth Annual Conference of the Cognitive Science Society*, 1986, pp. 823–831.

[62] Y. E. Nesterov, "A method of solving a convex programming problem with convergence rate $O(1/k^2)$", in *Doklady Akademii Nauk*, Russian Academy of Sciences, vol. 269, 1983, pp. 543–547.

[63] N. Qian, "On the momentum term in gradient descent learning algorithms", *Neural Networks*, vol. 12, no. 1, pp. 145–151, 1999, ISSN: 0893-6080. DOI: `10.1016/S0893-6080(98)00116-6`.

[64] A. Haibel, M. Ogurreck, F. Beckmann, T. Dose, F. Wilde, J. Herzen, M. Müller, A. Schreyer, V. Nazmov, M. Simon, A. Last, and J. Mohr, "Micro- and nanotomography at the GKSS Imaging Beamline at PETRA III", in *Developments in X-Ray Tomography VII*, S. R. Stock, Ed., SPIE, Aug. 2010. DOI: `10.1117/12.860852`.

[65] A. Haibel, F. Beckmann, T. Dose, J. Herzen, M. Ogurreck, M. Müller, and A. Schreyer, "Latest developments in microtomography and nanotomography at PETRA III", *Powder Diffraction*, vol. 25, no. 2, pp. 161–164, 2010. DOI: `10.1154/1.3428364`.

[66] D. T. Roscoe and G. Walker, "The adhesion of spiders to smooth surfaces", *Bull. Br. arachnol. Soc.*, 1991.

[67] C. F. Schaber, S. Flenner, A. Glisovic, I. Krasnov, M. Rosenthal, H. Stieglitz, C. Krywka, M. Burghammer, M. Müller, and S. N. Gorb, "Hierarchical architecture of spider attachment setae reconstructed from scanning nanofocus X-ray diffraction data", *Journal of The Royal Society Interface*, vol. 16, no. 150, p. 20 180 692, 2019. DOI: `10.1098/rsif.2018.0692`.

[68] S. Niederegger and S. N. Gorb, "Friction and adhesion in the tarsal and metatarsal scopulae of spiders", *Journal of Comparative Physiology A*, vol. 192, pp. 1223–1232, 2006, ISSN: 1432-1351. DOI: `10.1007/s00359-006-0157-y`.

[69] B. Zeller-Plumhoff, M. Gile, M. Priebe, H. Slominska, B. Boll, B. Wiese, T. Würger, R. Willumeit-Römer, and R. H. Meißner, "Exploring key ionic interactions for magnesium degradation in simulated body fluid – A data-driven approach", *Corrosion Science*, vol. 182, p. 109 272, 2021, ISSN: 0010-938X. DOI: `10.1016/j.corsci.2021.109272`.

[70] B. Zeller-Plumhoff, H. Helmholz, F. Feyerabend, T. Dose, F. Wilde, A. Hipp, F. Beckmann, R. Willumeit-Römer, and J. U. Hammel, "Quantitative characterization of degradation processes in situ by means of a bioreactor coupled flow chamber under physiological conditions using time-lapse SRμCT", *Materials and Corrosion*, vol. 69, no. 3, pp. 298–306, 2018. DOI: `10.1002/maco.201709514`.

[71] D. G. Voelz and M. C. Roggemann, "Digital simulation of scalar optical diffraction: revisiting chirp function sampling criteria and consequences", *Applied Optics*, vol. 48, no. 32, p. 6132, Nov. 2009. DOI: `10.1364/ao.48.006132`.

[72] S. Huhn, L. M. Lohse, J. Lucht, and T. Salditt, "Fast algorithms for nonlinear and constrained phase retrieval in near-field X-ray holography based on Tikhonov regularization", *Opt. Express*, vol. 30, no. 18, pp. 32 871–32 886, Aug. 2022. DOI: `10.1364/OE.462368`.

[73] V. Davidoiu, B. Sixou, M. Langer, and F. Peyrin, "Non-linear iterative phase retrieval based on Frechet derivative", *Opt. Express*, vol. 19, no. 23, pp. 22 809–22 819, Nov. 2011. DOI: `10.1364/OE.19.022809`.

[74] B. Henke, E. Gullikson, and J. Davis, “X-Ray Interactions: Photoabsorption, Scattering, Transmission, and Reflection at E = 50-30,000 eV, Z = 1-92”, *Atomic Data and Nuclear Data Tables*, vol. 54, no. 2, pp. 181–342, Jul. 1993. DOI: `10.1006/adnd.1993.1013`.

[75] B. Sixou, V. Davidoiu, M. Langer, and F. Peyrin, *Absorption and phase retrieval with Tikhonov and joint sparsity regularizations*, 2013. DOI: `10.3934/ipi.2013.7.267`.

[76] S. Loock and G. Plonka, “Phase retrieval for Fresnel measurements using a shearlet sparsity constraint”, *Inverse Problems*, vol. 30, no. 5, p. 055 005, Apr. 2014, ISSN: 1361-6420. DOI: `10.1088/0266-5611/30/5/055005`.

[77] V. Davidoiu, B. Sixou, M. Langer, and F. Peyrin, “Nonlinear approaches for the single-distance phase retrieval problem involving regularizations with sparsity constraints”, *Appl. Opt.*, vol. 52, no. 17, pp. 3977–3986, Jun. 2013. DOI: `10.1364/AO.52.003977`.

[78] K. Mom, M. Langer, and B. Sixou, “Nonlinear primal–dual algorithm for the phase and absorption retrieval from a single phase contrast image”, *Opt. Lett.*, vol. 47, no. 20, pp. 5389–5392, Oct. 2022. DOI: `10.1364/OL.469174`.

[79] L. I. Rudin, S. Osher, and E. Fatemi, “Nonlinear total variation based noise removal algorithms”, *Physica D: Nonlinear Phenomena*, vol. 60, no. 1, pp. 259–268, 1992, ISSN: 0167-2789. DOI: `10.1016/0167-2789(92)90242-F`.

[80] A. Chambolle and P.-L. Lions, “Image recovery via total variation minimization and related problems”, *Numerische Mathematik*, vol. 76, no. 2, pp. 167–188, Apr. 1997, ISSN: 0945-3245. DOI: `10.1007/s002110050258`.

[81] D. C. Dobson and F. Santosa, “Recovery of Blocky Images from Noisy and Blurred Data”, *SIAM Journal on Applied Mathematics*, vol. 56, no. 4, pp. 1181–1198, Aug. 1996, ISSN: 1095-712X. DOI: `10.1137/s003613999427560x`.

[82] A. N. Tikhonov and V. Y. Arsenin, *Solutions of ill-posed problems.* Washington, D.C.: John Wiley & Sons, New York: V. H. Winston & Sons, 1977, pp. xiii+258, Translated from the Russian, Preface by translation editor Fritz John, Scripta Series in Mathematics.

[83] A. N. Tikhonov, A. V. Goncharsky, V. V. Stepanov, and A. G. Yagola, *Numerical methods for the solution of ill-posed problems.* Springer Netherlands, 1995, pp. 65–79, ISBN: 9789401584807. DOI: `10.1007/978-94-015-8480-7_3`.

[84] K. T. Block, M. Uecker, and J. Frahm, “Suppression of MRI Truncation Artifacts Using Total Variation Constrained Data Extrapolation”, *International Journal of Biomedical Imaging*, vol. 2008, pp. 1–8, 2008, ISSN: 1687-4196. DOI: `10.1155/2008/184123`.

[85] J. W. Gibbs, “Fourier’s Series”, *Nature*, vol. 59, no. 1539, pp. 606–606, Apr. 1899, ISSN: 1476-4687. DOI: `10.1038/059606a0`.

[86] L. Czervionke, J. Czervionke, D. Daniels, and V. Haughton, “Characteristic features of MR truncation artifacts”, *American Journal of Roentgenology*, vol. 151, no. 6, pp. 1219–1228, Dec. 1988, ISSN: 1546-3141. DOI: `10.2214/ajr.151.6.1219`.

[87] T. Butz, *Fourier Transformation for Pedestrians* (Undergraduate Lecture Notes in Physics), en, 2nd ed. Cham, Switzerland: Springer International Publishing, May 2015, ISBN: 9783540231653. DOI: `10.1007/978-3-540-31108-9`.

[88] A. V. Oppenheim, R. W. Schafer, M. A. Yoder, and W. T. Padgett, *Discrete-time signal processing*, en, 3rd ed. Upper Saddle River, NJ: Pearson, Aug. 2009, ISBN: 9780132067096.

[89] R. Tibshirani, “Regression Shrinkage and Selection Via the Lasso”, *Journal of the Royal Statistical Society: Series B (Methodological)*, vol. 58, no. 1, pp. 267–288, 1996. DOI: `10.1111/j.2517-6161.1996.tb02080.x`.

[90] I. Daubechies, M. Defrise, and C. De Mol, *An iterative thresholding algorithm for linear inverse problems with a sparsity constraint*, 2003. DOI: `10.48550/ARXIV.MATH/0307152`.

[91] *Python Language Reference, version 3.8*, Python Software Foundation., 2019.

[92] A. Paszke, S. Gross, S. Chintala, G. Chanan, E. Yang, Z. DeVito, Z. Lin, A. Desmaison, L. Antiga, and A. Lerer, “Automatic differentiation in PyTorch”, in *NIPS-W*, 2017.

[93] *PyTorch Reference, version 1.10.2*, Torch Contributors, 2019.

[94] NVIDIA, *NVIDIA A100 Tensor Core GPU Architecture*, 2020.

[95] F. Witte, “The history of biodegradable magnesium implants: A review”, *Acta Biomaterialia*, vol. 6, no. 5, pp. 1680–1692, 2010, The THERMEC’2009 Biodegradable Metals, ISSN: 1742-7061. DOI: `10.1016/j.actbio.2010.02.028`.

[96] M. Liebling and M. Unser, “Autofocus for digital Fresnel holograms by use of a Fresnelet-sparsity criterion”, *J. Opt. Soc. Am. A*, vol. 21, no. 12, pp. 2424–2430, Dec. 2004. DOI: `10.1364/JOSAA.21.002424`.

[97] Y. Wu, Y. Rivenson, Y. Zhang, Z. Wei, H. Günaydin, X. Lin, and A. Ozcan, “Extended depth-of-field in holographic imaging using deep-learning-based autofocusing and phase recovery”, *Optica*, vol. 5, no. 6, pp. 704–710, Jun. 2018. DOI: `10.1364/OPTICA.5.000704`.

[98] P. Memmolo, C. Distante, M. Paturzo, A. Finizio, P. Ferraro, and B. Javidi, “Automatic focusing in digital holography and its application to stretched holograms”, *Opt. Lett.*, vol. 36, no. 10, pp. 1945–1947, May 2011. DOI: `10.1364/OL.36.001945`.

[99] P. Langehanenberg, B. Kemper, D. Dirksen, and G. von Bally, “Autofocusing in digital holographic phase contrast microscopy on pure phase objects for live cell imaging”, *Appl. Opt.*, vol. 47, no. 19, pp. D176–D182, Jul. 2008. DOI: `10.1364/AO.47.00D176`.

[100] Y. Zhang, H. Wang, Y. Wu, M. Tamamitsu, and A. Ozcan, “Edge sparsity criterion for robust holographic autofocusing”, *Opt. Lett.*, vol. 42, no. 19, pp. 3824–3827, Oct. 2017. DOI: `10.1364/OL.42.003824`.

[101] J. A. Nelder and R. Mead, “A Simplex Method for Function Minimization”, *The Computer Journal*, vol. 7, no. 4, pp. 308–313, Jan. 1965, ISSN: 0010-4620. DOI: `10.1093/comjnl/7.4.308`.

[102] J. C. Lagarias, J. A. Reeds, M. H. Wright, and P. E. Wright, “Convergence Properties of the Nelder–Mead Simplex Method in Low Dimensions”, *SIAM Journal on Optimization*, vol. 9, no. 1, pp. 112–147, 1998. DOI: `10.1137/S1052623496303470`.

[103] N. Hurley and S. Rickard, “Comparing measures of sparsity”, *IEEE Transactions on Information Theory*, vol. 55, no. 10, pp. 4723–4741, 2009. DOI: `10.1109/TIT.2009.2027527`.

[104] C. G. Schroer, I. Agapov, W. Brefeld, R. Brinkmann, Y.-C. Chae, H.-C. Chao, M. Eriksson, J. Keil, X. Nuel Gavaldà, R. Röhlsberger, O. H. Seeck, M. Sprung, M. Tischer, R. Wanzenberg, and E. Weckert, “PETRA IV: the ultralow-emittance source project at DESY”, *Journal of Synchrotron Radiation*, vol. 25, no. 5, pp. 1277–1290, Sep. 2018. DOI: `10.1107/S1600577518008858`.

[105] L. Liu, R. T. Neuenschwander, and A. R. D. Rodrigues, “Synchrotron radiation sources in Brazil”, *Philosophical Transactions of the Royal Society A: Mathematical, Physical and Engineering Sciences*, vol. 377, no. 2147, p. 20 180 235, Apr. 2019, ISSN: 1471-2962. DOI: `10.1098/rsta.2018.0235`.

[106] F. Pérez, I. Bellafont, G. Benedetti, J. Campmany, M. Carlà, J. Casas, C. Collderam, F. Fernández, J. C. Giraldo, T. Günzel, U. Iriso, J. Marcos, Z. Martí, V. Massana, R. Muñoz Horta, M. Pont, L. Ribó, P. Solans, and L. Torino, “ALBA II Accelerator Upgrade Project”, en, 2022. DOI: `10.18429/JACOW-IPAC2022-TUPOMS027`.